STRUCTURAL AND MECHANICAL INVESTIGATIONS OF MAGNESIUM AND FLUORIDE DOPED NANO CALCIUM PHOSPHATES

A THESIS SUBMITTED TO
THE GRADUATE SCHOOL OF NATURAL AND APPLIED SCIENCES,
MICRO AND NANOTECHNOLOGY DEPARTMENT
OF
MIDDLE EAST TECHNICAL UNIVERSITY

BY

ZEHRA PINAR SUN

IN PARTIAL FULLFILLMENT OF THE REQUIREMENTS
FOR
THE DEGREE OF MASTER OF SCIENCE
IN
MICRO AND NANOTECHNOLOGY

JULY 2009

Approval of the thesis:

STRUCTURAL AND MECHANICAL INVESTIGATIONS OF MAGNESIUM AND FLUORIDE DOPED NANO CALCIUM PHOSPHATES

submitted by **ZEHRA PINAR SUN** in partial fulfillment of the requirements for the degree of **Master of Science in Micro and Nanotechnology Department, Middle East Technical University** by,

Prof. Dr. Canan Özgen _____
Dean, Graduate School of **Natural and Applied Sciences.**

Prof. Dr. Raşit Turan _____
Head of Department, **Micro and Nanotechnology**

Assoc. Prof. Dr. Zafer Evis
Supervisor, **Engineering Sciences Dept., METU** _____

Assoc. Prof. Dr. Caner Durucan
Co-supervisor**, Metallurgical and Materials Engineering Dept., METU** _____

Examining Committee Members

Assist. Prof. Dr. Arcan Dericioglu _____
Metallurgical and Materials Engineering Dept., METU

Assoc. Prof. Dr. Zafer Evis _____
Engineering Sciences Dept., METU

Assoc. Prof. Dr. Caner Durucan _____
Metallurgical and Materials Engineering Dept., METU

Assist. Prof. Dr. Dr. Ayşen Tezcaner _____
Engineering Sciences Dept., METU

Assist. Prof. Dr. Dilek Keskin _____
Engineering Sciences Dept., METU

Date: 07.07.2009

I hereby declare that all information in this document has been obtained and presented in accordance with academic rules and ethical conduct. I also declare that, as required by these rules and conduct, I have fully cited and referenced all material and results that are not original to this document.

Name, Last name: Zehra Pınar Sun

Signature:

ABSTRACT

STRUCTURAL AND MECHANICAL INVESTIGATIONS OF MAGNESIUM AND FLUORIDE DOPED NANO CALCIUM PHOSPHATES

Sun, Zehra Pınar

M. Sc., Micro and Nanotechnology

Supervisor: Assoc. Prof. Dr. Zafer Evis

Co-Supervisor: Assoc. Prof. Dr. Caner Durucan

July 2009, pages 105

The aim of this study was to investigate the microstructure and mechanical properties of pure and Mg^{2+} and F^- doped nano-calcium phosphate (CaP) powders, which were synthesized by precipitation method. After the drying and calcination processes, the samples were sintered at 1100ºC for 1 hour. High densities were achieved except for the 7.5 % mole Mg doped samples. Microstructure of the CaPs were investigated by X- ray diffraction (XRD), Fourier Transform Infrared Spectroscopy (FTIR) and Scanning Electron Microscopy (SEM). Due to the Mg substitution, β-TCP phase was detected besides HAp, resulting in the formation of HAp/ β-TCP biphasic composites with different compositions. The substitutions of the ions have been verified by the decrease in the hexagonal unit cell volumes of the doped CaPs. FTIR spectra revealed the characteristic absorption bands of HAp, β-TCP and the ones that were resulted from the F-OH bonds and substitution of the Mg^{2+} ions. The SEM results revealed the grain sizes in the range of ~197 nm-740 nm. In general, the micro hardness and diametral tensile strength tests revealed that Mg^{2+} ions in large amounts (7.5 % mole) had negative effects on the mechanical properties of the samples, while substitution of the F^- ions had a positive effect on their mechanical properties.

Keywords: Bioceramics, Nano calcium phosphates, Magnesium, Fluoride, Sintering.

ÖZ

MAGNEZYUM VE FLOR EKLENMİŞ NANO-KALSİYUM FOSFATLARIN İÇ YAPI VE MEKANİK ÖZELLİKLER YÖNÜNDEN İNCELENMESİ

Sun, Zehra Pınar
Yüksek Lisans, Mikro ve Nanoteknoloji
Tez Yöneticisi: Doç. Dr. Zafer Evis
Yardımcı Tez Yöneticisi: Doç. Dr. Caner Durucan

Temmuz 2009, sayfa 105

Bu çalışmanın amacı çöktürme metoduyla üretilmiş olan saf ve Mg^{2+} ve F^- iyonları eklenmiş nano-kalsiyum fosfat (CaP) tozlarının mikro yapı ve mekanik özellikleri yönünden incelenmesidir. Kurutma ve kalsinasyon işlemlerinden sonra, ürünler 1100ºC'de 1 saat sinterlenmiştir. % 7.5 mol Mg eklenmiş örnekler hariç yüksek yoğunlukta kalsiyum fosfatlar üretilmiştir. Kalsiyum fosfatların mikroyapıları X-ışınları kırınımı, Fourier transform infrared spektrometresi ve Taramalı elektron mikroskobu ile incelenmiştir. Mg eklenmesi nedeniyle HAp'e ilaveten β-TCP fazı da oluşarak değişik kompozisyonlarda HAp/ β-TCP bifazik kompozitleri üretilmiştir. İyon eklenmiş kalsiyum fosfatların hegzagonal kafes hacimlerinde gözlenen azalma bu iyonların içyapıya girebildiklerini göstermiştir. FTIR sonuçları, HAp, β-TCP ve F-OH bağlarına atfedilmiş olan karakteristik bandları göstermiştir. SEM sonuçlarına göre 197 nm-740 nm değerleri arasında değişen tane boyutları belirlenmiştir. Mikrosertlik ve diyametral çekme dayanımı testleri sonucunda genel anlamda yüksek oranlardaki Mg^{2+} iyonlarının mekanik özellikleri negatif yönde etkilediği, F^- iyonlarının ise mekanik özellikleri iyileştirdiği saptanmıştır.

Anahtar Sözcükler: Biyoseramikler, Nano kalsiyum fosfatlar, Magnezyum, Flor, Sinterleme.

ACKNOWLEDGEMENTS

I would like to express my special thanks to my advisor Assoc. Prof. Dr. Zafer Evis for his enthusiastic guidance and patience throughout this study. I am also so grateful to my advisor for encouraging me in this fascinating field and for letting me benefit from his profound mind and knowledge.

Additionally, I would like to thank to my co-advisor Assoc. Prof. Dr. Caner Durucan for the precious lectures he gave in his Bioceramics class and for his precious helps in this thesis.

I would also like to thank to Assist. Prof. Dr. Ayşen Tezcaner, Assist. Prof. Dr. Dilek Keskin and my advisor for letting me work in their lovely biomaterials laboratory. I must thank to my lab friend Burçin Başar for her precious helps in this study. Moreover, I owe many thanks to my other lab friends Ayşegül Kavas, Özge Erdemli, Ömer Aktürk, Özlem Aydın, Mine Toker and Seylan Aygün for their fellowships.

I would like to give my special thanks to my dear friend Dr. Nurperi Ruhan Ayengin for being beside me in my hard times, her precious support and encouragement in every stage of my thesis.

My greatest thanks should be for my beloved parents Mehmet Sabit Sun and Saide Özkân Sun for their endless supports and encouragements at every stage of my life and this thesis. I would also like to thank to my one and only little niece Defne Sun for the joy and happiness she brought to our family, to my brothers Mustafa Sun and Melih Sun and his wife Demet Sun for encouraging me during my studies .

TABLE OF CONTENTS

LIST OF TABLES

LIST OF FIGURES

CHAPTER 1

INTRODUCTION

1.1 Nanostructured Materials

Nano materials are a broad class of materials with length scales less than 100 nm in at least one dimension and include nanoparticles, nanorods and nanowires, thin films and bulk materials made of nanoscale building blocks or consisting of nanoscale structures [1]. In the micro scale, materials mostly exhibit the same physical properties in the bulk form. However, in the nano scale, their properties are significantly different than those of bulk forms [1].

There is a broad field of nano structured materials including nanoparticles, nanocrystalline materials and nanodevices, which have possible applications such as dispersions and coatings, high surface area materials, functional nanostructures (e.g., optoelectronic devices, biosensors, nanomachines) and bulk nanostructured materials, which are used in structural and magnetic applications. Depending on their dimensions, nanostructured materials can be classified into [2];

(a) Nanoparticles; which are essentially atom clusters and can be considered as zero-dimensional (0-D) in nature [3].

(b) Layered or lamellar structures; are one-dimensional (1-D) nanostructures in which the thickness is only a few nanometers in size but the magnitudes of length and width are much greater.

(c) Filamentary structures; are two-dimensional (2-D) nanostructures in which the length is substantially larger than width or diameter which are of nanometer dimensions.

(d) Bulk nanostructured materials; are termed as nanostructure crystallites which are three-dimensional (3-D) nanostructures. They are basically equiaxed and all the three dimensions are of nanometer scale.

Some of the typical synthesis methods for these nanomaterials are; sol-gel method for zero 0-D, vapor deposition and electro deposition for 1-D, chemical vapor deposition for 2-D and gas condensation and mechanical alloying for 3-D nanocrystalline materials [2].

The nanostructured materials can be metals, ceramics, polymers or composites and may contain crystalline, quasicrystalline or amorphous phases. The materials with the grains made up of crystals are called nanocrystallines and the ones, which are made up of quasicrystalline or amorphous phases are called nanoquasicrystals and nanoglasses, respectively [2].

Due to their large surface to volume ratio and unusual chemical and electronic properties, nanostructured materials can offer much more improved performances than their coarser grained counterparts [4].

Nano structured materials have unique properties as a result of the significant increase in the grain boundary area due to the small grain size. As the grain size decreases to nanometer scale, the volume fraction increases significantly which strongly influences the chemical, physical and mechanical properties of the materials resulting in a remarkable improvement or deviation in comparison with the coarser grained polycrystalline materials [5]. For example, nanostructured ceramics are tougher and stronger than the coarser grained ceramics and may exhibit super plastic properties at low temperatures which is significant considering the brittle nature of the conventional ceramics [4]. In Figure 1.1, a schematic presentation of a nanocrystalline material is shown, in which the grain boundary atoms are white and the atoms in the center of the crystals are shown as black spheres [5].

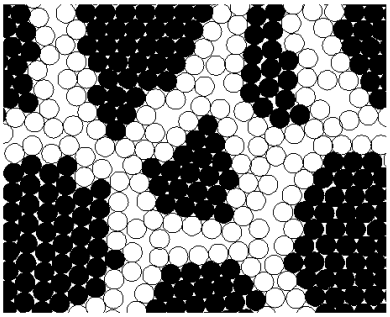

Figure 1.1 Two-dimensional model of a nanostructured material [5].

Nanocrystalline materials may exhibit increased strength and hardness, improved toughness, enhanced diffusivity and thermal expansion coefficient (CTE), superior soft magnetic properties and reduced elastic modulus and thermal conductivity in comparision with conventional polycrystalline materials [2,5].

By using various synthesis methods, it is possible to produce nanostructured materials in the forms of thin films, coatings, powders and as a bulk material. Nanomaterials can be produced by top-down and bottom-up approaches [5]. In the top-down method, the polycrystalline bulk material is broken down into crystalline units with the dimensions of nanometers whereas in the bottom-up approach, the nanostructure is arranged by consolidating the small clusters atom by atom and layer by layer [5]. Table 1.1 summarizes the synthesis methods of nanocrystalline materials according to their starting phase and the nature of the product [2].

Table 1.1 Methods to synthesize nanocrystalline materials [2].

Starting Phase	Technique	Nature of Product
Vapor	Inert gas condensation	3-D
	Physical vapor deposition- Evaporation and Sputtering	1-D
	Plasma processing	3-D
	Chemical vapor condensation	2-D, 3-D
	Chemical reactions	3-D
Liquid	Rapid solidification	3-D
	Electrodeposition	1-D, 3-D
	Chemical Reactions	3-D
Solid	Mechanical attrition	3-D
	Devitrification	3-D
	Spark erosion	3-D
	Sliding wear	3-D

1.2 Nanoceramics

Ceramics with grain sizes in nanometer range received much attention during the last decade owing to their superior properties such as extreme hardness, high fracture toughness and super-plastic behaviors in low temperatures (at temperatures smaller than $0.5T_m$) [2]. These unique properties are a consequence of the small grain size and large amount of grain boundaries, which result in unusual (thermo-) mechanical properties. It has been reported that the low-temperature plasticity behaviors of the nanoceramics are due to the mutual sliding of nanometer grains and atomic transport along their boundaries [6,7]. It is reported that large plastic strains up to 100% can be observed in nano grain size brittle ceramics [4,8].

Although enhancements in the mechanical behaviors are often associated with small grain sizes, it has been shown that in nano scale regime (<20nm) [2],

nanostructured ceramics might exhibit an inverse Hall-Petch effect; in which, the hardness decreases by decreasing the grain size, which is attributed to a crossover from dislocation mediated plasticity for large grain size to grain boundary sliding for small grain sizes [9].

During the densification process, grain growth is the common problem for all nanophase powders. In most of the nanophase material systems, accelerated grain growth is observed when the density of the specimen exceeds about 90% of the theoretical density. Introducing grain growth inhibitors is a method to overcome this problem [7]. For example, in the case of hydroxyapatite (HAp) nanopowders, introducing various ions such as Mg^{2+} led to smaller grain sizes by the adsorption of Mg ions on the surface of the HAp [10]. Grain growth also occurs because of the agglomerates in these powders and as a result, inter-agglomerate pores will form during pressing and pores exceeding a critical size might lead to grain growth during sintering [7]. Figure 1.2 shows an illustration of an agglomerated powder structure.

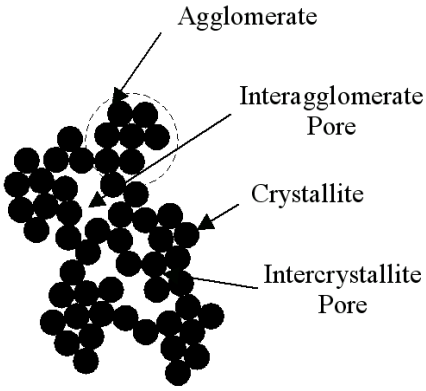

Figure 1.2 Schematic diagram of an agglomerated powder [7].

Besides using grain growth inhibitors, hot isostatic pressing (HIP) is also a method, which avoids grain growth during sintering. Another approach to reduce the grain growth is the surface modification. A possible method reported for the nanophase SiC is the use of a treatment of the powders at elevated temperatures in a nitrogen atmosphere [7]. As a result of this heat treatment, Si_3Ni_4 layer is formed on

the SiC particles and stabilized the SiC grains against the grain growth [7]. For the fabrication of nanostructured ceramics, methods such as hot pressing, HIP, spark plasma sintering etc. can be employed [5]. Conventional pressureless sintering is the most common and low-cost approach among them but in this method it is difficult to reduce grain growth during densification. Table 1.2 shows a list of various nano bioceramics according to their compositions and synthesis methods.

Table 1.2 Some synthesis methods of zirconia, titania and alumina nanocrystalline bioceramics.

Material	Year	Synthesis Method	Grain Size	Reference #
ZrO_2	1998	Nitrate-citrate combustion route	10-100nm	[11]
	1998	Nitrate-citrate gel route	10-20nm	[12]
	2000	Pechini process	10nm	[13]
	2001	Co-precipitation	10-20nm	[14]
	2004	Chemical co-precipitation	10-13nm	[15]
	2004	Agglomeration	12nm	[16]
TiO_2	1995	Sintering	15nm	[17]
	1999	High P and low T sintering	38nm	[18]
	2004	High pressure sintering	<100nm	[19]
	2005	Sol-gel	<60nm	[20]
	2006	Chemical vapor synthesis route (CVS)	<100nm	[21]
Al_2O_3	2004	Hot pressing	~300nm	[22]
	2005	Plasma Engineering	0.2μm	[23]
	2006	Flame spray pyrolysis	<100nm	[24]
	2007	High temperature and pressure sintering	~600nm	[25]

1.3 Calcium Phosphates

Calcium phosphates are the salts of the tribasic phosphoric acid (H_3PO_4) and they can form compounds containing $H_2PO_4^-$, HPO_4^{2-}, PO_4^{3-} ions. The compounds with $H_2PO_4^-$ ions normally are not found in biological systems because they form under acidic conditions [26]. However, both HPO_4^{2-} and PO_4^{3-} can occur in the mineral of bone and teeth. The hydrated CaPs contain OH^- ions and they belong to the basic apatitic CaP family [26]. Table 1.3 represents a list of various calcium phosphates and their chemical formulas.

Table 1.3 Abbreviations for various calcium phosphates [26].

Abbreviation	Ca/P ratio	Explanation
HAp	10/6	Hydroxyapatite, $Ca_{10}(PO_4)_6(OH)_2$.
FAp	10/6	Fluorapatite, $Ca_{10}(PO_4)_6F_2$.
ClAp	10/6	Chloroapatite, $Ca_{10}(PO_4)_6Cl_2$.
MCPM	1/2	Monocalcium phosphate monohydrate, $Ca(H_2PO_4)_2{\cdot}H_2O$.
MCPA	1/2	Monocalcium phosphate anhydrous, $Ca(H_2PO_4)_2$.
TTCP	2	Tetracalcium phosphate, $Ca_4P_2O_9$.
β-TCP	3/2	Tri-calcium-phosphate, β-$Ca_3(PO_4)_2$ without structural HPO_4^{2-} or Mg^{2+} ions.
Mg whitlockite	-	β-TCP like precipitates with structural HPO_4^{2-} or Mg^{2+} ions.
ACP	-	Amorphous calcium phosphate.

Table 1.3 (continued)

Abbreviation	Ca/P ratio	Explanation
ACa,Mg,CO_3P	-	As above, but containing Mg^{2+} and CO_3^{2-} (and HCO_3^-) ions.
α-TCP	3/2	α-tricalcium phosphate, α-$Ca_3(PO_4)_2$.
OCP	8/6	Octacalcium phosphate, $Ca_8H_2(PO_4)_6{\cdot}5H_2O$.
DCPD	1	Dicalcium phosphate dihydrate, $CaHPO_4{\cdot}2\ H_2O$.
DCPA	1	Dicalcium phosphate anhydrous, $CaHPO_4$.

Unless doped with a colored ion, all CaPs are white solids. CaPs can also occur as minerals and the most important of these minerals are the apatites. They are generally used as hard tissue implants such as coatings on metal prosthesis or in composites [26]. It has been reported that during the biomineralization process, the biological apatites form via an OCP intermediate, which has proven to be as one of the modes for the formation of HAp in model aqueous systems [27,28]. The physical properties of various phases of calcium phosphates and apatites are given in Table 1.4.

Table 1.4 Physical property of various phases of calcium phosphate bioceramics and apatites.

Phases	Chemical formula	Ca/P ratio	Crystal structure	Lattice constants	Density (g/cm^3)	Ref. #
HAp	$Ca_{10}(PO_4)_6(OH)_2$	10/6	Hexagonal, $P6_3/m$ space group.	a=b=9.417Å c=6.8814 Å	3.156	[26]
α-TCP	$Ca_3(PO_4)_2$	3/2	Monoclinic, $P2_1/a$ space group.	a=12.887 Å b=27.280 Å c=15.219 Å β=126.20º	2.86	[29,30]
β-TCP	$Ca_3(PO_4)_2$	3/2	Rhombohedral, space group R3cH.	a=b=10.43Å c=37.375 Å α=β=90º γ=120º	3.07	[29,30]
TTCP	$Ca_4P_2O_9$	2/1	Monoclinic, space group $P2_1$.	a=7.023 Å b=11.986 Å c=9.473 Å β=90.90º	3.05	[29,30]
FAp	$Ca_{10}(PO_4)_6F_2$	10/6	Hexagonal, $P6_3/m$ space group	a=9.367 Å c=6.884 Å	3.202	[31,32]
ClAp	$Ca_{10}(PO_4)_6Cl_2$	10/6	Hexagonal, $P6_3/m$ space group	a=9.628 Å c=6.764 Å	3.185	[33,34]
BrAp	$Ca_{10}(PO_4)_6Br_2$	10/6	Hexagonal, $P6_3/m$ space group	a=9.761 Å c=6.739 Å	3.376	[35]

Table 1.4 (continued)

Phases	Chemical formula	Ca/P ratio	Crystal structure	Lattice constants	Density (g/cm^3)	Ref. #
A-CO_3Ap	-	-	Hexagonal, $P6_3/m$ space group	a=9.557 Å c=6.872 Å	3.160	[36]
BaHAp	$Ba_5(PO_4)_3(OH)$	-	Hexagonal, $P6_3/m$ space group	a=10.177 Å c=7.731 Å	4.735	[37]
SrHAp	$(Sr,Ca)_5(PO_4)_3(F,OH)$	-	Hexagonal-Dipyramidal, $P6_3/m$ space group	a=9.565 Å c=7.115 Å	3.74	[38]
CdHAp	$Cd_5(PO_4)_3OH$	-	Hexagonal, $P6_3/m$ space group	a=9.335 Å c=6.664 Å	5.694	[39]
PbHAp	$Pb_{10}(PO_4)_6(OH)_2$	-	Hexagonal, $P6_3/m$ space group	a=b=9.866 Å c=7.426 Å	-	[40]

1.4 Apatites

The name “apatite” describes a family of compounds having similar structure (hexagonal system, space group, $P6_3/m$) with the general chemical formula $X_{10}(YO_4)_6Z_2$. Because the apatite structure is very tolerant to substitutions, X can be partly or completely replaced by Ca^{2+}, Ba^{2+}, Sr^{2+}, Pb^{2+}, Cd^{2+} ions and YO_4 can be replaced by PO_4^{3-}, AsO_4^{3-}, VO_4^{3-}, SiO_4^{4-}, CO_3^{2-} ions whereas, Z can be F^-, OH^-, Cl^- or CO_3^{2-} ions [26,41,42]. These substituents are summarized in Table 1.5.

Table 1.5 Various ionic substitutions to apatites.

Chemical Formula	**X**	**YO_4**	**Z**
$X_{10}(YO_4)_6Z_2$	Ca^{2+}, Ba^{2+}, Sr^{2+}, Pb^{2+}, Cd^{2+}, Mg^{2+}	PO_4^{3-}, AsO_4^{3-},VO_4^{3-}, SiO_4^{4-}, CO_3^{2-}	F^-,OH^-, Cl^-, CO_3^{2-}

Chemical substituents to the crystal structure of these apatites lead to a variety of species in this group [43]. Table 1.4 shows the lattice parameters and densities of various synthetic apatites.

Apatite is also well known as the main inorganic constituent of hard tissues of human and animals [42]. Carbonate containing HAp-like salt forms the minerals of bones and teeth. Biological apatites have nonstochiometric structures with vacant lattice sites, which considerably complicate their crystal structure. Some lattice substitutions can result in the lowering of the symmetry and/or a slight distortion from the hexagonal structure [26].

Biological apatites are poorly crystalline, which might be due to the presence of carbonate ions. Because they are known to have an essential influence on the growth of apatite crystals in solution; resulting in smaller crystals or even amorphous products. Mg^{2+} ions have also the similar effect on the growth of apatite crystals [26]. The typical composition of the inorganic components and Ca/P ratios of bone, enamel and dentin are shown in Table 1.6.

Table 1.6 Composition of the inorganic components by weight % of bone, enamel and dentin [44,45].

Component	Enamel	Dentine	Bone (cortical)
Ca	37.6	40.3	36.6
P	18.3	18.6	17.1
CO_3^{2-}	3.0	4.8	4.8
Na	0.7	0.1	1.0
K	0.05	0.07	0.07
Mg	0.2	1.1	0.6
Sr	0.03	0.04	0.05
Cl	0.4	0.27	0.1
F	0.01	0.07	0.1
Ca/P molar	1.59	1.67	1.65

These values above can show alterations from sample to sample; depending on the part of the tissue, species, maturation process, aging and disease [26]. From Table 1.6, it can be generally concluded that;

- The CO_3^{2-} contents of dentin and bone are similar but higher than that of the enamel
- The Mg amounts of bone and dentin are higher than those of enamel and it is twice as much in the dentin compared to the bone.
- Ca/P ratio of enamel is significantly lower than the stochiometric Ca/P ratio of 1.67 [26].

It is reported that as a result of the PO_4^{3-} replaced by CO_3^{2-} in human enamel, the Ca/P ratio is quite different from that in pure stochiometric HAp [46-48].

Among the CaPs and apatites, HAp has attracted a great deal of attention owing to its similarity to mineral part of bone.

1.5 Hydroxyapatite

Among various biocompatible materials, hydroxyapatite (HAp) has attracted an attention owing to its superior biocompatibility, bioactivity and similarity of its chemical composition to that of natural hard tissues. It can bond to bone and has been widely used as a bulk implant in non-load bearing areas of the body [49].

The stochiometric HAp has the general formula $Ca_{10}(PO_4)_6(OH)_2$ with a Ca/P ratio of 1.67. HAp has an hexagonal unit cell structure and belongs to the $P6_3/m$ space group. The atomic structure of typical HAp with a $P6_3/m$ space group is illustrated in Figure 1.3. Large and open circles represent the oxygen in OH^- and PO_4^{3-} groups, respectively and large and small solid circles are phosphorus in the PO_4^{3-} group and hydrogen in the OH^- group, respectively and double line circle represents the calcium ion [46].

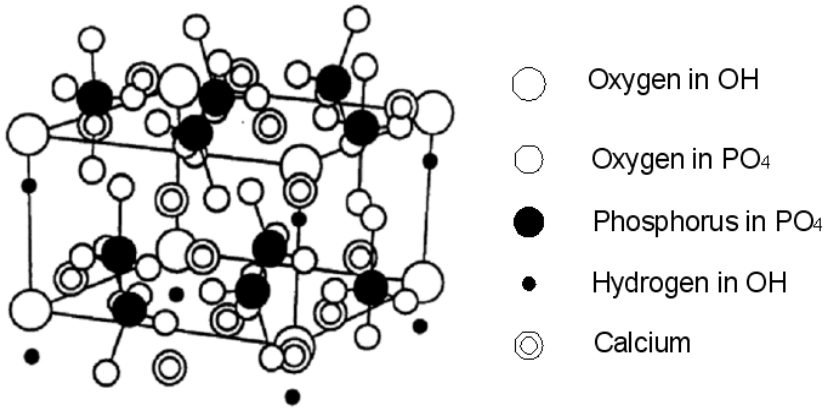

Figure 1.3 The atomic structure of typical HAp with a $P6_3/m$ space group [46].

It is reported that HAp promotes rapid bone growth and bonding between bone tissue and the implant surface. Moreover, it is known as a substrate for

effective adhesion of proteins, peptides, lipids, bacteria and strains [50,51]. It is also reported that HAp has the most stable phase above pH 4.3, which makes it more attractive among the Ca-P family for applications in the human body [4]. Due to these properties, HAp has been used for a variety of biomedical applications including matrices for drug release control [4,52] and also as coatings on orthopedic and dental implants [26,53]. However, because of its poor mechanical properties such as strength, hardness and fracture toughness, the application of HAp is limited to the non-load bearing areas [54]; such as, ossicles in middle ear [55].

1.5.1 Synthesis Methods

In order to synthesize HAp, various synthesis methods such as solid state reaction, wet chemical method, precipitation method, hydrothermal method, gel growth method, sol-gel method, alkoxide and other chemical methods have been used and as for the coating purposes in biomedical applications, chemical vapor deposition (CVD), plasma spray method and the other electrochemical methods have been used [42]. Some of the most commonly used methods are briefly explained below.

The solid state method, which takes place at high temperatures, has generally been used for the processing of ceramic powders and for studying their phase stabilities. However, powders synthesized by this method usually have irregular forms and large grain sizes [42].

Wet chemical method, has also been frequently used for the synthesis of HAp at relatively low temperatures. However, the powders prepared by this method were found to be poorly crystallized, inhomogenous in composition and irregularly formed [42].

Hydrothermal method was also used to produce nano-HAp. The difference of this method from the commercial precipitation method is that, it requires high temperature and high pressure during synthesis. By this method, well crystallized, homogenuos, uniform and easily sinterable powders could be produced [42].

However, by this method, small amounts can be produced in the laboratory. It has a limited commercial use and is moderately expensive.

By sol-gel method, improved chemical homogeneity due to the molecular level mixing of the precursors and reducing the synthesis temperature is possible [4]. However, during drying, cracks might occur due to the capillary forces.

Hydrolysis is another method to synthesize HAp, which requires low temperatures and occurs with water uptake of acidic CaPs (Ca/P< 1.67). However, in most cases the hydrolysis product is highly non-stochiometric [56].

All these methods have some advantages and disadvantages. But among them, precipitation method is a cheaper method, which is also fundamental to all solution processes. HAp with particle sizes ranging from nanometers to milimeters can be produced in large amounts more easily. By controling the processing parameters such as temperature and pH, nano-HAp powders can be produced. Table 1.7 presents a chronological development of nano-HAp synthesis methods during the recent years and their production methods.

Table 1.7 Synthesis of nano-HAp- chronological development.

Year	**Process**	**Reference #**
2000	Preperation of nano-HAp by pressure assisted sintering (grain size ~100 nm).	[57]
2002	Preperation of nano size HAp particles and HAp/chitosan nano composite.	[58]
2002	Direct precipitation of HAp from dilute calcium chloride and sodium phosphate solutions.	[59]
2003	Nanosize HAp powders produced in radio frequency (rf) thermal plasma (nano HAp grain size 10-100 nm).	[50]

Table 1.7 (continued)

Year	Process	Reference
2003	Nano HAp is produced by sol-gel process, using equimolar solutions of $Ca(NO_3)_2 \cdot 4H_2O$ and $(NH_4)_2HPO_4$ dissolved in ethanol solvent.	[60]
2003	Chemical precipitation through aqueous solutions of calcium chloride and ammonium hydrogen phosphate.	[61]
2003	Mechanochemical synthesis of nano-HAp and TCP powders using calcium hydrogen phosphate ($CaHPO_4 \cdot 2H_2O$) and CaO as precursors.	[62]
2003	Synthesis of nano HAp by sucrose templated sol-gel method.	[63]
2004	Synthesis of nano HAp using hydrolysis method by hydrolysis of DCPD and CaO with 2,5 M NaOH(aq).	[64]
2007	Synthesis of nanocrystalline HAp by precipitation method.	[56]
2007	Synthesis of nanocrystalline HAp by using wet chemical route.	[65]
2008	Synthesis of nano HAp under a sonochemical/ hydrothermal condition.	[66]

1.5.2 Phase Transformations

HAp decomposes to secondary phases such as TCP and TTCP upon sintering at high temperatures [67]. It has been reported that the decomposition of HAp starts at about 1300ºC, which is accompanied by the deterioration of

mechanical properties of HAps [65,68,69]. The thermal decomposition occurs in two steps i.e. dehydroxylation (Equation 1.1) and decomposition (Equation 1.2).

HAp dehydroxylates to oxyhydroxyapatite by a fully reversible reaction at temperatures around 850-900ºC [65,67].

$$Ca_{10}(PO_4)_6(OH)_2 \rightarrow Ca_{10}(PO_4)_6(OH)_{2-2x}O_x + xH_2O_{gas} \quad (1.1)$$

The decomposition of HAp to TCP and TTCP takes place at temperatures higher than 900ºC.

$$Ca_{10}(PO_4)_6(OH)_2 \rightarrow 2Ca_3(PO_4)_2 + Ca_4P_2O_9 + H_2O_{gas} \quad (1.2)$$

The decomposition of HAp was also reported by the following reaction [53]:

$$Ca_{10}(PO_4)_6(OH)_2 \rightarrow 3Ca_3(PO_4)_2 + CaO + H_2O \quad (1.3)$$

Although the transition temperatures of HAp can be experimentally measured, it should be strongly emphasized that phase transition temperatures can change depending on the nature of the starting synthesized powders and the relative humidity in the furnace [65].

Since both dehydroxylation and decomposition reactions include water vapor, the rates of these reactions depend on the humidity in the furnace. In the presence of humidity, the decomposition rate slows down by preventing the dehydration of the OH^- group.

As a result, formation of second phases upon sintering can be suppressed by controlling the moisture content in the sintering environment and in addition, adding the sintering additives into HAp can also prevent the formation of second phases [65].

1.5.3 Mechanical Properties

Sintered HAp exhibits poor mechanical properties owing to its brittle nature, low fracture toughness (< 1 $MPa \cdot m^{1/2}$) and low ductility [65]. Also it was reported that the decomposition of HAp causes further reduction in its mechanical properties [53].

Another shortcoming of the HAp is the elastic modulus mismatch with natural bone tissues. HAp has a much higher elastic modulus (~ 130 GPa [70]) than

bone (~17.50 GPa for trabecular bone and for cortical bone ~20.55 GPa (longitudinal) [71]), which leads to greater stress concentration and fracture at the bone and material interface [72]. However, it has also been reported that the Young's modulus value of HAp sintered at 1000ºC was higher than 100 GPa with a bulk density up to higher than the 98 % of the theoretical value [65].

Due to various insufficient properties of HAp, many attempts and studies have been performed to improve both its mechanical and biological properties by producing nano-sized HAp and doping the HAp with various ions.

Porous structure, which provides a network for the ingrowth of bone tissue and accelerates the replacement of the material by bone tissue, is also an important parameter in affecting the mechanical properties of HAp [72-74]. The effects of porosity on the relative elastic modulus and hardness of the HAp have been investigated and it is reported that the elastic modulus and hardness of the HAp exhibited an exponential relationship with the porosity [72].

1.5.4 Nano-Hydroxyapatite

HAp with nano grain size would be more desirable in clinical applications due to its similarity to the nano structure of bone [50]. As a result of its greater surface area, nanocrystalline HAp exhibits improved sinterability and densification, which also improve the fracture toughness and other mechanical properties of this material [57]. In Table 1.8, mechanical properties of nanostructured HAp are compared with those of conventional HAp, dental enamel and compact bone.

Table 1.8 Mechanical properties of nano HAp compared to conventional HAp, dental enamel and compact bone.

Sample	Compressive Strength (MPa)	Bending Strength (MPa)	Fracture Toughness ($MPa \cdot m^{1/2}$)	Elastic Modulus (GPa)	Reference #
Nano structured HAp	879	193	1.3	78-106	[57,65]
Conventional HAp	120-800	38-113	1	~100	[70,75,76, 77]
Dental enamel	95-370	76	0.7-1.3	60	[70,78,79]
Compact bone	170-193	160	2-12	8-24	[70,78]

Nano HAp is expected to have better bioactivity than the coarser grain sized HAps due to its similarity to the nano structure of bone [4,56]. Improving the various properties of HAp is possible by controlling the powder characteristics such as particle size, shape, particle distribution and agglomeration [56]. Nanocrystallized HAp can promote osteoblast adhesion and proliferation, osseointegration and the deposition of calcium containing minerals on its surface [50].

It has been reported that aging is also an important parameter in order to obtain crystalline HAp with a uniform morphology. Grains with non-uniform morphologies are redissolved and are recrystallized into more ordered forms during the aging process [57]. It was noted that for aging up to 100 hours, the samples synthesized by precipitation method became more stable against decomposition to second phases. Moreover, small crystalline sizes around 50 nm could be achieved for the HAp powders calcined at 550˚C which were verified by transmission electron microscopy (TEM) and x-ray diffraction (XRD) peak broadening analysis [57].

Effects of some important parameters such as precursor pH, aging time and temperature were examined in achieving nano-HAp particles with tailored composition, crystal size, morphology and surface chemistry to optimize their chemical stability, sinterability and mechanical properties [57]. The effects of these parameters are summarized in Table 1.9.

Table 1.9 Some important parameters in controlling crystal size, morphology, chemical stability and sinterability of HAp.

Parameters		**Resulting effects**
Aging time	As increases;	Smaller crystal sizes, more uniform morphology, reduction in phase decomposition during sintering.
Aging temperature	0˚C;	Highly non-stochiometric HAp, decomposed to coarser grained β-TCP during sintering.
	25˚C;	Stochiometric HAp, spherical morphology; increased sinterability.
	80˚C;	Whisker-like HAp particles with preferential growth along the <002> axis.
Precursor pH	As increases;	Preferential growth along the <002> axis of HAp, rod-like morphology, larger average particle size, non-stochiometric HAp, phase decomposition during sintering.
	As decreases;	Non-stochiometric HAp, phase decomposition during sintering.

1.6 Doping of HAp with Various Ions

Biological HAp crystals in vivo contain many ionic impurities such as; K^+, Mg^{2+}, Na^+, CO_3^{2-} and F^-, which usually reflect dietary history and exposure to hazards, such as Pb^{2+}, Sr^{2+}, Cd^{2+}, Cu^{2+} [80-83]. These substitutions alter the biological, mechanical and solubility properties of HAp [82]. To enhance the biological and mechanical properties of HAp, several researches have been focused on doping of HAp with various ions.

Doping of HAp with 2 mol % Zn^{2+} or 2 mol % Mg^{2+} increased the osteoblast adhesion [84]. In addition, the osteoblast adhesion for 2 mol % Y^{3+} doped HAp was 28% greater than that of the pure HAp [84]. Among the dopants of 5 wt % Mg^{2+}, Zn^{2+}, La^{3+}, Y^{3+}, In^{3+} and Bi^{3+}; following ions of Zn^{2+}, In^{3+}, Bi^{3+} were reported as the most effective dopants enhancing the osteoblast response to HAp [82].

In addition, it is reported that doping elements such as Na^+, K^+, Mg^{2+}, Sr^{2+}, Ba^{2+} and Pb^{2+} into HAp can lower the grain boundary energy [46]. These elements have a tendency to segregate into the grain boundary and they stabilize the grain boundary region by increasing the interaction between the atoms on the grain boundary [46]. The effective ionic radii for some of the substitution ions in apatites are given in Table 1.10.

Table 1.10 Effective ionic radii (Å) for some of the ions that partly or completely substitute in the apatites [85].

Mg^{2+}	CO^{2+}	Sb^{3+}	Fe^{2+}	Mn^{2+}	Y^{3+}	Eu^{3+}	Cd^{2+}
0.720	0.745	0.76	0.780	0.830	0.900	0.947	0.95
Nd^{3+}	Ca^{2+}	Na^{+}	La^{3+}	Sr^{2+}	Pb^{2+}	Ba^{2+}	K^{+}
0.983	1.00	1.02	1.032	1.84	1.19	1.35	1.38
Bi^{3+}	In^{3+}	Zn^{2+}	Cu^{2+}	Al^{3+}	-	-	-
1.03	0.80	0.74	0.73	0.535			
F^{-}	OH^{-}	O^{2-}	Cl^{-}	S^{2-}	Br^{-}	I^{-}	-
1.33	1.37	1.40	1.81	1.84	1.96	2.20	
C^{4+}	P^{5+}	Si^{4+}	Mn^{5+}	As^{5+}	Cr^{5+}	V^{5+}	Ge^{5+}
0.16	0.17	0.26	0.33	0.335	0.345	0.355	0.390

Especially, Pb^{2+} ion drastically lowers the grain boundary energy and Pb^{2+} ion segregated on the grain boundary has an apparent effect in reducing the grain size [46]. The effects of Sr^{2+} [86], Li^{+} [87], pyrophosphate, citrate and Mg^{2+} [88] ions on the crystal growth of HAp have also been studied [26]. It is reported that although the Sr/Ca ratio was much lower than it is in the solution, significant amounts of Sr^{2+} ion incorporation into the lattice is achieved [86]. Increased Li^{+} ions up to ~40 ppm reduced the rate of crystallization significantly [87]. At higher pH values, pyrophosphate and citrate ions showed an increase while Mg^{2+} ions showed a decrease in effectiveness as inhibitors of crystal growth [26]. It is reported that, the presence of CO_3^{2-} (and F^{-}) ions increases the uptake of Mg^{2+} ions in HAp synthesized in aqueous systems [26,89].

1.6.1 Effect of Magnesium Ions

Mg^{2+} is one of the most important bivalent ions, which has an important factor in determining the bone fragility. In bone tissue, Mg^{2+} ion stimulates the transformation of immature bone into a mature form. The translocation of Mg^{2+} into mineral tissues prevents fractures by increasing bone elasticity [90,91].

It has been reported that doping low amounts (0.5-0.05 wt%) of either Mg^{2+} or F^- ions increased in vivo stability and thus decreased the solubility of HAp [92].

The Mg^{2+} ion content of the natural apatite is around 6 mol% but the Mg content can be changed depending on the aging. It is contained in high concentrations in the cartilage and bone tissues during the initial phases of osteogenesis and it tends to disappear when the bone tissue becomes mature [93]. It is also reported that the existence of Mg^{2+} ion results in acceleration of the nucleation kinetics and inhibits the crystallization process [94-96].

Mg^{2+} ion deficiency affects all stages of skeletal metabolism causing cessation of bone growth, decrease of osteoblastic and osteoclastic activities, ostepenia and bone fragility. Therefore, Mg^{2+} ion incorporation into the HAp structure is of great interest in developing of artificial bone substitutes [97].

Mg^{2+} ions can substitude for Ca^{2+} ions in the HAp structure and inhibites CaP precipitation because it is mainly adsorbed on the crystalline surface of HAp. For that reason, the amount of Mg^{2+} ions associated to HAp surface is usually much more than the Mg^{2+} ions, which are incorporated into its crystalline structure [42]. Moreover, the incorporation of Mg^{2+} ions into the precipitated CaP phase was supported by XRD analysis of the sintered samples in which the formation of Mg^{2+}-containing whitlockite $(Ca, Mg)_3(PO_4)_2$ was verified [98].

It is reported that the ions that are larger than Ca^{2+} ions, can be completely substituted for calcium sites in the HAp [99]. However in the case of Mg^{2+} ion substitution into HAp, it is difficult to protect the phase purity. The Mg^{2+} ion substituted HAp becomes unstable upon sintering [99]. Due to the difference in the atomic radiis of Mg^{2+} and Ca^{2+} ions (Table 1.10), doping of Mg^{2+} ions into HAp

causes contraction in the hexagonal unit cell volume and reduction in the mean crystal size.

To increase the stability of the structure and to decrease the subsequent phase decomposition (formation of TCP besides HAp) during sintering, co-substitution of a second ion, especially substituting CO_3^{2-} group is a simple way of decreasing the decomposition of HAp [100].

Mg^{2+} ions stabilize the β-TCP upon sintering above 800ºC along with the formation of HAp phase and improves the thermal stability of TCP [91,101]. Moreover, Mg^{2+} ions improve densification behavior of TCP, stabilize the cell-material interface, improve cell attachment and growth and also reduce the resorption and solubility of TCP [101,102].

It is reported [84] that doping 5 wt% Mg into HAp resulted in mechanical properties (such as compressive strength [103]) comparable to those of physiological bone (e.g., 170 MPa for human femur [81]).

Mg^{2+} ion is the activator of more than 300 enzymes in the body while fluoride is known as their inhibitor. However, it is known that the activities of some enzymes are to be increased by fluoride. The greatest practical significance of Mg-F interaction is in the processes of bone and tooth mineralization, and in the formation of uroliths [90].

1.6.2 Effect of Fluoride Ions

Fluoride has been widely added into HAp to improve its thermal stability and biological properties. Fluoride substituted in HAp influences the physical and biological characteristics of HAp [90].

Fluoride ions affect enamel hardening and prevent its annealing but this effect diminishes after the addition of Mg^{2+} ions. Mg alone does not visibly affect tooth plaque, erosive enamel damage, or the course of caries but Mg^{2+} and F^- ions together influence the enamel hardening and prevent the risk of dental caries significantly.

In interactions of F^- with Mg^{2+} and Ca^{2+}, it should be emphasized that it is the calcium rather than magnesium that intensifies the mineralization processes [90]. Fluoride ions are present in saliva and blood plasma and they are required for normal dental and skeletal development. They increase the crystal sizes of HAp along the c-axis direction [10]. Fluoride ions also improve the thermal stability of HAps [104]. Moreover, fluoride substituted in HAp influences the physical and biological characteristics of HAp and stimulates proliferation and differentiation of bone cells. It is reported that the structural energy of F^- is much lower than that of other atoms. Therefore, F^- is very stable in the lattice sites and doping F^- ions can stabilize the crystal structure of HAp [46]. The presence of F^- ions also has a reducing effect on the acid dissolution of HAp [26].

1.7 Tri-calcium Phosphates

Among the CaPs, TCP has gained great importance as bone cement and implant material in biomedical applications due to its close similarity to the inorganic component of the bone, its resorbability and excellent osseoconductive properties [101].

TCP ($Ca_3(PO_4)_2$) is a bioactive and biodegradable material, which has four polymorphs; β, α, α′ and a high pressure form γ phase, which is obtained by heating β-TCP at 950˚C under a high pressure of 4 GPa [105]. Among the four polymorphs of TCP, α′ and γ phases are difficult to prepare because they need high temperatures or high pressures and the α polymorph has a high reactivity problem which results in rapid degradation in vitro [99]. β-TCP is a slow degrading and bioresorbable CaP ceramic. Therefore, the investigations have also been focused on β-TCP as a bioactive material [4].

TCP has poor mechanical properties like brittleness and insufficient densification behavior. Transformation from β- to α- phase prevents the TCP from further densification and also expansion of the crystal unit cell volume during this phase transition causes micro-cracks in the structure, which reduces the mechanical strength of the material [101,106].

β phase is stable below 1125˚C and the α phase is stable in the range of 1125- 1430 ˚C and above 1430 ˚C the α´ phase becomes stable [107]. Different phases can be used in different applications depending on whether a bioresorbable or a bioactive material is desired [4]. Physical properties of the α and β phases of TCP are summarized in Table 1.4.

While degrading in the host, TCP is replaced by the regenerating bone and acts as a seed for the new bone and as a supplier of the Ca^{2+} and PO_4^{3-} ions [108]. It was reported that TCP is more degradable than HAp, which shows minimum degradability properties; preventing the bone ingrowth for extended periods [109]. Because of the higher resorption rates of TCP, strength reduction occurs in the bone-implant interface. Therefore, the dissolution behavior of TCP should be controlled by chemical modifications. Doping it with trace elements such as Mg is one of the approaches in controlling the dissolution behavior of TCP and also stabilizing the β-TCP phase at elevated temperatures above 1125˚C [99,108].

Because of the advantages of nanosized materials that are discussed previously, nano sized β-TCP ceramics are also being investigated. Nanosized β-TCP exhibits significant biological affinity and activity and it responds very well to physiological environments. It has been reported that the value of Young's modulus in nano-β-TCP ceramics is 21 GPa [4]. Nano-β-TCP cements can also serve as drug delivery systems for variable drugs such as antibiotics, anti-tumor and anti-inflammatory drugs [110].

1.8 Nano Structure of Bone

Bone is a hierarchical composite that consists of minerals deposited in an oriented fashion in a collagen backbone [111]. Bone consists of 65% mineral, 25% organic matrix, cells and water. The bone mineral is in the form of small crystals in the shape of needles, plates and rods located within and between the collagen fibers. The organic matrix, which is synthesized and secreted by the osteoblasts, consists of 90% collagen and about 10% of various noncollagenous proteins [112]. The mineral

component provides both the mechanical strength of bone and the ability to regulate mineral ion homeostasis.

The bone mineral consists of tiny HAp crystals that are deposited within and between the collagen type I fibrils to form an inorganic/organic composite structure [113,114]. Bone mineral is a poorly crystalline HAp, containing constituents such as carbonate, citrate, magnesium, fluoride and strontium incorporated in the crystal lattice or absorbed on the crystal surface [111,112].

Type 1 collagen, that is predominantly present in the bone, provides the structural framework in which the HAp platelets are inserted. The calcification is initiated within the gap regions of the fibers by the formation of HAp platelets. Bone mineral growth and proliferation are controlled by the spatial limitation of the collagen fibers and by the absorption of matrix proteins [112].

The basic building block of the bone mineral is the mineralized collagen type1 fibril of about 100 nm in diameter. The osteoblasts deposits the triphelical collagen molecule into the extra cellular space and the 300 nm long and ~1.5 nm thick molecules build fibrils by a self-assembling process. The mineral particles are believed to be nucleated with a 67 nm periodicity in the collagen matrix [115], which is illustrated in Figure 1.4.

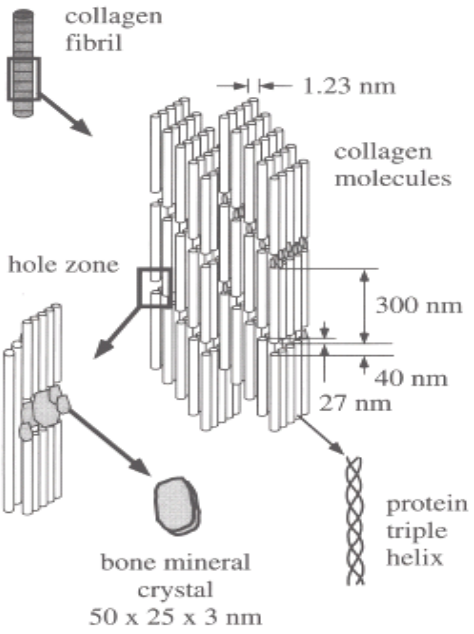

Figure 1.4 An illustration of collagen fibrils, fibers and bone mineral crystals [116].

The plate-like apatite crystals with a length and width of 50x25 nm and a crystal thickness of 2-3 nm occur within the discrete spaces of the collagen fibrils by which the crystal growth is limited and forced to be discrete and discontinuous [111, 112, 116].

1.9 Aim of This Study

The objective of this study was to investigate the microstructural and the mechanical properties of pure and Mg^{2+} and F^- ions doped nano-CaPs. Pure and doped nano-CaPs were synthesized by a precipitation method. Powders were cold pressed and sintered at 1100°C for 1 hour. Different Ca/P ratios and CaP powders doped with various amounts of Mg^{2+} and F^- were studied. XRD, SEM, and FTIR methods were used to investigate the microstructural features. Moreover, micro-hardness and diametral strength of the materials were determined. By doping of

ions, an enhancement in the strengths and micro hardness values of the CaPs was aimed in this study.

The amount and ratios of Ca/P and the dopants were investigated as seperate parameters and the affect of each parameter on CaPs were studied in detail.

CHAPTER 2

MATERIALS AND METHODS

2.1 Materials

Calcium nitrate tetra hydrate ($Ca(NO_3)_2 \cdot 4H_2O$) and di-ammonium hydrogen phosphate ($(NH_4)_2HPO_4$) Merck, Germany were used as precursors. In order to prepare Mg^{2+} and F^- doped CaPs, magnesium nitrate ($Mg(NO_3)_2 \cdot 6H_2O$) and ammonium fluoride (NH_4F) Aldrich, USA were used. Ammonia solution (Merck, Germany) was also used to adjust the pH values of the solutions.

2.2 Synthesis Method of Nano-CaPs

2.2.1 Synthesis of Pure CaPs

Nano-CaP was synthesized by a precipitation method [117]. Calcium nitrate tetra hydrate and di-ammonium hydrogen phosphate are used as precursors. Two different solutions were prepared separately in distilled water by using 0.5 M $Ca(NO_3)_2 \cdot 4H_2O$ and 0.3 M $(NH_4)_2HPO_4$ precursors and they were mixed with each other to obtain pure HAp (Ca/P=1.67). Additionally, the Ca-P precursors were mixed to obtain the CaP ratios of 2.00, 1.50 and 1.20 to obtain the compositions that are listed in Table 2.1.

Table 2.1 List of the synthesized products.

Group No	Sample ID	Ca/P	Mg	F
1	2Mg0F0	2.00	-	-
	1.67Mg0F0	1.67	-	-
	1.5Mg0F0	1.50	-	-
	1.2Mg0F0	1.20	-	-
2	1.95Mg2.5F2.5	1.95	2.5	2.5
	1.625Mg2.5F2.5	1.625	2.5	2.5
	1.463Mg2.5F2.5	1.463	2.5	2.5
	1.17Mg2.5F2.5	1.17	2.5	2.5
3	1.65Mg1F2.5	1.65	1	2.5
	1.625Mg2.5F2.5	1.625	2.5	2.5
	1.542Mg7.5F2.5	1.542	7.5	2.5
4	1.65Mg1F0	1.65	1	-
	1.625Mg2.5F0	1.625	2.5	-
	1.542Mg7.5F0	1.542	7.5	-
5	1.625Mg2.5F0	1.625	2.5	-
	1.625Mg2.5F2.5	1.625	2.5	2.5
	1.625Mg2.5F7.5	1.625	2.5	7.5

As-prepared solutions were stirred for one hour. After one hour of stirring, ammonia solution was added into both solutions to bring the pH level to ~11. Then,

the calcium nitrate solution was poured dropwise into the di-ammonium hydrogen phosphate solution. A milky and denser solution was obtained at the end of the mixing. This final mixture had a pH level around 11-12 with the addition of ammonia solution. After 2-3 hours of stirring, the mixture was heated until the boiling in order to increase the reaction rate and to obtain a homogenous solution. After the boiling, the solution was left to stirring for one day at room temperature (RT). After the stirring, the mixture was filtered by a fine filter paper. At the end of this process, the obtained wet cake was dried over night in an oven at 200^{o}C to remove excess water. After the drying, calcination was performed at 600^{o}C for 15 minutes.

After the calcination, the ceramic powders were crushed with a mortar and pestle to obtain a fine powder with a reduced particle size and homogenous distribution. Doped and undoped powders were cold pressed into a 13 mm diameter die at 30 MPa for 60 seconds. 10 disks were prepared for each composition. Then the samples were air sintered at 1100^{o}C for 1 hour and cooled to RT in the furnace.

2.2.2 Synthesis of Mg^{2+}& F^{-} Doped Calcium Phosphates

The main CaP precursors and the synthesis technique were the same for the production of the doped samples. Additionally, magnesium nitrate and ammonium-fluoride were used as Mg^{2+} and F^{-} sources.

The amounts of the dopants were adjusted according to their mole % to that of Ca^{2+} used in the production. The mole % of the dopants were presented in Table 2.1. Magnesium nitrate was added into calcium nitrate solution in 1, 2.5 and 7.5 moles % of calcium nitrate and ammonium fluoride was added into di-ammonium phosphate solution in the compositions of 2.5 and 7.5 moles % of calcium nitrate. Ca/P ratios presented in this table were the first mixing ratios of the CaP precursors adjusted for the Ca/P ratios of 2.00, 1.67, 1.50 and 1.20. As the Mg^{2+} ion amount increased, the Ca/P ratios of the samples were decreased. The groups that were synthesized are summarized in Table 2.1. The compositions in group 1 were produced as the control samples for comparing the results to the ones in groups 2, 3, 4 and 5.

2.3 Characterization Methods

2.3.1 Structural Analysis

2.3.1.1 Density

The densities of the disks were measured by geometrical method. Powders were cold-pressed after the calcination at 600 ºC for 15 minutes. 10 disks were prepared for each sample. After measuring the average green densities, the disks were air-sintered in the furnace at 1100 ºC for 1 hr and they were cooled in the furnace to RT. After the sintering, the bulk densities of the samples were measured and the average value was taken as the sintered density. Volume and densities of the samples were determined by the formulas below;

$$V = \left(\pi \cdot \frac{D^2}{4} \right) \cdot t \tag{2.1}$$

$$\mathrm{d} = \frac{\mathrm{w}}{\mathrm{V}} \tag{2.2}$$

where;

V= disc volume; t= disc thickness; D= disc diameter; w= weight; d= density.

Additionally, in order to improve the densification of the samples during sintering, the as dried samples were directly sintered at 1100ºC for 1 hr without crushing to powder form. The density measurements of these pieces were taken by Archimedes method and these samples were used for the μ-hardness measurements. The dried and sintered pieces of the samples' densities were measured by the following formula:

$$Density\,(g/cm^3) = \frac{Wt_{(air)}}{Wt_{(air)} - Wt_{(water)}} \times \rho_{(water)} \tag{2.3}$$

where;

$\rho_{(water)}$: density of water; $Wt_{(air)}$: dry weight of the sample; $Wt_{(water)}$: wet weight of the sample.

The theoretical densities of HAp and β-TCP are 3.156 g/cm^3 and 3.07 g/cm^3, respectively. The theoretical densities (ρ_t) of the HAp/ β-TCP composites were calculated according to their weight percentages (wt% of HAp and wt% of β-TCP, which were calculated from the ratios of the most intense XRD peaks of the phases) in the samples by the following formula [118];

$$\rho_t = \frac{1}{\frac{W_{\beta\text{-TCP}}}{3.07} + \frac{W_{HAp}}{3.156}} \tag{2.4}$$

The relative densities (ρ) were calculated by dividing the measured bulk densities (ρ_{bulk}) to the theoretical densities (ρ_t).

2.3.1.2 X-Ray Diffraction Analysis

XRD was performed to study the presence and amounts of the phases, lattice parameters of the samples. A Rigaku DMAX 2200 machine was used with a Cu-Kα radiation at 40 kV/ 40 mA and the samples were scanned from 10^o to 80^o in 2θ angles with a scan speed of 2.0^o /min. Results were compared with the Joint Committee on Powder Diffraction Standards (JCPDS) files for HAp (#09-0432) [119] and β-TCP (#09-0169) [120].

2.3.1.2.1 Phase Determination

The amount of phases present in pure and doped CaPs was calculated by using the relative intensity measurements of highest diffracted peaks by the following formulas [121];

$$\frac{W_{HAp}}{W_{\beta-TCP}} = \frac{R}{R_0} = \frac{I_H / I_{\beta-TCP}}{1.755} \tag{2.5}$$

$$W_{HAp} + W_{\beta-TCP} = 1 \tag{2.6}$$

where; W_{HAp} and $W_{\beta-TCP}$ are the amounts by weight % of the phases. R is the ratio of the intensities of the HAp (I_H) to that of β-TCP ($I_{\beta-TCP}$) measured from the

XRD peaks. The ratio R_0 of the peak heights of HAp to that of β-TCP was taken as 1.755 [121].

2.3.1.2.2 Lattice Parameter Measurements

The hexagonal lattice parameters of pure and doped HAp/β-TCP samples were calculated by successive approximations method [122]. The lattice parameters of the rhombohedral β-TCP were expressed in the hexagonal setting. The unit cell volumes of HAp and β-TCP were calculated by the following formulas, respectively:

$$V = 2.589 \cdot a^2 \cdot c \tag{2.7}$$

$$V = 0.866 \cdot a^2 \cdot c \tag{2.8}$$

where; V ($Å^3$) is the volume of unit cell, a and c are the hexagonal lattice parameters in Angstroms. 'a' and 'c' hexagonal lattice parameters of the samples were calculated based on the Bragg's equation according to the Equations 2.9 and 2.10 [122];

$$a_0 = \left(\frac{\lambda}{2\sin\theta}\right)\sqrt{\left(\frac{4}{3}(h^2 + hk + k^2) + \left(\frac{a}{c}\right)^2 l^2\right)} \tag{2.9}$$

$$c_0 = \left(\frac{\lambda}{2\sin\theta}\right)\sqrt{\left(\frac{4}{3}\left(\frac{c}{a}\right)^2 (h^2 + hk + k^2) + l^2\right)} \tag{2.10}$$

where;

a_0 and c_0: the calculated lattice parameters; λ : x-ray wavelength; θ: the Bragg angle for corresponding (hkl); a/c ratio: the last calculated ratio in successive approximation method.

Equation 2.9 was used for the calculation of 'a' values, in which the term "$\frac{4}{3}(h^2 + hk + k^2)$" was larger than "$\left(\frac{a}{c}\right)^2 l^2$". In addition, equation 2.10 was used for the calculation of 'c' values for the conditions, where "$h^2 + hk + k^2$" term was less than the value of "l^2".

2.3.2 Fourier Transform Infrared Spectroscopy

FTIR measurements were performed to identify the presence of bonds in the samples. Produced CaP powders and potassium bromide (KBr) were mixed by a weight ratio of 1 to 300. In order to prepare the samples for the analysis, transparent pellets were produced by cold pressing. A FTIR spectrometer, BioRad FTS 175C was used and the spectra records were performed from 4000 cm^{-1} to 500 cm^{-1} using 512 scan.

2.3.3 Scanning Electron Microscopy Analysis

SEM analysis was performed to determine the average grain sizes of the sintered samples. A QUANTA 400F Field Emission SEM at a voltage of 20 kV was used for the analysis. Firstly, the samples were coated with gold and platinum under vacuum. Grain sizes of the samples were determined by the intercept method within a 20 cm circumference circle. Following formula was used to determine the average grain sizes [123].

$$G_{av} = \frac{L}{N * M} \tag{2.11}$$

where:

G_{av} : Average grain size; L: circumference of the circle; N: number of the intersections along the intersection line; M: magnification.

2.4 Mechanical Testings

2.4.1 Vickers Micro-hardness

The Vickers micro-hardness measurements were determined by a Vickers micro hardness tester (HMV-2, Shimadzu, Japan). The samples were first polished step by step with SiC papers (Buehler Ltd., USA) from 600 to 1200 grades and then they were polished with a 1μm monocrystalline diamond suspension (Buehler Ltd., USA). Approximately 20 measurements were performed on each sample with a

diamond indenter at 200 g load. The average μ-hardness was calculated by the formula below [124];

$$HV = 0.001854\frac{P}{d^2} \tag{2.12}$$

where:

HV: Vickers hardness (GPa); P: Applied load (N); d: diagonal indent length (mm).

2.4.2 Diametral Strength

The diametral tensile strength of the sintered disks with varying ratios of HAp, β-TCP and the dopants were measured by a universal testing machine (LS500; Llyod Instruments, UK). The measurements were taken from 10 disks for each composition. Disks placed between two flat plates and compression was applied by a cylinder with a speed of 2mm/min. During the compression, a maximum tensile strength was generated across the flat surface diameters of the disks normal to the loading direction. The tensile strength of the samples were calculated with the following formula [125-127]:

$$S = \frac{2F}{\pi \cdot D \cdot t} \tag{2.13}$$

where:

F: failure force; D: sample diameter; t: sample thickness.

CHAPTER 3

RESULTS AND DISCUSSION

3.1 Density Results

Green and sintered densities of the disk shaped samples are presented in Table 3.1. The calculations were performed according to the Equations 2.1, 2.2 and 2.4. Although a high green density was achieved for sample 2Mg0F0, the relative sintered density of sample 2Mg0F0 was lower than that of sample 1.67Mg0F0. The samples in Table 3.1 were calcined at 600ºC and then the cold pressed samples were air sintered at 1100ºC for 1 hr. These samples were used for the diametral tensile strength tests.

By increasing the Mg content and therefore the β-TCP amount, the relative densities were decreased. It was reported that the densities of the Mg^{2+} ion substituted HAp samples were lower than that of the stochiometric HAp [128]. However, by the addition of F^- ions, the densification behavior of the samples was increased significantly for all groups.

Table 3.1 Green and sintered densities of the cold pressed disks.

Group No	Sample ID	Bulk Density (Green) (g/cm^3)	Relative Density % (Green)	Standard Deviation ($\pm g/cm^3$)	Bulk Density (Sintered) (g/cm^3)	Relative Density % (Sintered)	Standard Deviation ($\pm g/cm^3$)
1	2Mg0F0	1.72	54.4	0.018	2.76	87.5	0.033
	1.67Mg0F0	1.61	51.1	0.026	2.87	90.8	0.05
	1.5Mg0F0	1.41	45.6	0.012	2.79	90.1	0.049
	1.2Mg0F0	1.39	45.4	0.012	2.61	85.1	0.039
2	1.95Mg2.5F2.5	1.63	51.6	0.018	-	-	-
	1.625Mg2.5F2.5	1.55	49.4	0.009	2.85	90.5	0.057
	1.463Mg2.5F2.5	1.39	45.0	0.012	2.79	90.1	0.025
	1.17Mg2.5F2.5	1.35	43.8	0.009	2.48	80.7	0.032
3	1.65Mg1F2.5	1.52	48.2	0.009	2.88	91.3	0.039
	1.625Mg2.5F2.5	1.55	49.4	0.009	2.85	90.5	0.057
	1.542Mg7.5F2.5	1.50	48.2	0.015	2.40	77.1	0.059
4	1.65Mg1F0	1.53	48.6	0.01	2.83	89.6	0.069
	1.625Mg2.5F0	1.53	48.6	0.012	2.80	89.2	0.093
	1.542Mg7.5F0	1.62	52.0	0.06	2.53	81.1	0.095
5	1.625Mg2.5F0	1.53	48.6	0.012	2.80	89.2	0.093
	1.625Mg2.5F2.5	1.55	49.4	0.009	2.85	90.5	0.057
	1.625Mg2.5F7.5	1.51	47.9	0.022	2.87	91.3	0.027

The relative densities of sintered samples measured by Archimedes method are given in Table 3.2. The dried samples with irregular shapes were directly air sintered at 1100ºC for 1 hr. Because the shrinkage in these samples were much more than the previous ones, higher densities were achieved and these samples were used for the micro hardness measurements. High densities were achieved after the sintering at 1100ºC except for the samples 1.17Mg2.5F2.5 and 1.542Mg7.5F2.5, which had the relative densities of 80.2 % and 80.9 %, respectively. Sample 1.625Mg2.5F2.5 exhibited the highest density among the doped samples.

Table 3.2 Densities of the sample pieces after sintering.

Group No	Sample ID	Bulk density (g/cm^3)	Theoretical density (g/cm^3)	% Density	Standard Deviation ($\pm g/cm^3$)
1	2Mg0F0	2.96	3.16	93.9	0.029
	1.67Mg0F0	3.00	3.16	95.0	0.045
	1.5Mg0F0	3.01	3.10	97.1	0.042
	1.2Mg0F0	2.75	3.07	89.6	0.04
2	1.95Mg2.5F2.5	3.00	3.16	95.2	0.039
	1.625Mg2.5F2.5	3.03	3.14	96.4	0.052
	1.463Mg2.5F2.5	2.81	3.09	91.0	0.021
	1.17Mg2.5F2.5	2.47	3.07	80.2	0.032
3	1.65Mg1F2.5	3.02	3.16	95.8	0.037
	1.625Mg2.5F2.5	3.03	3.14	96.4	0.052
	1.542Mg7.5F2.5	2.52	3.11	80.9	0.061
4	1.65Mg1F0	2.91	3.16	92.1	0.064
	1.625Mg2.5F0	2.92	3.14	93.0	0.084
	1.542Mg7.5F0	2.83	3.11	90.7	0.097
5	1.625Mg2.5F0	2.92	3.14	93.0	0.084
	1.625Mg2.5F2.5	3.03	3.14	96.4	0.052
	1.625Mg2.5F7.5	2.91	3.15	92.7	0.023

The improvement in the densification behaviors between the groups 1 and 2 with the additions of Mg^{2+} and F^- ions became more apparent above the Ca/P ratio of 1.67.

Group 3 shows the effect of the increase in Mg amount with a constant 2.5 mole % F^- addition and the group 4 shows the effect of increase in Mg amount on density. In group 3, bulk densities of the samples decreased sharply compared to group 4 when the mole % of Mg^{2+} was increased from 2.5 to 7.5. The decrease in the density by the addition of Mg ions was also reported for Mg substituted HAp

ceramics [129]. Highest densities were achieved for the samples 1.65Mg1F2.5 and 1.65Mg1F0 in groups 3 and 4, respectively (Table 3.1). A similar observation was also reported for 1 wt % MgO addition to HAp/TCP biphasic ceramics (sintered at 1000-1100ºC for 12 hr) and the optimum amount of MgO doping was found to be 1 wt%, which leads to a 99% relative density in HAp/β-TCP ceramics [99]. It was also reported in the same study that the higher concentrations of MgO suppressed the grain growth of HAp/TCP ceramics and lowered the sinterability.

An enhancement in the relative densities was observed for the samples in group 5 in the F^- mole % $\geq$ 2.5 region with a constant 2.5 mole % Mg^{2+} amount. The relative density of sample 1.542Mg7.5F2.5 reduced significantly in comparison to that of sample 1.542Mg7.5F0.

The theoretical densities of HAp and β-TCP are 3.156 and 3.07 g/cm^3, respectively. Therefore, the densities should decrease as the wt% of β-TCP phase increases. In the samples 1.625Mg2.5F2.5 and 1.625Mg2.5F0 (~15 wt% β-TCP), the densities were slightly increased in both F^- doped and undoped samples with constant Mg^{2+} amount, in comparison with samples 1.65Mg1F2.5 and 1.65Mg1F0, which are pure HAp. An enhancement in densification by the incorporation of F^- ions into the sample 1.625Mg2.5F2.5 was observed when compared with that of the sample 1.625Mg2.5F0 with no F^- addition.

3.2 Structural Investigation of the Samples

The XRD patterns of the samples were studied to determine the presence of phases and lattice parameters. In addition to the XRD measurements, FTIR and SEM studies were performed on the samples.

3.2.1 X-ray Diffraction

The XRD spectra of the sintered samples in group 1 are presented in Figure 3.1. The samples 2Mg0F0, 1.67Mg0F0, 1.5Mg0F0, 1.2Mg0F0 with Ca/P ratios of 2.00, 1.67, 1.50, 1.20 were compared with the JCPDS files of HAp and β-TCP.

For the sample 2Mg0F0, CaO phase was detected in addition to HAp because the Ca/P ratio was higher than 1.67 [130,131]. For this sample, an additional peak was observed at the 2θ-angle of 37.44º due to the presence of CaO phase. For sample 1.67Mg0F0, the sintered products were pure HAp. For sample 1.5Mg0F0, a pure HAp/ β-TCP composite was obtained. For the Ca/P ratio of 1.20 (sample 1.2Mg0F0), the product was β-TCP. Narrow and sharp peaks were observed for all of the samples indicating the high crystallinity of these powders. The peaks for HAp and β-TCP were closely matched to their counterparts of the JCPDS files.

It was reported that the structure of bone consists of amorphous phase β-TCP and crystalline phase of HAp in nano crystal sizes [132]. HAp/ β-TCP biphasic composites were generally produced from calcium deficient apatites at temperatures above 800ºC or by introducing Mg^{2+} ions into the HAp structure [91]. In a study of HAp/TCP biphasic ceramics, it was observed that the phase composition was basically a function of the Ca/P ratio of the raw material and the use of porojen did not alter the HA/TCP content, but induced changes in relative content of TCP phase (α or β phase) [133]. It has been reported that even small variations in the Ca/P ratios of the initial precipitates significantly affect the phase composition of the final CaP materials [131]. In Figure 3.1, the increase in the β-TCP phase can be seen. The samples became more calcium deficient from sample 1.67Mg0F0 to 1.2Mg0F0.

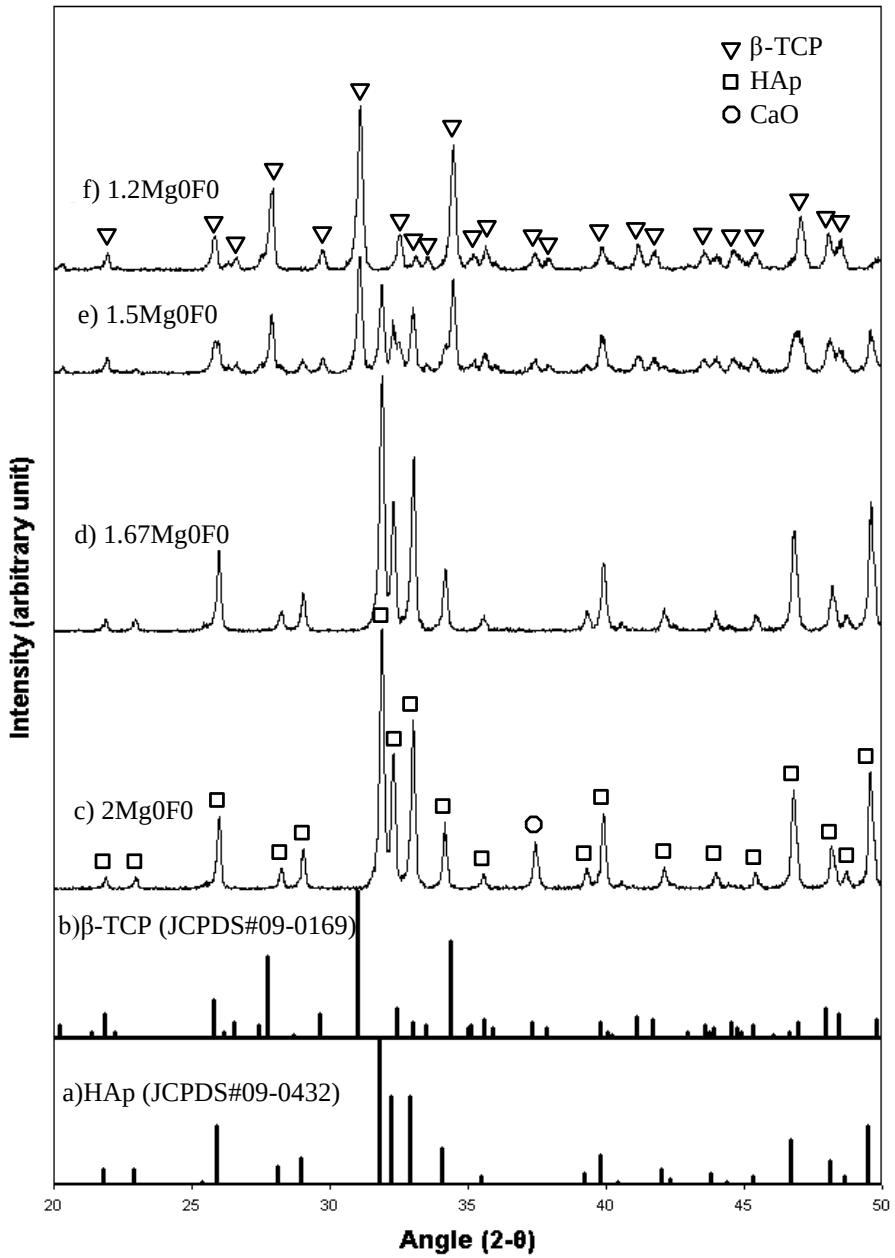

Figure 3.1 XRD results of a) standard HAp (JCPDS# 09-0432); b) standard β-TCP (JCPDS# 09-0169); c) Sample 2Mg0F0; d) Sample 1.67Mg0F0; e) Sample 1.5Mg0F0; f) Sample 1.2Mg0F0. All samples were sintered at 1100ºC for 1 hr.

In Figure 3.2, the XRD patterns of the sintered samples (group 2) are presented. In this group, all the products were doped with 2.5 mole % Mg^{2+} and F^{-}

and sintered at 1100ºC for 1 hr. Although the Ca/P ratios were adjusted as in group 1, the Ca/P ratios were decreased as shown in Table 2.1 as a result of the substitution of Mg^{2+} ions for the Ca^{2+} sites in the samples. The increase in the β-TCP phase can be observed from the XRD patterns for this group. The peaks for HAp and β-TCP were also closely matched with the 2θ angles of JCPDS patterns seen in Figure 3.1. However, as a result of the substitution of Mg^{2+} and F^{-} ions, a slight shift to the left was observed.

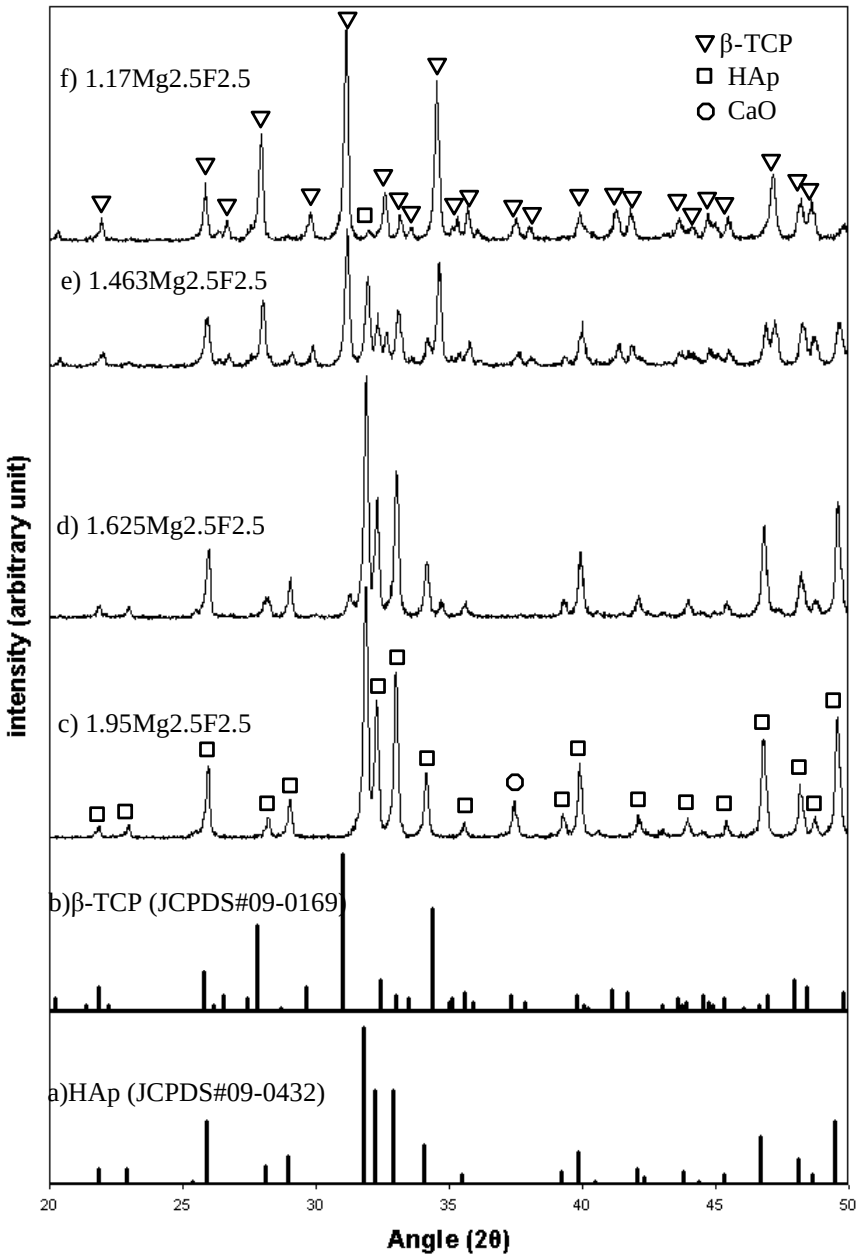

Figure 3.2 XRD results of a) standard HAp (JCPDS# 09-0432); b) standard β-TCP (JCPDS# 09-0169); c) Sample 1.95Mg2.5F2.5; d) Sample 1.625Mg2.5F2.5; e) Sample 1.463Mg2.5F2.5; f) Sample 1.17Mg2.5F2.5. All samples were sintered at 1100ºC for 1 hr.

Although Mg^{2+} ion is known to trigger β-TCP formation even at low sintering temperatures [91,101,102], trace amount of HAp was formed in the sample 1.17Mg2.5F2.5. This could be attributed to the existence of F^- ions, which is known to make the structure of HAp more stable [104]. When compared with the Figure 3.1, the most intense peaks of β-TCP became narrower and higher in Figure 3.2, which indicates better crystallinity in the samples. It was reported that the CaP materials can be combined with Mg^{2+} ions in order to improve crystallization of phosphate deposits and therefore its persistence and biocompatibility [134]. In sample 1.95Mg2.5F2.5, a dominant HAp was present and no β-TCP phase was observed. Moreover, CaO phase was also observed for the sample 1.95Mg2.5F2.5 at the 2θ-angle 37.46º. The presence of CaO phase was also reported for the CaP ceramics with Ca/P ratios higher than 1.67 [130,131]. For the sample 1.625Mg2.5F2.5, the sintered product was HAp with a small amount of β-TCP. As the Ca/P ratio decreased, β-TCP phase became dominant with a small amount of HAp in the sintered product for the sample 1.463Mg2.5F2.5.

Naturally, as the Ca/P ratio decreased, the amount of β-TCP increased as it can be seen from Figure 3.2. For sample 1.95Mg2.5F2.5, an additional peak in 2θ-angle close to the one that was observed for sample 2Mg0F0, was also formed due to the increased Ca^{2+} ion content.

Figure 3.3 presents the XRD patterns for the samples in group 3. No β-TCP formation was observed for the sample 1.65Mg1F2.5 (1 mole % Mg). In a study, HAp/β-TCP biphasic ceramics were produced by the co substitution of Na^+, Mg^{2+} and F^- ions with 3 different HAp/β-TCP ratios by adjusting the amount of initial Ca/P ratios and the amount of the dopants [91]. It was shown that the incorporated elements played a crucial role in the thermal stability of the apatites up to 1400ºC and increased calcium deficiency led to the formation of higher proportion of β-TCP in the biphasic ceramics [91]. As the Mg^{2+} ion content increased, β-TCP formation was also increased in group 3. The increase in the β-TCP content with the increase in the Mg^{2+} ion content was also reported elsewhere [128,135]. From sample 1.625Mg2.5F2.5 to 1.542Mg7.5F2.5, a slight shift to higher 2θ-angles was observed in β-TCP peaks with the increase in the Mg^{2+} ion content.

As a result of Mg^{2+} and F^{-} addition, slight shifts to the right were also observed for the HAp peaks with respect to the pure HAp (sample 1.67Mg0F0). As the Mg^{2+} ion amount was increased to 7.5 mole %, the diffraction peaks of HAp became broader for the sample 1.542Mg7.5F2.5 indicating the poor crystallinity.

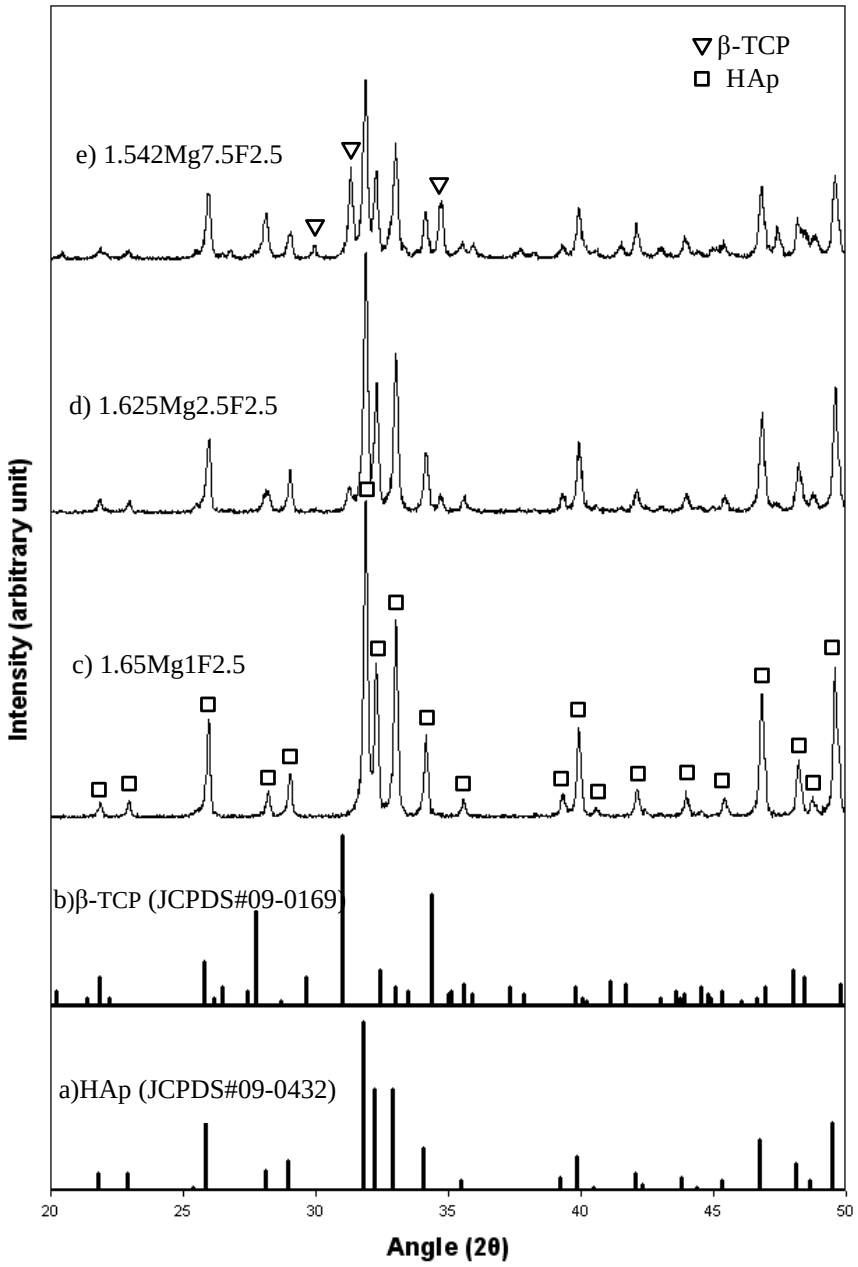

Figure 3.3 XRD results of a) standard HAp (JCPDS# 09-0432); b) standard β-TCP (JCPDS# 09-0169); c) Sample 1.65Mg1F2.5; d) Sample 1.625Mg2.5F2.5; e) Sample 1.542Mg7.5F2.5. All samples were sintered at 1100ºC for 1 hr.

Figure 3.4 presents the XRD patterns of the samples in group 4 with increasing the amounts of (1, 2.5, 7.5 mole %) Mg^{2+} content. No F^- ion was added into the samples for this group. No β-TCP formation was observed for 1 mole % Mg doped sample 1.65Mg1F0. For the samples 1.625Mg2.5F0 and 1.542Mg7.5F0, β-TCP peaks were formed and peaks of β-TCP get higher, respectively. By the increase in the Mg^{2+} content from 2.5 mole % to 7.5 mole %, a slight shift in the 2θ values were also observed in the β-TCP peaks. These peak shifts were also reported for MgO addition into HAp/ β-TCP mixtures by H.-S. Ryu et. al. [99].

As the Mg^{2+} ion amount increased to 7.5 mole % (sample 1.542Mg7.5F0), the diffraction peaks of HAp became broader similar to the sample 1.542Mg7.5F2.5, is seen in Figure 3.3, showing the poor crystallinity nature of this sample. Moreover, as a result of the substitution of Mg^{2+} ions, slight peak shifts were also observed for the HAp peaks with respect to the sintered pure HAp (sample 1.67Mg0F0).

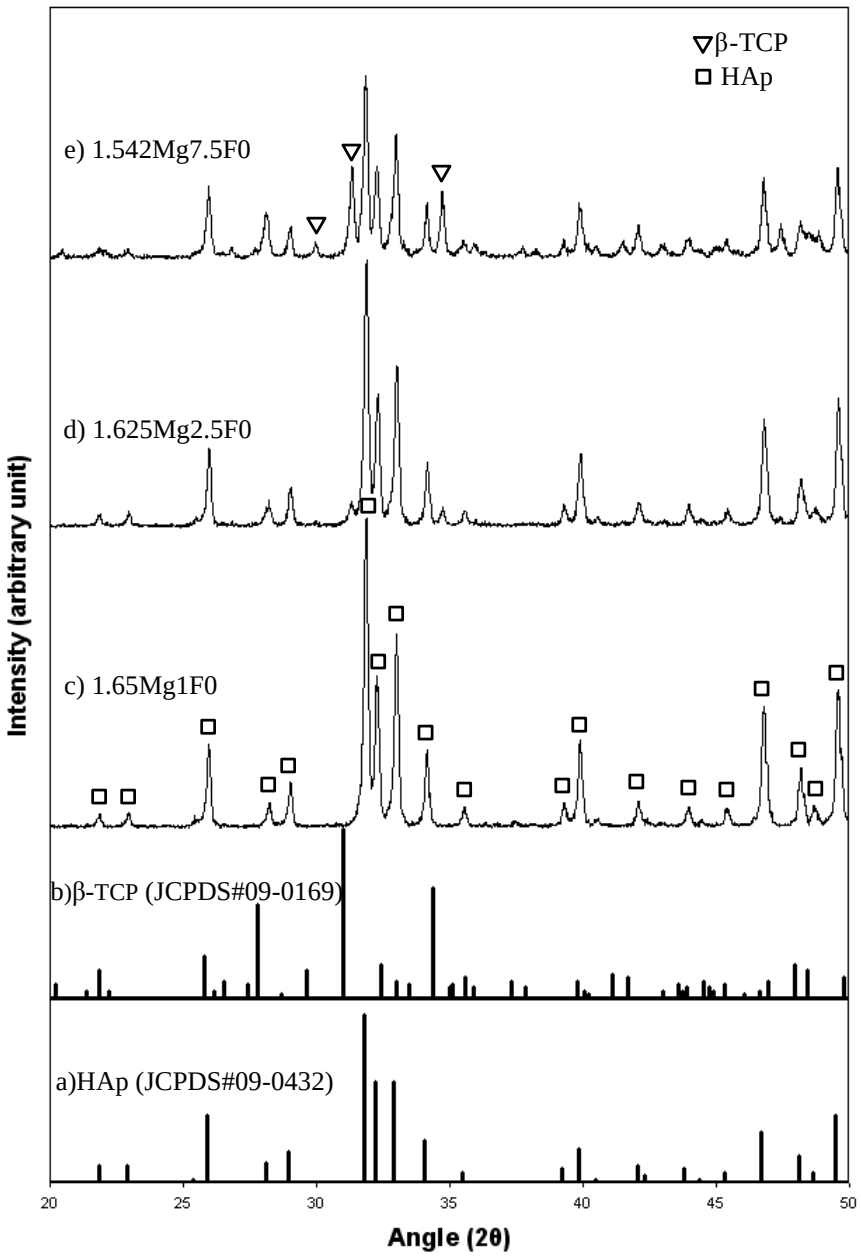

Figure 3.4 XRD results of a) standard HAp (JCPDS# 09-0432); b) standard β-TCP (JCPDS# 09-0169); c) Sample 1.65Mg1F0; d) Sample 1.625Mg2.5F0; e) Sample 1.542Mg7.5F0. All samples were sintered at 1100ºC for 1 hr.

Figure 3.5 shows the XRD results of the group 5 samples with selective effect of increase in the F amount with a constant amount (2.5 mole %) of Mg

dopant. In Figure 3.5, well-crystallized samples were obtained. The intensity of β-TCP peaks was decreased with an increase in F^- amount. As it can be seen from this figure, as the F amount increased from 2.5 to 7.5 mole %, the intensity of the peak at (002) plane was also increased, indicating that the crystals were well crystallized and oriented in the c- axis direction of the apatite. Moreover, the crystallinity was increased with the increase in the F^- content [136,137].

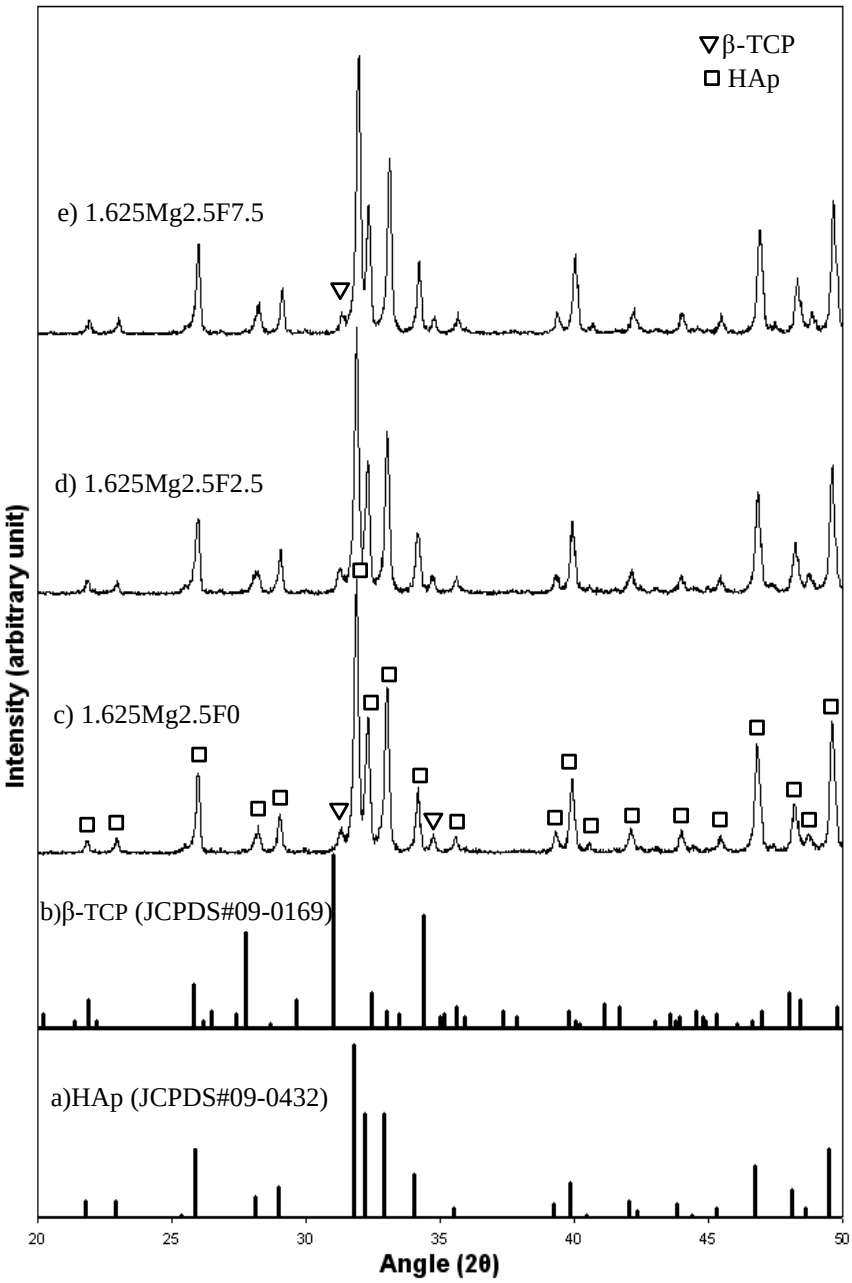

Figure 3.5 XRD results of a) standard HAp (JCPDS# 09-0432); b) standard β-TCP (JCPDS# 09-0169); c) Sample 1.625Mg2.5F0; d) Sample 1.625Mg2.5F2.5; e) Sample 1.625Mg2.5F7.5. All samples were sintered at 1100ºC for 1 hr.

In order to control the phase content during the sintering for the samples in group 1, the phase transition temperature (1125˚C) from β to α-TCP [107] was taken

as the threshold value and the highest optimum sintering temperature was taken as 1100˚C [138]. Additionally, the optimum sintering time was chosen 1 hr [139].

Amounts of HAp and β-TCP phases present in the samples are presented in Table 3.3. The phases were determined from the relative intensity measurements of the XRD patterns according to the Equations 2.4 and 2.5. Amount of β-TCP formation was increased with the increase in Mg^{2+} content and decreased with the increase in the F^- ion content in group 5, making the structure of HAp more stable. It was reported that F tends to decrease the strain on the apatite lattice and thereby increase the stability of the apatite structure [140]. In a study that compares the fluoridated HAp with pure HAp, more β-TCP phase was detected in HAp than in fluoridated HAp at both 1300ºC and 1400ºC, which confirmed that the thermal stability of fluoridated HAp increased with an increase in F^- ion content in the specimens [141]. It was also reported that as a result of the F^- ion substitution into HAp lattice, peak shifts to higher 2θ values were observed in the positions of (211), (300) and (112) peaks in an increasing manner with the increase in the F^- ion content [142,143]. Peak shifts in these positions due to the F^- ion substitution were also reported in another study [141]. However, the XRD patterns obtained from the fluoridated HAp samples with different F^- ion contents revealed the same systematic shift for these peaks (independent from the F^- ion amounts) in contrast to the previous reports by Okazaki et al [142,143]. Therefore, the form of the shifted peaks was interpreted as the convolution of the peaks from HAp and FAp [141].

In the XRD patterns of group 5, from sample 1.625Mg2.5F2.5 (2.5 mole % F^-) to 1.625Mg2.5F7.5 (7.5 mole % F^-), the positions of (211), (300) and (112) peaks were shifted significantly to higher 2θ values. However, for the smallest amount of F^- addition (2.5 mole %), a significant shift could not be detected, suggesting that the findings of Okazaki et al. [142,143] might be more accurate compared to the study [141] mentioned above.

Although Mg^{2+} ion is known to trigger β-TCP formation, no β-TCP phase was observed for 1 mole % Mg^{2+} ion in the sample 1.95Mg2.5F2.5 (Figure 3.2) and in the samples 1.65Mg1F2.5 and 1.65Mg1F0 (Figures 3.3 and 3.4). As indicated in Table 3.3, no β-TCP formation was observed for samples 2Mg0F0 and

1.95Mg2.5F2.5. Some amount of CaO was present together with HAp for these samples because of their Ca/P ratios exceeding the stochiometric ratio. However, since the main aim of this study was to compare the β-TCP and HAp amounts and to investigate their resulting structural and mechanical affects, CaO amounts were not taken into account in Table 3.3.

Table 3.3 Presence of HAp and β-TCP phases in the samples.

Groups	Sample ID	$W_{\beta\text{-TCP}}$%	W_{HAp}%	Phase Formations
1	2Mg0F0	—	100.0	No TCP
	1.67Mg0F0	—	100.0	No TCP
	1.5Mg0F0	69.8	30.2	TCP
	1.2Mg0F0	100.0	—	TCP
2	1.95Mg2.5F2.5	—	100.0	No TCP
	1.625Mg2.5F2.5	14.8	85.2	TCP
	1.463Mg2.5F2.5	72.6	27.4	TCP
	1.17Mg2.5F2.5	97.5	2.5	TCP
3	1.65Mg1F2.5	—	100.0	No TCP
	1.625Mg2.5F2.5	14.8	85.2	TCP
	1.542Mg7.5F2.5	47.5	52.5	TCP
4	1.65Mg1F0	—	100.0	No TCP
	1.625Mg2.5F0	14.9	85.0	TCP
	1.542Mg7.5F0	46.9	53.1	TCP
5	1.625Mg2.5F0	14.9	85.0	TCP
	1.625Mg2.5F2.5	14.8	85.2	TCP
	1.625Mg2.5F7.5	12.5	87.5	TCP

3.2.1.1 Lattice Parameter Measurements

Hexagonal lattice parameters and unit cell volumes of all the samples are presented in Table 3.4. As seen from this table, hexagonal lattice parameters ‘a’ and ‘c’ were decreased for all sintered materials in comparison with the lattice parameters of the pure HAp (JCPDS file #09-0432). As a result, unit cell volumes of the apatites were decreased.

Table 3.4 HAp and β-TCP lattice parameters of the samples.

Group No	Sample IDs	HAp Lattice Parameters				Sample IDs	β-TCP Lattice Parameters			
		a (Å)	c (Å)	V (Å^3)	ΔV (Å^3)		a (Å)	c (Å)	V (Å^3)	ΔV (Å^3)
	HAp (09-0432)	9.4180	6.8840	1580.9	0.0	β-TCP (09-0169)	10.4290	37.3800	3520.8	0.0
1	2Mg0F0	9.4132	6.8739	1576.9	-3.9	2Mg0F0	—	—	—	—
	1.67Mg0F0	9.4106	6.8720	1575.6	-5.3	1.67Mg0F0	—	—	—	—
	1.5Mg0F0	9.4118	6.8765	1577.0	-3.8	1.5Mg0F0	10.4289	37.5213	3534.1	13.2
	1.2Mg0F0	—	—	—	—	1.2Mg0F0	10.3938	37.3992	3498.9	-22.0
2	1.95Mg2.5F2.5	9.4090	6.8785	1576.6	-4.3	1.95Mg2.5F2.5	—	—	—	—
	1.625Mg2.5F2.5	9.4080	6.8758	1575.6	-5.3	1.625Mg2.5F2.5	10.3765	37.4024	3487.5	-33.3
	1.463Mg2.5F2.5	9.3615	6.8753	1560.0	-20.9	1.463Mg2.5F2.5	10.3543	37.2940	3462.6	-58.3
	1.17Mg2.5F2.5	—	—	—	—	1.17Mg2.5F2.5	10.3798	37.2834	3478.7	-42.1
3	1.65Mg1F2.5	9.4100	6.8785	1576.9	-4.0	1.65Mg1F2.5	—	—	—	—
	1.625Mg2.5F2.5	9.4080	6.8758	1575.6	-5.3	1.625Mg2.5F2.5	10.3765	37.4024	3487.5	-33.3
	1.542Mg7.5F2.5	9.4100	6.8962	1580.9	0.1	1.542Mg7.5F2.5	10.3708	37.3296	3476.9	-43.9
4	1.65Mg1F0	9.4147	6.8787	1578.5	-2.3	1.65Mg1F0	—	—	—	—
	1.625Mg2.5F0	9.4147	6.8754	1577.8	-3.1	1.625Mg2.5F0	10.3711	37.7841	3519.5	-1.3
	1.542Mg7.5F0	9.4210	6.8766	1580.2	-0.7	1.542Mg7.5F0	10.3447	37.1974	3447.2	-73.6
5	1.625Mg2.5F0	9.4147	6.8754	1577.8	-3.1	1.625Mg2.5F0	10.3711	37.7841	3519.5	-1.3
	1.625Mg2.5F2.5	9.4080	6.8758	1575.6	-5.3	1.625Mg2.5F2.5	10.3765	37.4024	3487.5	-33.3
	1.625Mg2.5F7.5	9.3857	6.9464	1584.3	3.4	1.625Mg2.5F7.5	10.3470	37.5044	3477.2	-43.6

The variations in the lattice parameter values “a” and “c” were not found to be in correlation with the decrease in the Ca/P ratios for HAp, in group 1 and the changes in the unit cell volumes were mainly due to the sintering, as there were no dopants in this group. Small irregular changes have been observed in “a” and “c” lattice parameters. On the other hand, both “a” and “c” lattice parameters of HAp were decreased gradually with the decrease in the Ca/P ratio as a result of the substitution of constant amount of Mg^{2+} and F^- ion addition (2.5 mole %) in group 2. In a study with fluoridated HAp and Mg containing fluoridated HAps by Okazaki et al., it was reported that “a” lattice parameter was decreased with the increase in degree of fluoridation, which suggested the substitution of F^- ions into the apatite crystals [144,145]. Additionally, for the Mg^{2+} ion containing fluoridated HAps, the “c” lattice parameter was also decreased as a result of the substitution of Mg^{2+} ions into the apatite crystals [145]. Therefore, this decrease in the lattice parameters of HAp should be attributed to the substitution of these ions within the samples in group 2.

Because ion sizes of both Mg^{2+} and F^- are smaller than those of Ca^{2+} and OH^- ions, it is expectable that the addition of these ions resulted in the shrinkage of unit cell volumes (Table 3.4). The effective ionic radii of Mg^{2+} and Ca^{2+} ions are 0.72 Å and 1.0 Å and F^- and OH^- ions have an effective ionic radii of 1.33 Å and 1.37 Å, respectively [85]. In group 4, “a” lattice parameters were slightly increased by the addition of 1 mole % Mg^{2+} ion (sample 1.65Mg1F0) in comparison with the pure HAp sintered at 1100ºC (sample 1.67Mg0F0). Increasing the Mg^{2+} ion amount to 2.5 mole % did not change the “a” values, while for the 7.5 mole % Mg^{2+} ion, the “a” lattice parameter was increased in group 4. This change in the “a” lattice parameters may be due to the stresses introduced to the unit cell by the addition of Mg^{2+} ions. The “c” lattice parameter was decreased from sample 1.65Mg1F0 to sample 1.625Mg2.5F0 as the Mg content increased. However, further increase in the Mg amount did not show the same effect on the “c” lattice parameter.

It has been reported that Mg substitution into the apatite crystals may occur to a limited extend whereas it was also suggested that the substitution of Mg^{2+} ions could be promoted by fluoride [145]. Therefore, it can be concluded that in the case

of group 4, 2.5 mole % Mg could be substituted into the apatite structure as the limit value in the absence of F^- ions. It has been reported that F ions increase the crystal sizes of HAp along the c-axis direction [10]. In summary, Mg ions have a decreasing effect on the "c" lattice parameters, while F^- ions have an increasing effect. When the "c" lattice parameters of groups 3 and 4 were compared, it can be seen that the effect of the F ions on the "c" values were dominant. The "c" lattice parameter of sample 1.542Mg7.5F2.5 was significantly higher than that of sample 1.542Mg7.5F0 for 7.5 mole% Mg.

In group 3, addition of F^- ions suppressed the increase in the "a" lattice parameters with respect to group 4 for the same variations of Mg^{2+} ions. Incorporation of F^- ions into the apatite structure causes a contraction of the "a" lattice [144,145]. Therefore, it can be concluded that in group 3, an increase in the "a" value was not observed in sample 1.65Mg1F2.5 with 1 mole % Mg addition with respect to sample 1.65Mg1F0 in group 4.

In group 5; sample 1.625Mg2.5F7.5, highest c/a ratio was obtained due to the gradual decrease in the "a" lattice parameters for both HAp and β-TCP and increase in the "c" lattice parameter of HAp for the highest F^- amount. As a result of the substitution of F^- ions, with the addition of 7.5 mole% F^- ion, an apparent increase in the "c" lattice parameter values were observed in both HAp and β-TCP phases for sample 1.625Mg2.5F7.5. Since all of the samples in group 5 were doped with constant amount of Mg^{2+} ions (2.5 mole%) besides F^- ions, it is logical to attribute this increase to the high amount of F^- ion substitution. It was also reported that for 20%, 60% and 100% F^- ion substitution for OH^- groups, the crystallinity of the fluoridated HAps were increased gradually with the increase in the F^- amount. This indicated that the F^- concentration increased the driving force for the apatite crystal growth during precipitation [137].

Additionally, the slight shift to higher 2θ values that was observed from sample 1.625Mg2.5F2.5 to 1.542Mg7.5F2.5 in the XRD patterns of group 3 (Figure 3.3) indicated that the lattice parameters of β-TCP decreased by the increase in the Mg^{2+} content. This can also be verified from Table 3.4. A slight shift to higher 2θ values was also observed from sample 1.625Mg2.5F0 to 1.542Mg7.5F0 similar to

group 3 samples in Figure 3.4. This shift also indicated the decrease in the β-TCP lattice parameters (Table 3.4) as it was reported for the previous group. A similar observation was also reported by H.-S. Ryu et. al. [99] for the MgO addition into HAp/ β-TCP mixtures. The decrease in the lattice parameters of β-TCP occurs as a result of the lattice contraction due to the replacement of Ca^{2+} atoms with Mg^{2+} ions with smaller radii.

Mg^{2+} ions improve the densification behavior of β-TCP by shifting its phase transition temperature (~1125ºC) to higher values and prevent its transition to α-TCP, which leads to an expansion in the unit cell volume. The variation in the unit cell volumes (ΔV) of β-TCP in sample 1.542Mg7.5F0 with no F^- dopant, was significantly high for 7.5 mole % Mg^{2+}. However, a high ΔV value was also obtained for sample 1.625Mg2.5F7.5 with 2.5 mole % Mg^{2+} and 7.5 mole % F^- dopants, which indicated that the change in the unit cell volumes were mainly due to the difference in the atomic radii of the dopants.

It was reported that the amount of Mg^{2+} ions associated on the surface of HAp is usually much more than the Mg^{2+} ions incorporated into its crystalline structure [10]. However, as a result of the change in the lattice parameters (Table 3.4) of the Mg^{2+} and/or F^- doped HAps, it can be concluded that Mg^{2+} ions are actually incorporated into the unit cell structure and not just adsorbed on the HAp crystalline surface. The variations in the lattice parameters and unit cell volumes of the doped samples with respect to their undoped counterparts can be interpreted as the incorporation of these ions into the unit cell structure of the samples.

In group 5, the F^- amount was increased from 0 to 7.5 mole %, while Ca/P ratio and the Mg amounts were kept the same. “c” values of the samples were increased significantly and the “a” values were decreased in the HAp phase.

3.2.2 Fourier Transform Infrared Spectroscopy

FTIR was employed to identify the functional groups of the sintered doped and undoped CaPs. The characteristic band exhibited by the samples and their corresponding infrared frequencies are given in Table 3.5. All of the samples

showed the characteristic bands for HAp and β-TCP as well as the bands that appeared due to the substitution of the dopants. For all of the samples sintered at 1100°C, the spectra region for the presence of adsorbed water around 3300-3600 cm^{-1} [91] was almost a flat line, indicating the minimum amount of adsorbed water in the samples. The band at 962.59 cm^{-1} is assigned to υ_1, the non-degenerate P-O symmetric stretching mode. The bands at 1048.4 and 1090.8 cm^{-1} are assigned to the components of the triply degenerated υ_3 antisymmetric P-O stretching mode and the bands at 573.89 and 599.93 were assigned to the components of the triply degenerate υ_4 O-P-O bending mode [131]. The bands that are attributed to the υ_2 O-P-O bending mode was out of range for the investigated frequency interval.

Table 3.5 Infrared frequencies and their assignments for the sintered CaP samples.

Assignment	**Infrared Frequency (cm^{-1})**	**Reference #**
OH^- (stretching)	3571.6	[136]
adsorbed water	~3300-3600	[91]
υ_3 PO_4^{-3} (P-O antisymmetric) stretching	1048.4 and 1090.8	[135]
υ_1 PO_4^{-3} (P-O symmetric) stretching	962.59	[135]
OH-F bond	~ 720 and 3544.6	[91,132]
OH^- (librational)	631.7	[136]
υ_4 PO_4^{-3} (P-O-P symmetric) bending	573.89 and 599.93	[135]

The spectra for the samples categorized in five groups are presented in Figures 3.6-3.10. In Figure 3.6, the undoped CaP samples of group 1 were investigated for the Ca/P ratios ranging from 2.00 to 1.20. In the spectras for pure

HAp (sample 2Mg0F0, 1.67Mg0F0) and HAp/ β-TCP composite (sample 1.5Mg0F0), the bands for PO_4 groups and OH^- groups were easily observable, while for pure β-TCP (sample 1.2Mg0F0) the OH^- stretching and librational modes of HAp were disappeared.

The characteristic OH^- absorption bands at 631.7 and 3571.6 cm^{-1} of HAp [133] were present for the spectra of samples 2Mg0F0-1.5Mg0F0 and naturally disappeared for sample 1.2Mg0F0, which was in good agreement with the findings of Slosarczyk et al. [131]. Therefore, the transmittance intensities of the OH^- groups for HAp were gradually decreased from sample 1.67Mg0F0 to 1.2Mg0F0 as the HAp content decreased. Additionally, the OH^- intensities were also decreased for sample 1, due to the decrease in the HAp wt % as a result of the presence of CaO phase (Figure 3.1). It was reported that because of its reactivity against water, the presence of CaO could be very harmful for implantation materials and when stored in air, the sintered material can absorb water vapor with the formation of some amount $Ca(OH)_2$ [131]. Since the spectra region assigned for the absorbed water at 3300-3600 cm^{-1} was almost a flat line in all of the samples, it can be concluded that a transformation from CaO phase to $Ca(OH)_2$ did not occurred for the samples 2Mg0F0 and 1.95Mg2.5F2.5.

Therefore, the decrease in the intensities of OH^- bands in HAp can not be attributed to the excess amount of Ca ions in sample 2Mg0F0, forming bonds with the OH ions, but they could be rather as a result of the decrease in HAp by weight. This behavior suggests that the transmission intensities give us also quantitative information about the HAp and β-TCP amounts. A similar case with 2 % CaO and 98 % HAp (by weight) was reported by Slosarczyk et al. [131]. In that study, CaO existence was verified due to the surface hydroxyl ions at around 3642 cm^{-1} that were not originated from HAp, suggesting a transformation of CaO to $Ca(OH)_2$. The absorbance band at ~3642 cm^{-1} has been assigned to the surface hydroxyl ions [26]. However, this band was not observed for sample 2Mg0F0, verifying that the CaO phase did not transformed to $Ca(OH)_2$. Additionally, some irregular fluctuations were observed in the FTIR spectra of the samples. These fluctuations may be due to the impurities present in the samples. Additionally, as the β-TCP content increased,

broadening accompanied with the reduction in the intensities was observed in the bands assigned for the PO_4^{3-} groups. As the β-TCP phase occurred in sample 1.5Mg0F0 and totally in sample 1.2Mg0F0, additional peaks were detected at around the infrared frequencies 1126 cm^{-1} and 971 cm^{-1}, which can be attributed to the β-TCP phase [133].

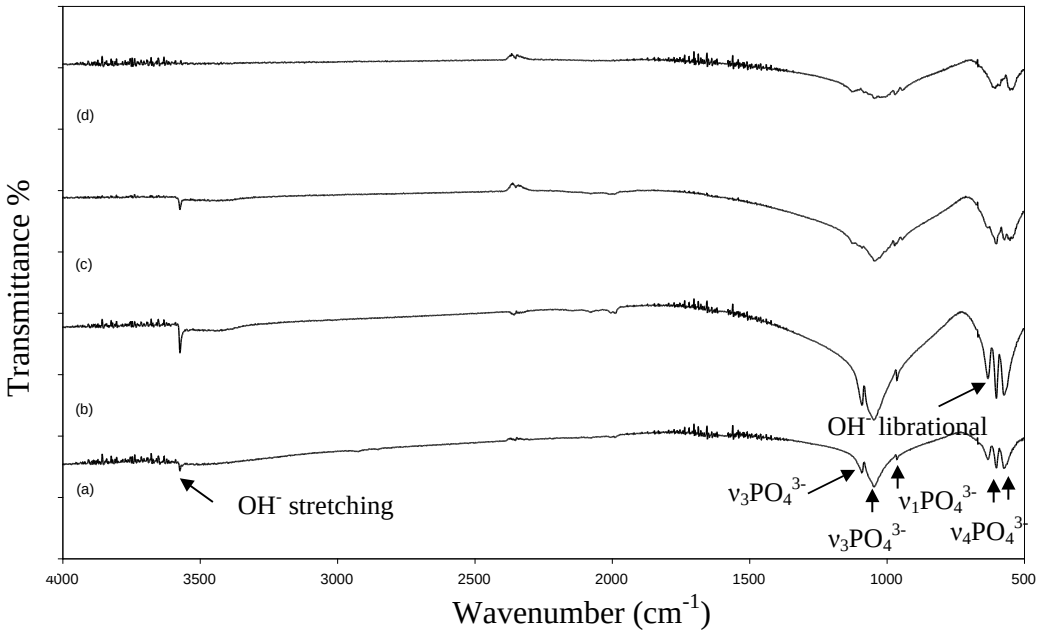

Figure 3.6 FTIR patterns of the sintered CaP samples of group 1: a) Sample 2Mg0F0; b) Sample 1.67Mg0F0; c) Sample 1.5Mg0F0; d) Sample 1.2Mg0F0.

The FTIR spectra for the samples in group 2 are presented in Figure 3.7. All of the samples were doped with 2.5 mole % Mg^{2+} and F^- ions with Ca/P ratios ranging from 1.95 to 1.17 as seen in Table 2.1. The bands assigned for the PO_4 groups and OH^- vibrational modes were also visible for this group. As it is seen in Figure 3.7 (a-d), the broadening of the PO_4 groups were also gradually increased from sample 1.95Mg2.5F2.5 to 1.17Mg2.5F2.5 with the increase in β-TCP content (Table 3.3) similar to the samples in group 1. In samples 1.95Mg2.5F2.5 and

1.625Mg2.5F2.5 the dominant phase was HAp, while for samples 1.463Mg2.5F2.5 and 1.17Mg2.5F2.5 β-TCP phase was dominant. As a result, the characteristic bands of OH^- groups for HAp were disappeared for samples 1.463Mg2.5F2.5 and 1.17Mg2.5F2.5. In samples 1.95Mg2.5F2.5 and 1.625Mg2.5F2.5 additional peaks other than HAp were identified at frequencies 3544.6 cm^{-1} [137] and ~720 cm^{-1} [91], which were assigned for the incorporated F^- ions replacing with the OH^- groups of HAp. It should also be noted that as a result of the partial replacement of the F^- ions with the OH^- groups, the peaks corresponding to OH^- were not as intense as the ones detected for the pure HAp (sample 1.67Mg0F0) with no additional phases. For the samples 1.95Mg2.5F2.5 and 1.625Mg2.5F2.5, the librational OH^- peak at 631.7 cm^{-1} for HAp was considerably shifted from its normal position to ~640 cm^{-1} due to the incorporation of F^- ions into the apatite unit structure. In a FTIR study for HAp/β-TCP composites co-substituted with Na^{2+}, Mg^{2+} and F^- ions, approximately the same amount of peak shift was also reported as a result of the F^- incorporation [91].

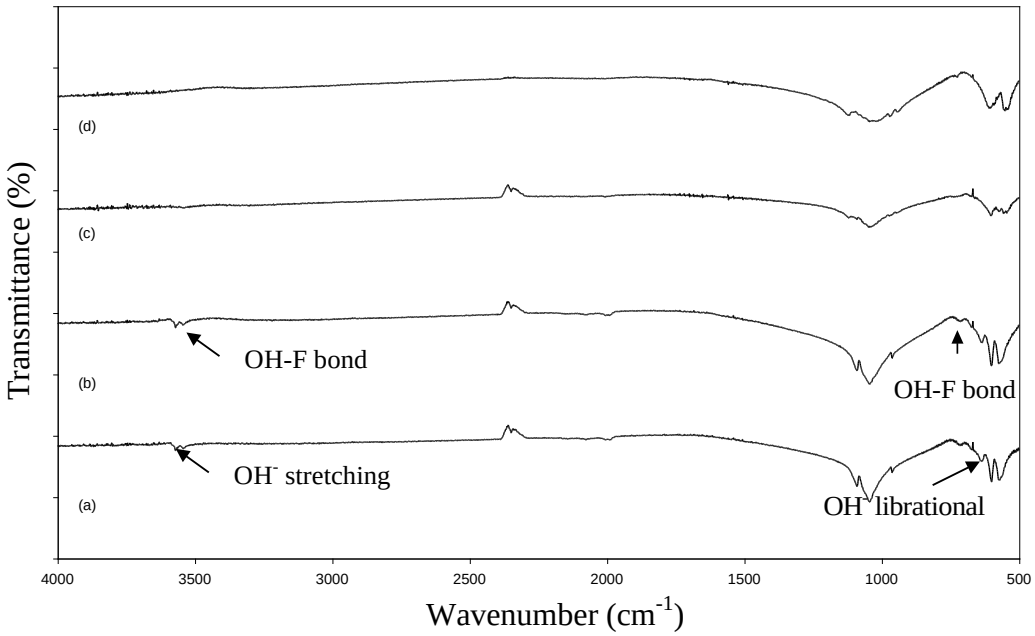

Figure 3.7 FTIR patterns of the sintered CaP samples of group 2: a) Sample 1.95Mg2.5F2.5; b) Sample 1.625Mg2.5F2.5; c) Sample 1.463Mg2.5F2.5; d) Sample 1.17Mg2.5F2.5.

It was reported that the presence of the CaO phase could be identified with FTIR by determining the existence of the surface hydroxyl ions due to the transformation of the CaO phase to $Ca(OH)_2$ [131]. The FTIR band at ~3642 cm^{-1} has been assigned to the surface hydroxyl ions [26,130]. This peak could not be detected also as in the case of sample 2Mg0F0. This might be also due to the presence of F^- ions forming a new peak at 3544.6 cm^{-1} assigned to the F-OH bonding, interrupting a possible transformation from CaO to $Ca(OH)_2$. It should also be noted that the OH^- source for F-OH bond assignment was mainly at the OH stretching and librational modes of HAp, which was easily observed for the samples in group 5.

In Figure 3.8, the FTIR patterns of the samples in group 3 are presented. The Ca/P ratios ranged from 1.65 to 1.542 as a result of the increase in the amount of Mg^{2+} ions replacing the Ca^{2+} ions. In all the samples, F^- amount was constant at 2.5

mole %, while Mg content was 1, 2.5 and 7.5 mole % for the samples 1.65Mg1F2.5, 1.625Mg2.5F2.5 and 1.542Mg7.5F2.5, respectively. The characteristic vibration modes for the PO_4^{3-} groups and OH^- groups that were aroused from HAp and F-OH bonding were also visible for this group. Due to the incorporation of F^- ions, the same amount of peak shift was also observed at the OH^- librational mode for this group as in the previous one.

For the first two groups, broadening and a decrease in the intensities were observed for the PO_4^{3-} groups with the increase in the β-TCP and therefore decrease in the HAp content (by weight). Although a decrease in the HAp content was also observed for group 3, the intensities of the PO_4^{3-} groups were increased significantly as the Mg^{2+} ion amount increased from 1 mole % to 7.5 mole %. As a result of the Mg^{2+} ion addition, a slight shift of the 3571.6 cm^{-1} absorbing bands was observed. Broadening of the phosphate bands and the slight shift of the 3571.6 cm^{-1} bands was also reported for increasing amounts of Mg^{2+} ion substitution into HAp ceramics [128,129].

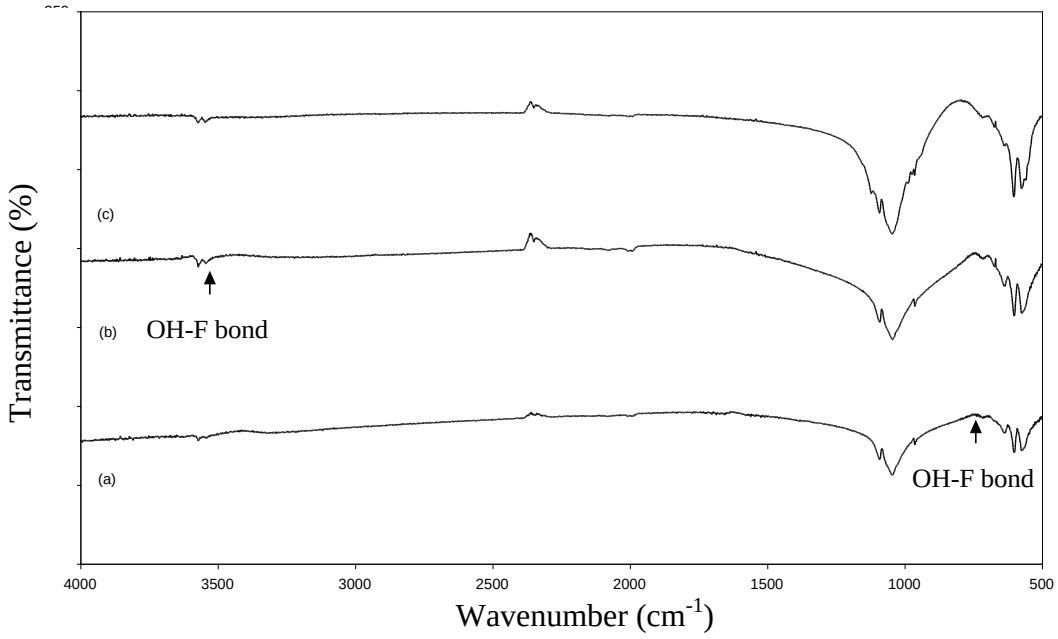

Figure 3.8 FTIR patterns of the sintered CaP samples of group 3: a) Sample 1.65Mg1F2.5; b) Sample 1.625Mg2.5F2.5; c) Sample 1.542Mg7.5F2.5.

The FTIR patterns of the samples in group 4 are presented in Figure 3.9. In this group, Ca/P ratios were also ranged from 1.65 to 1.542 as a result of the increase in the amount of Mg^{2+} ions replacing the Ca^{2+} ions. Mg^{2+} content was 1, 2.5 and 7.5 mole % for the samples 1.65Mg1F0, 1.625Mg2.5F0 and 1.542Mg7.5F0 as in the previous group. However, no F^- was present within the samples of this group. As a result, the peaks due to F-OH^- bonding were not observed in these spectra. The infrared frequencies assigned for PO_4^{3-} groups and OH^- librational, stretching modes were almost at the same wave numbers in comparison with group 1. Especially for sample 1.542Mg7.5F0, an increase was also observed in the intensities of the PO_4^{3-} groups similar to group 3 due to the increased Mg^{2+} ion content. However, with the existence of 2.5 mole % F^-, this increase was quantitatively more accurate for group 3. Similar to groups 1 and 2, the intensities of the OH^- groups of HAp were also decreased with the decrease in the HAp content.

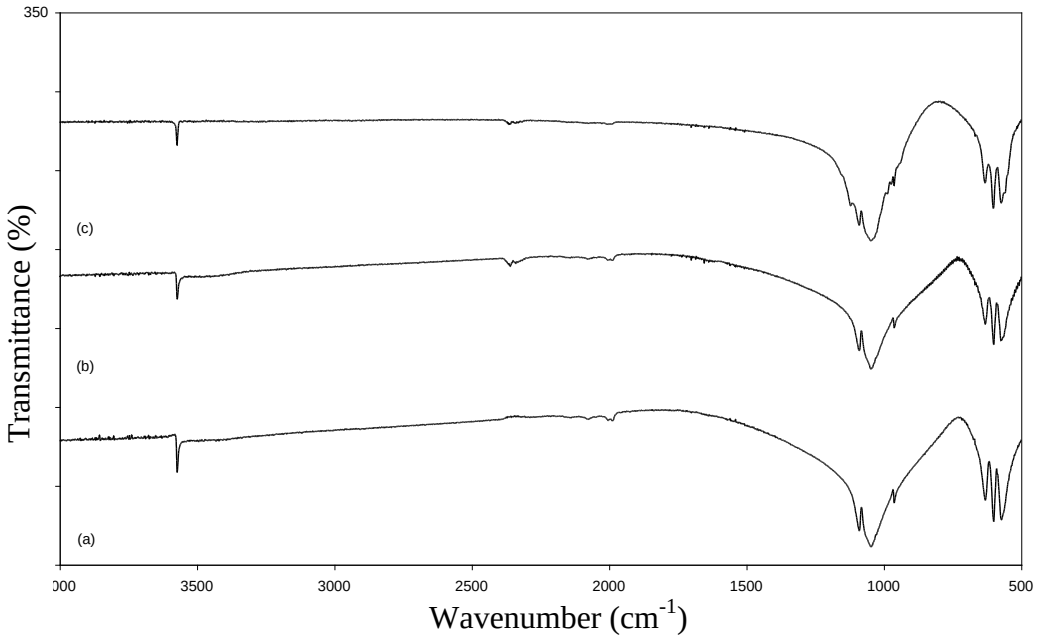

Figure 3.9 FTIR patterns of the sintered CaP samples of group 4: a) Sample 1.65Mg1F0; b) Sample 1.625Mg2.5F0; c) Sample 1.542Mg7.5F0.

Finally, the FTIR patterns of group 5 are presented in Figure 3.10. The effect of increase in the F content from 0 to 7.5 mole % was investigated for the CaP samples with a constant 1.625 Ca/P ratio and 2.5 mole % Mg^{2+}. Apart from the vibrational modes of PO_4^{3-} groups and OH^- groups of HAp, the infrared frequencies assigned to the OH-F bonding were also observed in an increasing manner with the increase in the F^- content. Intensities of the librational and stretching modes of OH^- were gradually decreased forming a shoulder for the sample 1.625Mg2.5F7.5, while the intensities at around 720 cm^{-1} and 3544.6 cm^{-1} were gradually increased as a result of the F^- ions replacing OH^- ions. The presence of the peaks assigned for the OH^- librational and stretching modes confirms that the F ions only partially replaced the OH^- ions, resulting in the formation of flouridated HAp. The peak shifts that were detected due to the incorporation of F^- ions in groups 2 and 3 were also

observed for group 5. Amount of the peak shift was found to be increased (~ 670 cm^{-1}) with 7.5 mole % F^- content for sample 1.625Mg2.5F7.5.

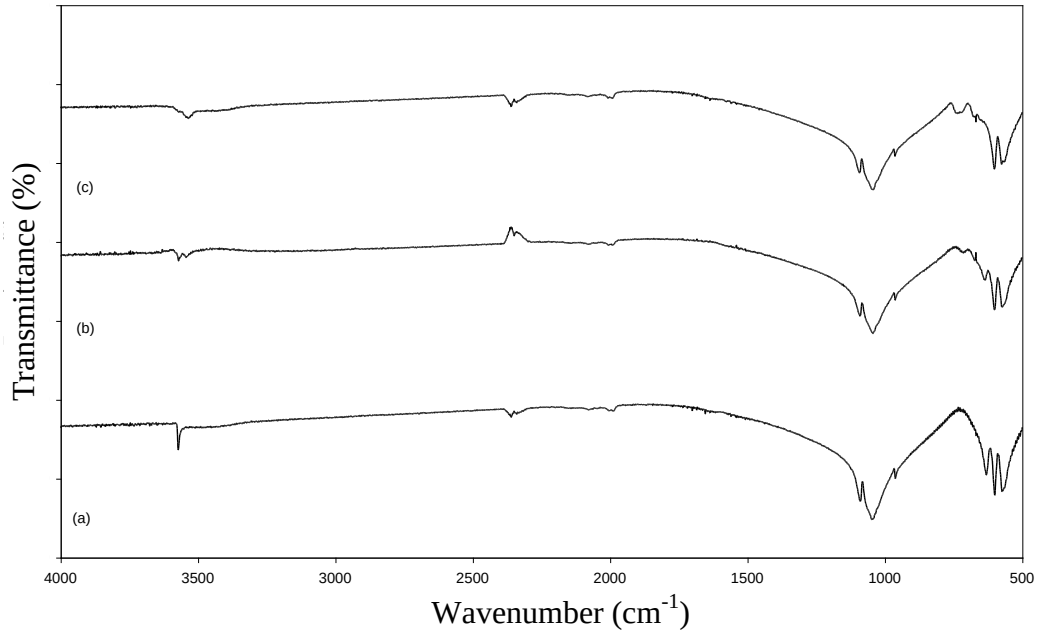

Figure 3.10 FTIR patterns of the sintered CaP samples of group 5: a) Sample 1.625Mg2.5F0; b) Sample 1.625Mg2.5F2.5; c) Sample 1.625Mg2.5F7.5.

3.2.3 Scanning Electron Microscopy

SEM images of the pure and doped CaPs are given in Figures 3.11- 3.24. All of the images were taken from the samples that were sintered at 1100 ºC for 1 hr. The average grain sizes of the samples according to their groups are presented in Table 3.7.

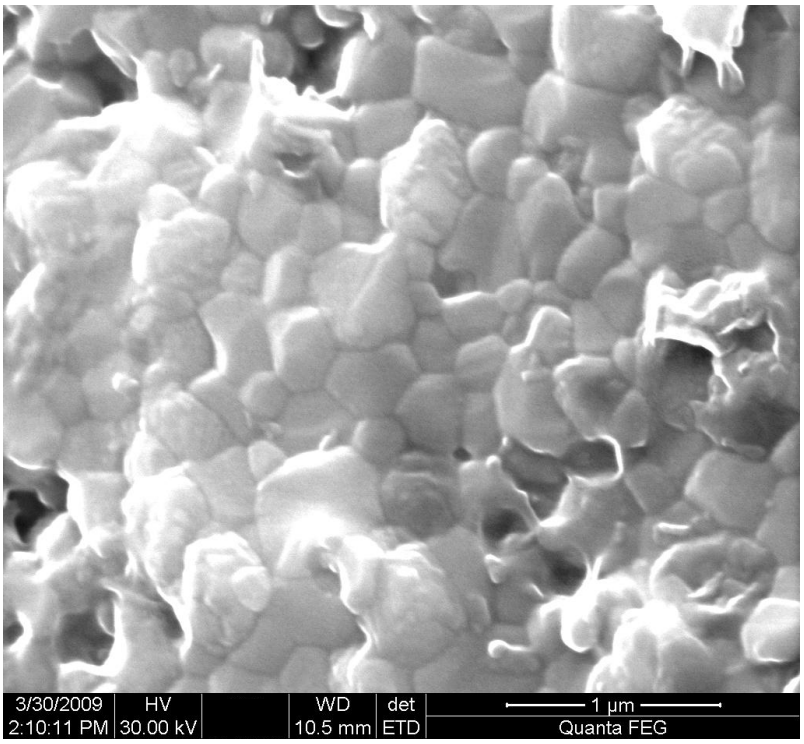

Figure 3.11 SEM image of the sample 2Mg0F0.

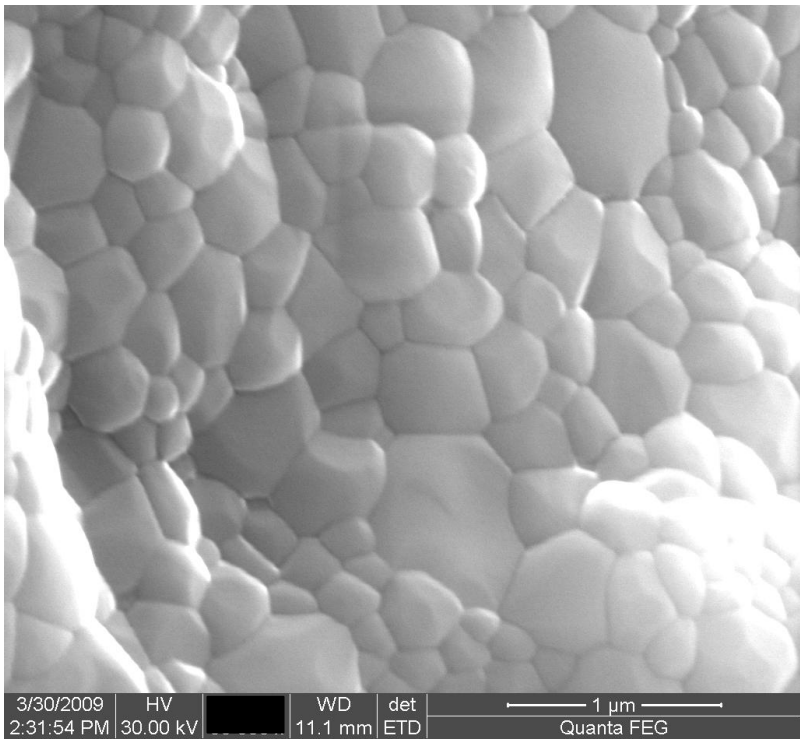

Figure 3.12 SEM image of the sample 1.67Mg0F0.

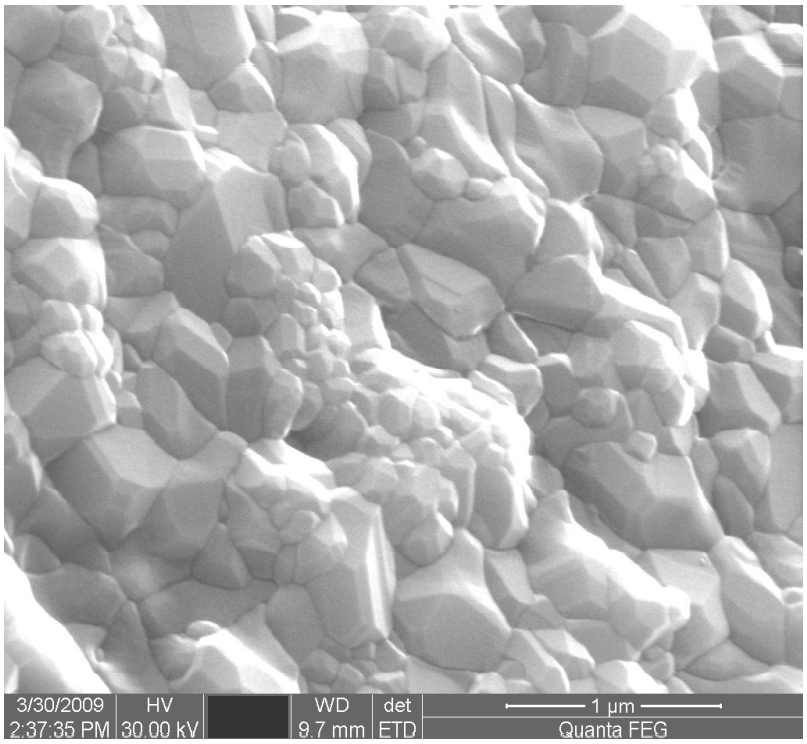

Figure 3.13 SEM image of the sample 1.5Mg0F0.

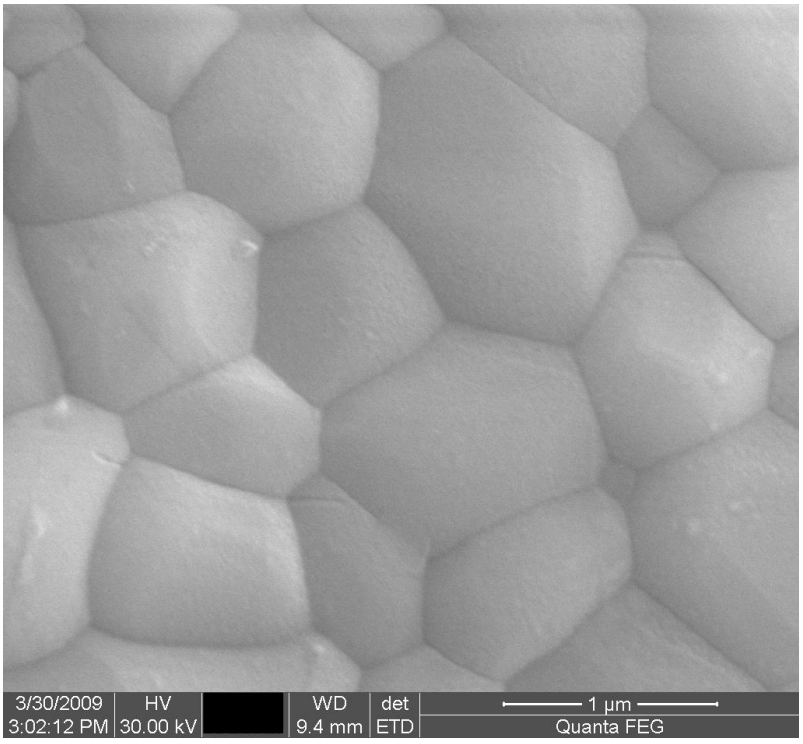

Figure 3.14 SEM image of the sample 1.2Mg0F0.

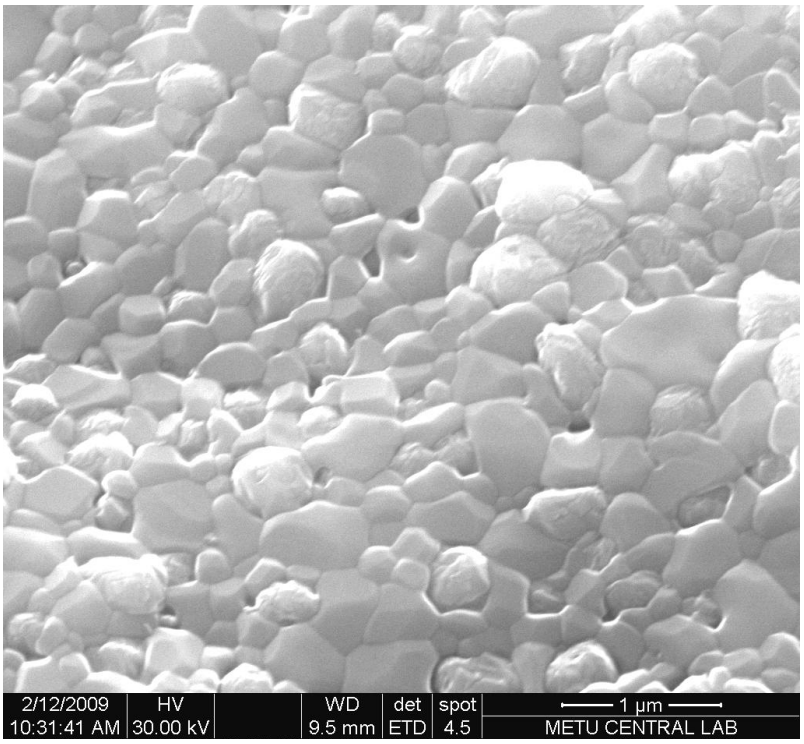

Figure 3.15 SEM image of the sample 1.95Mg2.5F2.5.

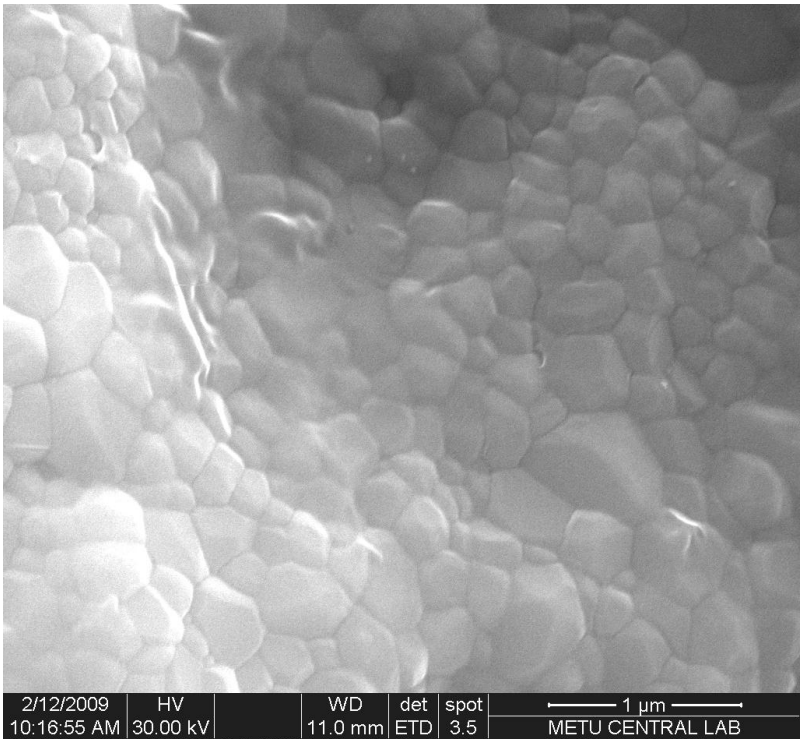

Figure 3.16 SEM image of the sample 1.625Mg2.5F2.5.

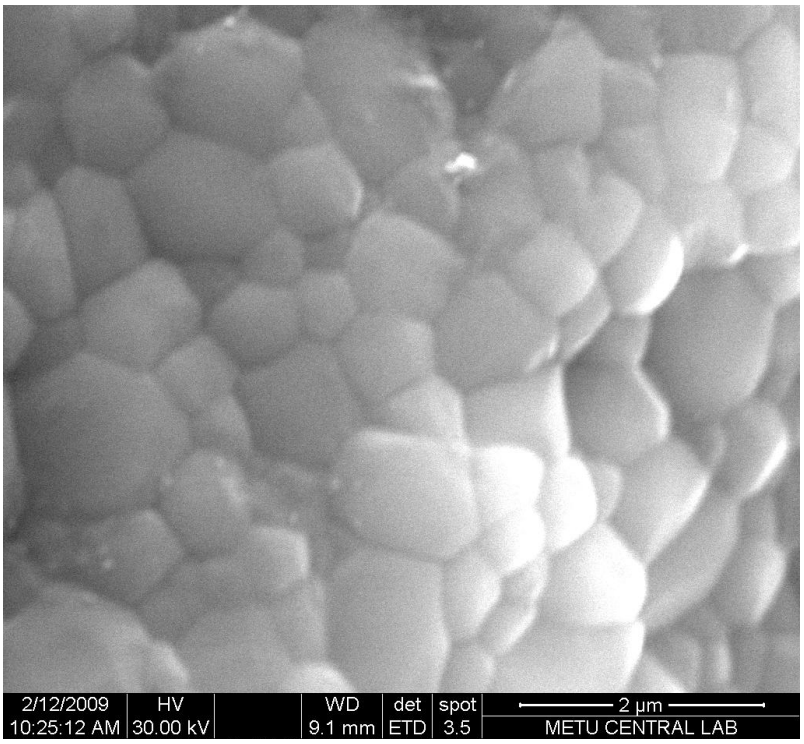

Figure 3.17 SEM image of the sample 1.463Mg2.5F2.5.

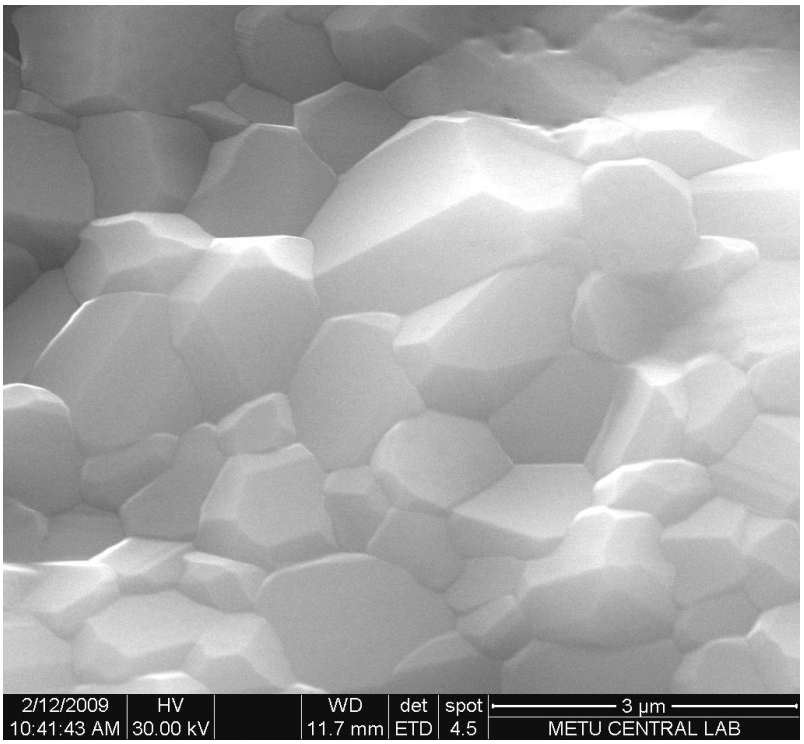

Figure 3.18 SEM image of the sample 1.17Mg2.5F2.5.

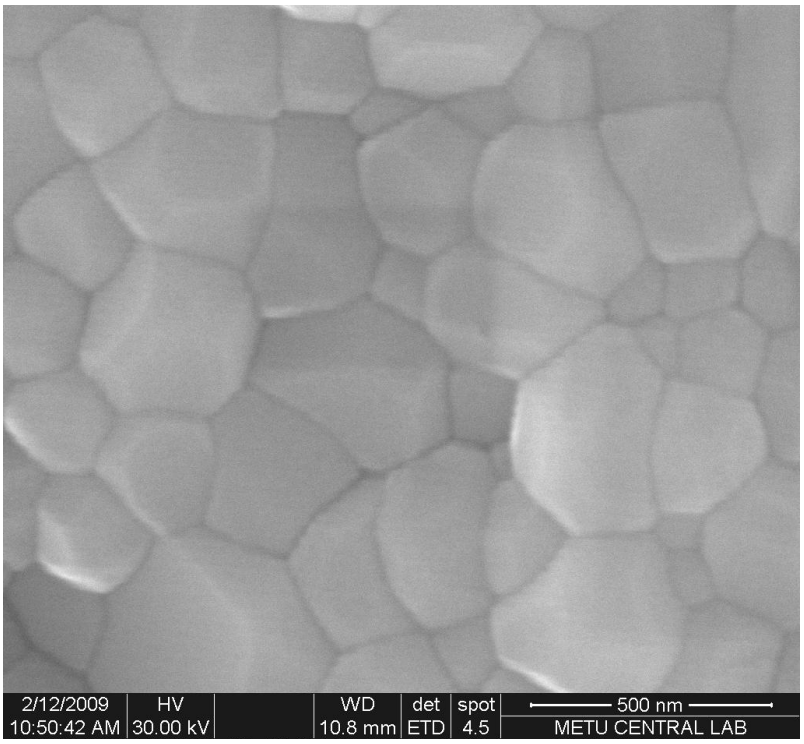

Figure 3.19 SEM image of the sample 1.65Mg1F2.5.

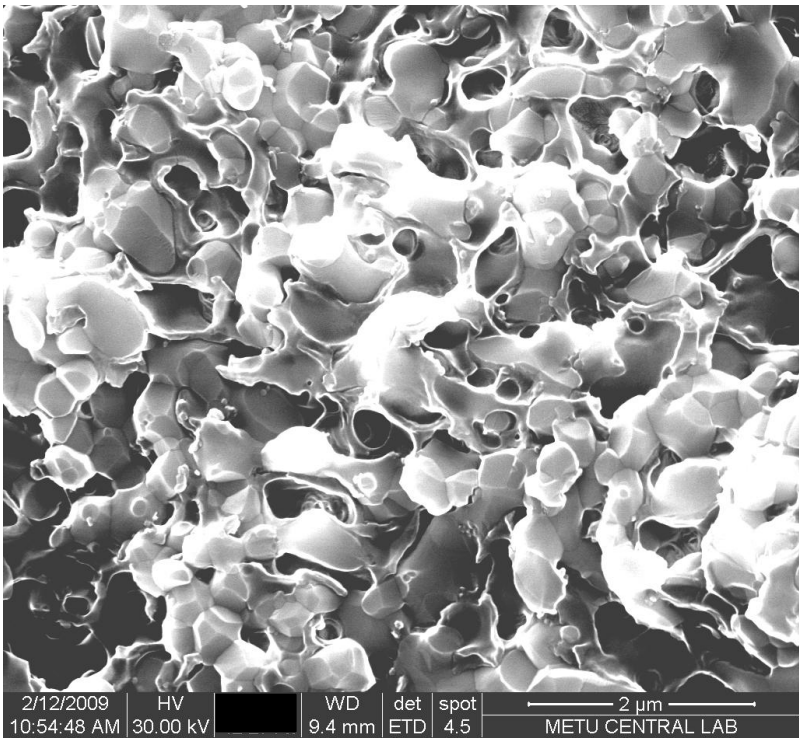

Figure 3.20 SEM image of the sample 1.542Mg7.5F2.5.

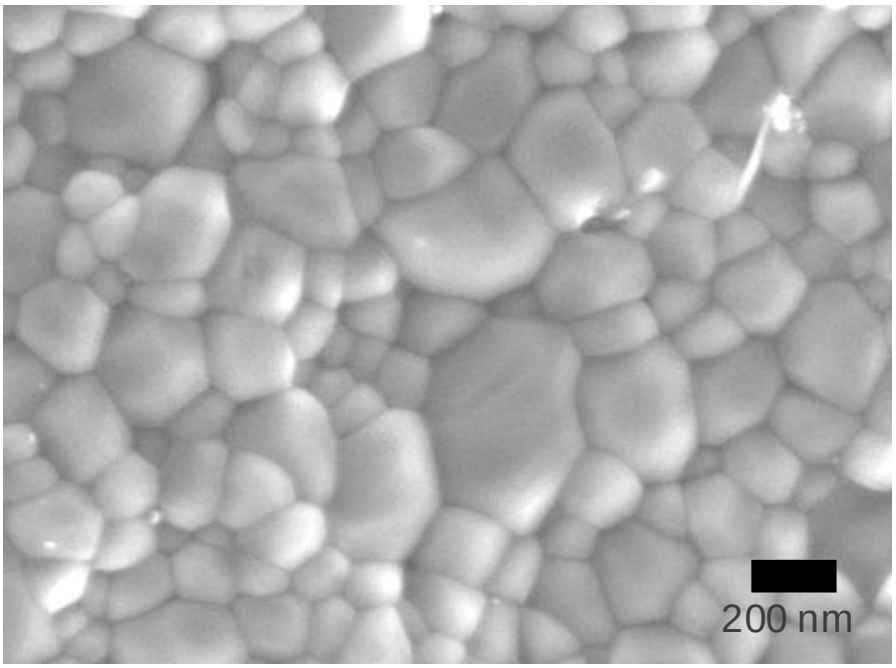

Figure 3.21 SEM image of the sample 1.65Mg1F0.

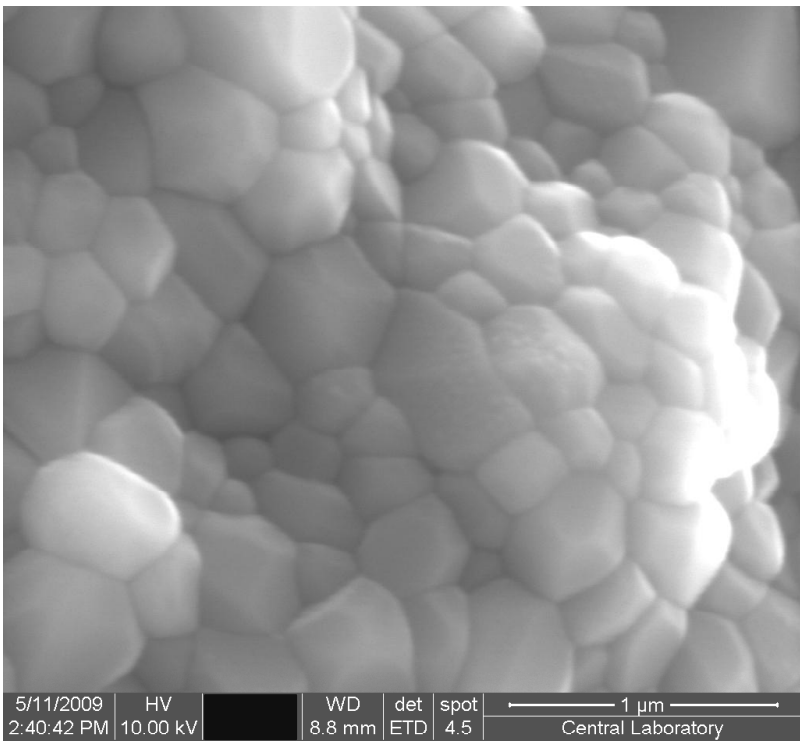

Figure 3.22 SEM image of the sample 1.625Mg2.5F0.

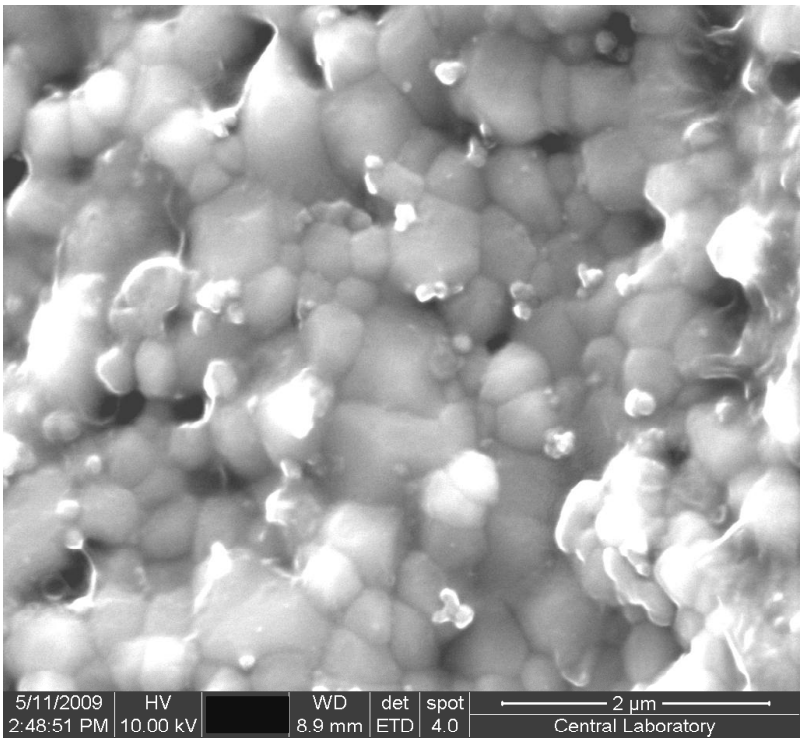

Figure 3.23 SEM image of the sample 1.542Mg7.5F0.

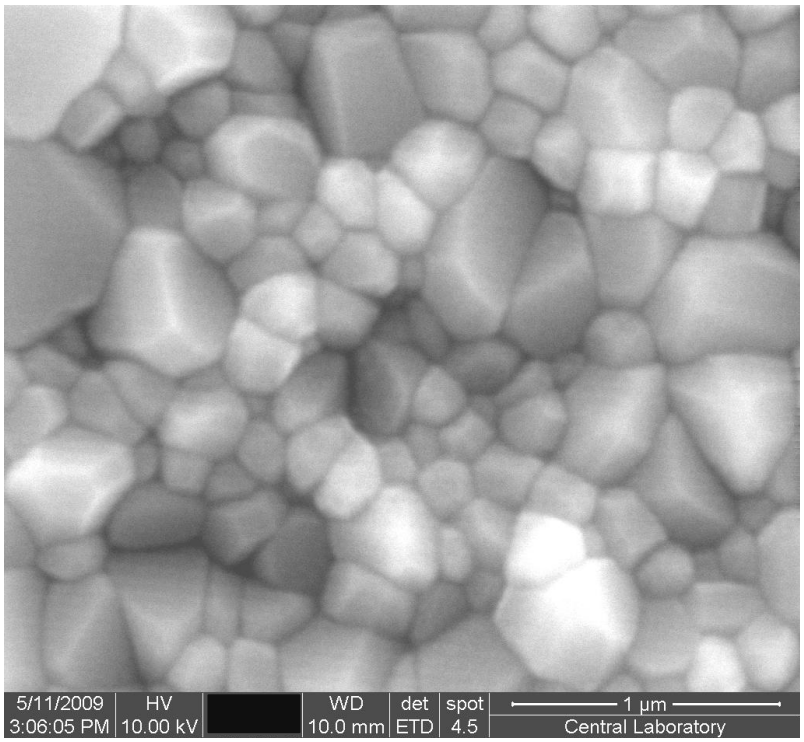

Figure 3.24 SEM image of the sample 1.625Mg2.5F7.5.

The SEM examinations revealed that the average grain sizes were generally increased with the increase in the β-TCP content. The presence of CaO phase (in sample 2Mg0F0 and 1.95Mg2.5F2.5) increased the average grain sizes of these samples, suggesting that the phase purity could be a factor in reducing the grain sizes. In group 2, the average grain sizes were increased with the decrease in the Ca/P ratios and therefore increase in the β-TCP content, except for sample 1.95Mg2.5F2.5 and sample 1.625Mg2.5F2.5 because of the presence of the CaO phase in sample 1.95Mg2.5F2.5.

In group 3, in which the Mg^{2+} ion amount varied from 1 to 7.5 mole % with constant amount of F^- ions, the smallest average grain size was achieved for 1 mole % Mg^{2+} and 2.5 mole % F^- (sample 1.65Mg1F2.5).

For very small concentrations of magnesia (MgO) substitutions (in the range of 0.25 to 3.00 wt%) into HAps, a gradual decrease in the average grain sizes was observed with the increase in the Mg^{2+} amount [129]. On the other hand, when the Mg^{2+} concentrations were ranged from 1 to 7.5 mole %, a decrease in the average grain sizes of the samples did not occur. Therefore, the smallest grain size was achieved for sample 1.65Mg1F2.5 doped with 1 mole % Mg^{2+} and 2.5 mole % F^-. However, for the sample 1.65Mg1F0 in group 4, which was doped with 1 mole % Mg, an increase was observed in the average grain size. Therefore, the decrease in the average grain size of sample 1.65Mg1F2.5 should not only be attributed to the presence of Mg^{2+} but also to the presence of F^- ions.

As the relative densities of the samples were decreased, a discontinuity in the pore distribution was observed for the samples in group 4 as the Mg^{2+} content was increased. It was previously shown that in Mg^{2+} doped HAps, large grains correspond to unsubstituted HAp while the substitution of Mg^{2+} for Ca^{2+} occurred in smaller grains [129].

In group 5, among the samples doped with a constant amount of Mg^{2+} content, as the F^- amount was increased from 0 to 7.5 mole %, the average grain size was gradually decreased.

Table 3.6 Average grain sizes of the samples.

Group No	Sample ID	Average Grain size (nm)
1	2Mg0F0	267
	1.67Mg0F0	261
	1.5Mg0F0	213
	1.2Mg0F0	566
2	1.95Mg2.5F2.5	261
	1.625Mg2.5F2.5	222
	1.463Mg2.5F2.5	636
	1.17Mg2.5F2.5	740
3	1.65Mg1F2.5	197
	1.625Mg2.5F2.5	222
	1.542Mg7.5F2.5	600
4	1.65Mg1F0	256
	1.625Mg2.5F0	245
	1.542Mg7.5F0	453
5	1.625Mg2.5F0	245
	1.625Mg2.5F2.5	222
	1.625Mg2.5F7.5	208

3.3 Mechanical Investigation of the Samples

3.3.1 Micro-hardness Measurements

The μ-hardness of the samples sintered at 1100ºC for 1 hr was determined to study the effects of the dopants to HAp and β-TCP. The μ-hardness values of the samples are presented in Figures 3.25-3.29. The surfaces of the samples were ground with abrasive papers (No. 600-1200) and finally polished with 1μm diamond paste. This procedure resulted in a removal of ~ 1mm thick layer to avoid the "skin" effect on mechanical properties of the internal part of the sintered samples [130].

In group 1, the highest μ-hardness value was obtained for Ca/P ratio of 2.00 and as the Ca/P ratio was decreased, μ-hardness was decreased gradually. Jarcho et al. determined the hardness of dense polycrystalline HAp ceramics sintered in air by Knoop method as equal to 4.8 GPa while the hardness of natural apatite reached to ~ 4.3 GPa [139].

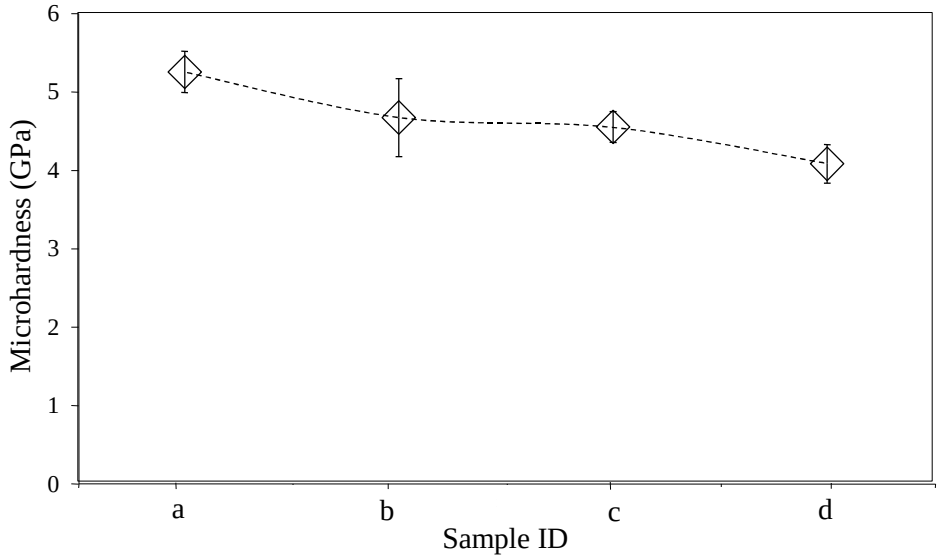

Figure 3.25 Micro-hardness values of the samples in group 1: a) Sample 2Mg0F0; b) Sample 1.67Mg0F0; c) Sample 1.5Mg0F0; d) Sample 1.2Mg0F0. All samples were sintered at 1100ºC for 1 hr.

In group 2, the gradual decrease in the μ-hardness values were also observed for the same variations of Ca/P ratios with 2.5 mole % Mg^{2+} and F^- addition. However, in group 2, the decrease in the μ-hardness values were started from a smaller value and reached to its minimum with a greater slope as a result of the Mg^{2+} addition. For the CaP precipitates with Ca/P ratios higher then 1.67 formed CaO phase besides HAp after the sintering at 1250ºC [130], which was also detected for the samples 2Mg0F0 and 1.95Mg2.5F2.5 in their XRD patterns. It was also reported that CaO can transform into $Ca(OH)_2$ in air and then partially to $CaCO_3$, which significantly decreases the hardness of the ceramics [130]. However, the micro hardness values of the samples 2Mg0F0 and 1.95Mg2.5F2.5 were found to be the highest among the groups 1 and 2 despite the presence of CaO phase. This behavior should suggest that CaO to $Ca(OH)_2$ transformation did not occur for these samples, which was also confirmed by the FTIR patterns of these samples.

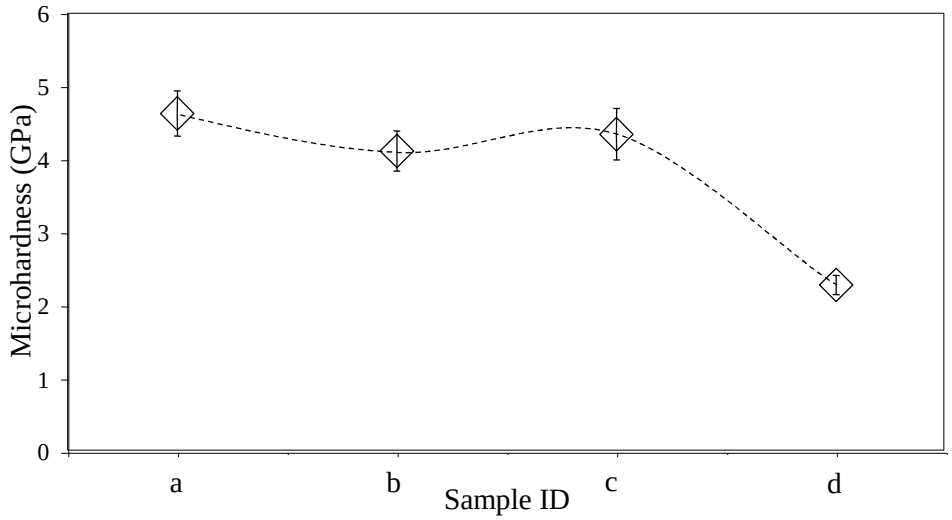

Figure 3.26 Micro-hardness values of the samples in group 2: a) Sample 1.95Mg2.5F2.5; b) Sample 1.625Mg2.5F2.5; c) Sample 1.463Mg2.5F2.5; d) Sample 1.17Mg2.5F2.5.

It was reported that the addition of Mg^{2+} ion into HAp ceramics resulted in reduction of both densities and the Vickers hardness values of the HAp ceramics [129]. In groups 3 and 4, the effect of increase in the Mg^{2+} amount with a constant amount of F dopant (2.5 mole %) and the effect of Mg^{2+} alone were investigated, respectively. The hardening effect of the F^- addition was confirmed by comparing the μ-hardness results for groups 3 and 4. The μ-hardness values showed the same characteristic slope in both groups.

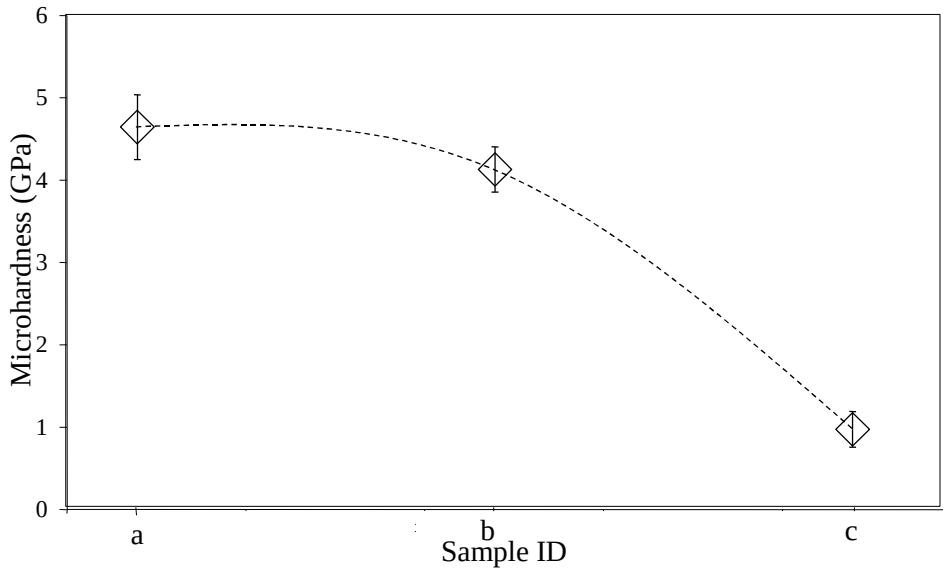

Figure 3.27 Micro-hardness values of the samples in group 3: a) Sample 1.65Mg1F2.5; b) Sample 1.625Mg2.5F2.5; c) Sample 1.542Mg7.5F2.5.

In group 4, with no F^- addition, the decrease in the μ-hardness values due to the increase in the Mg^{2+} amount was started from a smaller value in comparison with group 3. Generally, it was observed that in the absence of F^- ions, the μ-hardness values of the samples became smaller.

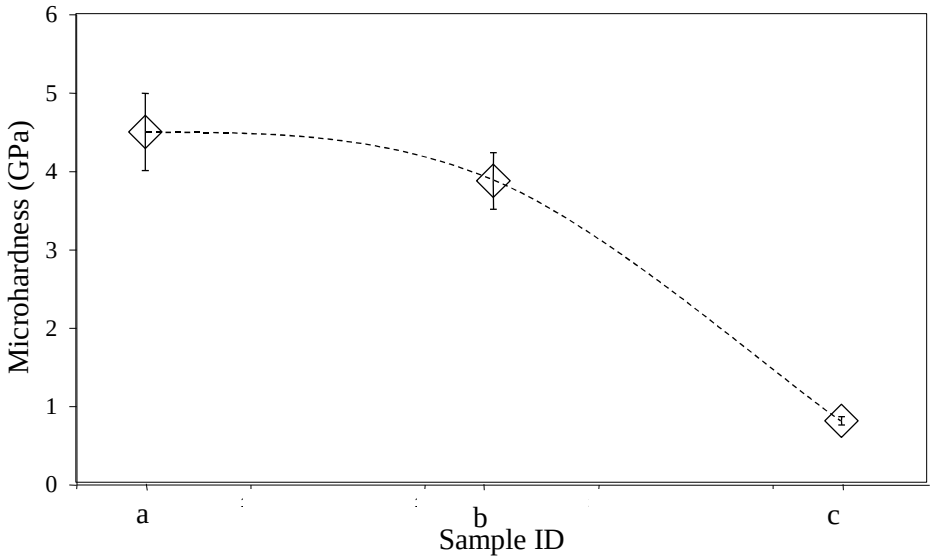

Figure 3.28 Micro-hardness values of the samples in group 4: a) Sample 1.65Mg1F0; b) Sample 1.625Mg2.5F0; c) Sample 1.542Mg7.5F0.

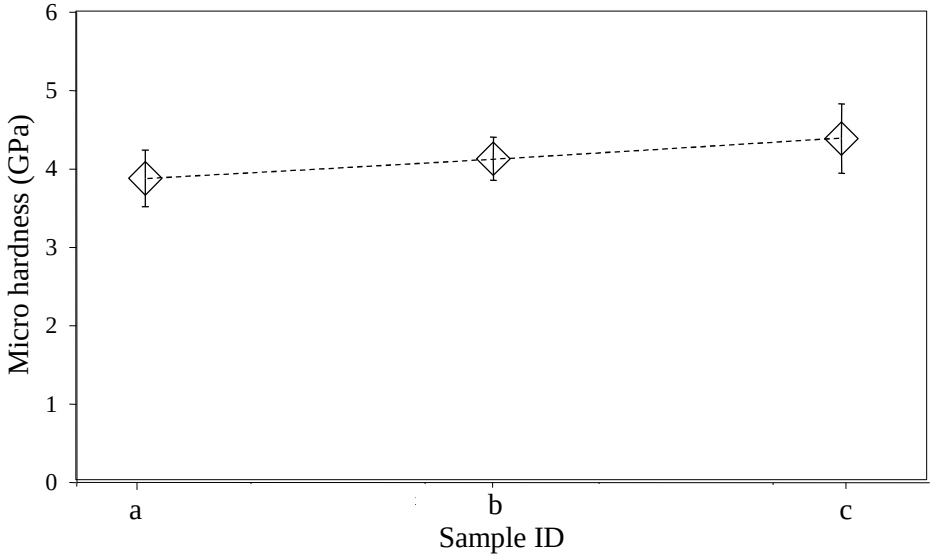

Figure 3.29 Micro-hardness values of the samples in group 5: a) Sample 1.625Mg2.5F0; b) Sample 1.625Mg2.5F2.5; c) Sample 1.625Mg2.5F7.5.

Finally, the affect of the increase in the F^- amount to the μ-hardness values was investigated, for group 5. The hardening effect of the F^- ion was also confirmed by the measurements among the compositions in this group. As seen in Figure 3.29, the increase in the μ-hardness values of the samples were proportional to the increase in the F^- amount.

3.3.2 Diametral Tensile Strength

Diametral tensile strength test has been widely applied to the biomaterials such as teeth prosthesis materials and cements used in the dentistry [127]. Because stresses formed on dental implants are similar to those that formed during the diametral tensile strength tests [146].

The densities of the samples used in the diametral tensile strength test were ranged between 77-91 % of their theoretical densities. The disks mostly broken into two pieces while for the ones with 7.5 mole % Mg^{2+} content, the disks were broken into three or more pieces. It was reported that the diametral strength values of the materials could vary according to porosity, poissons ratio, contact area during the test, diameter and thickness of the disks and distribution of the pores [146,147]. The influence of porosity to the diametral tensile strength has been studied with porosities ranging from 1 to 32 % [146]. It was found that the diametral strength of HAps increased with increasing the densities. Besides porosity, there are many factors (second phases, grain sizes, etc) affecting the diametral strength of the materials. Therefore, there is a wide range of diametral tensile strength values reported in the literature for the HAp ceramics. For a 100 % dense HAp, the diametral tensile strength was reported as 35 MPa [93]. However, for HAp with 45-50 % open pore structure, it was reported as 1-2 MPa [148].

Table 3.7 Diametral tensile strength values of the samples.

Group No	Sample ID	Relative densities (geometrical)	Diametral Tensile Strength (MPa)	Standard Deviation (± MPa)
1	2Mg0F0	87.5	10.99	4.625
	1.67Mg0F0	90.8	4.15	9.065
	1.5Mg0F0	90.1	11.40	8.216
	1.2Mg0F0	85.1	11.31	3.956
2	1.95Mg2.5F2.5	—	—	
	1.625Mg2.5F2.5	90.5	5.56	3.841
	1.463Mg2.5F2.5	90.1	8.51	11.254
	1.17Mg2.5F2.5	80.7	8.35	6.159
3	1.65Mg1F2.5	91.3	5.06	3.245
	1.625Mg2.5F2.5	90.5	5.56	3.841
	1.542Mg7.5F2.5	77.1	2.26	8.152
4	1.65Mg1F0	89.6	3.75	7.583
	1.625Mg2.5F0	89.2	5.15	8.718
	1.542Mg7.5F0	81.1	5.82	4.359
5	1.625Mg2.5F0	89.2	5.15	8.718
	1.625Mg2.5F2.5	90.5	5.56	3.841
	1.625Mg2.5F7.5	91.3	9.49	4.165

The results in Table 3.7 were not found to be in correlation with the relative densities of the samples except for the ones in group 3 and 5. This suggests that other parameters such as grain sizes, presence of other phases, effects of the substitution ions and also the distribution of the cavities within the samples should also be considered. It was reported that neck formations in the HAps and discontinuous cavities increased the strength of the samples [149].

It is known that the decrease in the grain size enhances the mechanical properties of the materials, especially if the grains are in nano-size. Because the average values of the grains are presented in Table 3.6, an accurate correlation cannot be constructed between Tables 3.6 and 3.7 due to the wide grain size distribution of the samples. In some of the samples, very small grains mixed with large grains can be seen in the SEM images. Despite the increase in the average grain sizes, the diametral tensile strength values were high in these samples. This might be due to the enhancing effects of these small grains that are distributed between the larger grains.

When a crack gets across a grain boundary, the energy dissipation occurs to decrease the driving force for the crack propagation [99]. It was reported that the powder characteristics, such as surface area and grain size distribution, significantly influenced the sintering ability of dense HAps and determined the strength and hardness values of the final sintered samples [150].

Presence of multi-phases, such as β-TCP and HAp, might lead to a reduction in the strengths of the HAp/ β-TCP biphasic ceramics. This might be due to the occurrence of stresses within the samples due to the differences in the CTE of the co-existing phases [131]. However, the use of the biphasic ceramics as biomaterials still holds their importance owing to their higher biological reactivity and better bonding with bones compared to the pure HAp [91,131]. It should be considered that the presence β-TCP phase has long term enhancing effects to the strengths of the materials owing to its higher dissolution rate that promotes bone in-growth. Interestingly, high values were achieved in group 1 for the samples 2Mg0F0, 1.5Mg0F0 and 1.2Mg0F0. In addition, the diametral tensile strength values were increased for the samples 1.463Mg2.5F2.5 and 1.17Mg2.5F2.5 with a constant amount of Mg^{2+} and F^{-} addition in group 2.

In group 3, a gradual decrease was observed for the samples with constant F^{-} content as the Mg^{2+} amount increased. It was reported that the addition of Mg^{2+} ion into HAps reduces the strengths of the ceramics [129,151].

Sample 1.65Mg1F0 had the smallest diametral tensile strength value among the samples in group 4. It was reported that in small amount of MgO substitution to

HAps, both transcrystallite fracture along the large grains and intercrystallite fractures along the small grains were observed [129]. This suggested that the introduction of small quantities of MgO into the samples promoted granular bond weakening in the samples [129], which might also be the reason of the low diametral tensile strength value of this sample. Although it was reported that increase in the Mg amount and the decrease in the densities led to a strength reduction in the samples, the diametral strength values were gradually increased for the samples in group 4. This might be attributed to the discontinuity of the cavities present in the samples that were revealed by the SEM pictures of this group.

The diametral tensile strength values of the samples 1.625Mg2.5F2.5, 1.65Mg1F2.5, 1.625Mg2.5F0 and 1.625Mg2.5F7.5 can be compared with that of pure HAp (sample 1.67Mg0F0) considering their relatively close average grain size and density values, which were found to be around 200-260 nm and 90 %, respectively. It can be seen from the diametral tensile strength results (Table 3.7) that the substitutions of these ions generally had an enhancing effect on the CaPs when compared to pure HAp. Because of the simultaneous presence of many parameters mentioned above, more studies should be employed with less parameters that affect the diametral tensile strength values of the samples in order to study each of these parameters effectively.

CHAPTER 4

CONCLUSIONS

In this study, CaPs with ratios ranging from 1.17 to 2.00 were produced by precipitation method. Mg^{2+} and/or F^- ions were doped into this material with varying amounts in order to investigate its microstructural and mechanical properties. Additionally, with the addition of Mg^{2+} ions to HAp/β-TCP biphasic ceramics were produced with varying ratios, which are tailored both with the Ca/P ratios of the precursors and the Mg^{2+} amounts. All the samples were sintered at 1100ºC for 1 hr.

The densities measured by the Archimedes method were higher compared to the ones measured by the geometrical method due to the difference in the preparation methods. High densities were achieved for the pure and doped HAps except for the ones doped with 7.5 mole % Mg^{2+}.

The XRD patterns revealed that the increase in the β-TCP phase was proportional to the increase in the Mg^{2+} content and inversely proportional to the decrease in the Ca/P ratios and the F content. The hexagonal lattice parameter measurements revealed the substitution of the ions into the apatite structure. The FTIR measurements revealed that all of the samples showed the characteristic bands for HAp and β-TCP. SEM images revealed the grain sizes in the range of 197 nm-740 nm. The grain sizes were generally increased with the increase in the Mg^{2+} content and decreased with the increase in the F^- content.

The micro hardness values of the samples were also decreased with the increase in Mg^{2+} ions and therefore β-TCP amount and increased with the increase in the F^- amount. As a result of the distribution of smaller grains in between the larger grains, a relative increase in the diametral tensile strength values was observed. Due to existance of many parameters affecting the diametral tensile strength values, these values were not found to be in correlation with the relative densities for all of the samples. The mechanical properties of the CaPs produced in

this study was not still high enough for load-bearing applications. However, it should be also considered that the presence β-TCP phase has long term enhancing effects to the strengths of the materials owing to its higher dissolution rate.

REFERENCES

[1] Cao G., Nanostructures and Nanomaterials, Singapore: World Scientific Publishing Company (2004), 16-18.

[2] Suryanarayana C., Koch C.C., Nanostructured Materials, Pergamon Materials Series, Volume 2 (1999), 313-344.

[3] Siegel R.W., "Nanostructured materials –mind over matter", Nanostructured Materials 4 (1994), 121-138.

[4] Kalita S.J., Bhardwaj A., Bhatt H.A., "Nanocrystalline calcium phosphate ceramics in biomedical engineering", Materials Science and Engineering C 27 (2007), 441-449.

[5] Meyers M.A., Mishra A., Benson D.J., "Mechanical properties of nanocrystalline materials", Progress in Materials Science 51 (2006), 427-556.

[6] Dominguez-Rodriguez A., Gomez-Garcia D., Zapata-Solvas E., Shen J.Z., Chaim R., "Making ceramics ductile at low homologous temperatures", Scripta Materialia 56 (2007), 89-91.

[7] Vaßen R., Stöver D., "Processing and properties of nanophase ceramics", Journal of Materials Processing Technology 92-93 (1999), 77-84.

[8] Karch J., Birringer R., Gleiter H., "Ceramics ductile at low temperature", Nature 330 (1987), 556-558.

[9] Szlufarska I., Nakano A., Vashishta P., “A crossover in the mechanical response of nanocrystalline ceramics”, Science 309 (2005), 911-914.

[10] Bertoni E., Bigi A., Cojazzi G., Gandolfi M., Panzavolta S., Roveri N., “Nanocrystals of magnesium and fluoride substituted hydroxyapatite” Journal of Inorganic Biochemistry 72 (1998), 29-35.

[11] Popp U., Herbig R., Michel G., Müller E., Oestreich C., “Properties of nanocrystalline ceramic powders prepared by laser evaporation and recondensation”, Journal of the European Ceramic Society 18 (1998), 1153-1160.

[12] Lamas D.G., Lascalea G.E., de Reca N.E.W., “Synthesis and characterization of nanocrystalline powders for partially stabilized zirconia ceramics”, Journal of the European Ceramic Society 18 (1998), 1217-1221.

[13] Juárez R.E., Lamas D.G., Lascalea G.E., de Reca N.E.W., “Synthesis of nanocrystalline zirconia powders for TZP ceramics by a nitrate–citrate combustion route”, Journal of the European Ceramic Society 20 (2000), 133-138.

[14] Laberty-Robert Ch., Ansart F., Deloget C., Gaudon M., Rousset A., “Powder synthesis of nanocrystalline ZrO_2–8%Y_2O_3 via a polymerization route”, Materials Research Bulletin 36 (2001), 2083-2101.

[15] Thangadurai P., Sabarinathan V., Chandra Bose A., Ramasamy S., “Conductivity behavior of a cubic/tetragonal phase stabilized nanocrystalline La_2O_3-ZrO_2”, The Journal of Physics and Chemistry of Solids 65 (2004), 1905-1912.

[16] Zhang Y.C., Qiao T., Hu X.Y., “Preparation of Mn_3O_4 nanocrystallites by low-temperature solvothermal treatment of γ-MnOOH nanowires”, Journal of Solid State Chemistry 177 (2004), 4093-4097.

[17] Bykov Y., Gusev S., Eremeev A., Holoptsev V., Malygin N., Pivarunas S., Sorokin A., Shurov A., “Sintering of nanophase oxide ceramics by using millimeter-wave radiation”, Nanostructured Materials 6 (1995), 855-858.

[18] Liao S.C., Chen Y.J., Mayo W.E., Kear B.H., “Transformation-assisted consolidation of bulk nanocrystalline TiO_2”, Nanostructured Materials 11 (1999), 553-557.

[19] Duan R.G., Zhan G.D., Kuntz J.D., Kear B.H., Mukherjee A.K., “Processing and microstructure of high pressure consolidated ceramic nanocomposites”, Scripta Materialia 51 (2004), 1135-1139.

[20] Li J., Ye Y., Shen L., Chen J., Zhou H., “Densification and grain growth during pressureless sintering of TiO_2 nanoceramics”, Materials Science and Engineering A 390 (2005), 265-270.

[21] Akurati K.K., Bhattacharya S.S.,Winterer M., Hahn H., “Synthesis, characterization and sintering of nanocrystalline titania powders produced by chemical vapour synthesis”, Journal of Physics D: Applied Physics 39 (2006), 2248-2254.

[22] Morsi K., Keshavan H., Bal S., “Hot pressing of graded ultrafine-grained alumina bioceramics”, Materials Science & Engineering A 386 (2004), 384-389.

[23] Laha T., Balani K., Agarwal A., Patil S., Seal S., “Synthesis of nanostructured spherical aluminum oxide powders by plasma engineering”, Metallurgical and Materials Transactions A 36 (2005), 301-309.

[24] Tok A.I.Y., Boey F.Y.C., Zhao X.L., “Novel synthesis of Al_2O_3 nano-particles by flame spray pyrolysis”, Journal of Materials Processing Technology 178 (2006), 270-273.

[25] Meng F., Fu Z., Zhang J., Wang H., Wang W., Wang Y., Zhang Q., "Rapid densification of nano-grained alumina by high temperature and pressure with a very high heating rate", Journal of the American Ceramic Society 90 (2007), 1262-1264.

[26] Elliot J.C., "Structure and Chemistry of the Apatites and Other Calcium Orthophosphates", Studies in Inorganic Chemistry 18, Elsevier (1994).

[27] Brown W.E., "Crystal growth of bone mineral", Clinical Orthopaedics and Related Research 44 (1966), 205-220.

[28] Brown W.E., Eidelman N., Tomazic B., "Octacalcium phosphate as a precursor in biomineral formation", Advances in Dental Research 1 (1987), 306-313.

[29] Billottee W.G., Ceramic Materials in: Park J.B., Bronzino J.D., (Eds.), in "Biomaterials: Principles and Applications", CRC Press, Boca Raton, FL, USA (2002).

[30] De Groot K., Klein C.P.A.T., Wolke J.G.C., Blieck-Hogervorst J.M.A., "Chemistry of calcium phosphate bioceramics", CRC Handbook of Bioactive Ceramics, Calcium Phosphate and Hydroxylapatite Ceramics II, CRC press, Boca Raton, FL, (1990).

[31] Sudarsanan K., Mackie P.E., Young R.A., "Comparison of synthetic and mineral fluorapatite, $Ca_5(PO_4)_3F$, in crystallographic detail", Materials Research Bulletin 7 (1972), 1331-1338.

[32] Fluorapatite mineral data, last visited on 24 March 2009, http://www.webmineral.com/data/Fluorapatite.shtml.

[33] Mackie P.E., Elliot J.C., Young R.A., "Monoclinic structure of synthetic $Ca_5(PO_4)_3Cl$, chloroapatite", Acta Crystallographica Section B 28 (1972),1840-1848.

[34] Chlorapatite mineral data, last visited on 24 March 2009, http://www.webmineral.com/data/Chlorapatite.shtml.

[35] Elliot J.C., Dykes E., Mackie P.E., "Structure of bromapatite and the radius of bromide ion", Acta Crystallographica Section B 37 (1981), 435-438.

[36] Elliot J.C., "Space group and lattice constants of $Ca_{10}(PO_4)_6CO_3$", Journal of Applied Crystallography 13 (1980), 618-621.

[37] Negas T., Roth R.S., "High temperature dehydroxylation of apatatic phosphates", Journal of Research of the National Bureau of Standards 72A (1968), 783-787.

[38] Strontium apatite mineral data, last visited on 24 March 2009, http://www.webmineral.com/data/Strontium-apatite.shtml.

[39] Hata M., Okada K., Iwai S., Akao M., Aoki H., "Cadmium hydroxyapatite", Acta Crystallographica B34 (1978), 3062-3064.

[40] Brückner S., Lusvardi G., Menabue L., Saladini M., "Crystal structure of lead hydroxyapatite from powder x-ray diffraction data", Inorganica Chimica Acta 236 (1995), 209-212.

[41] Legeros R.Z., "Biological and Synthetic Apatites", In: Brown P.W., Constantz B., editors. Hydroxyapatite and Related Materials, (1994) CRC press.

[42] Yoshimura M., Suda H., “Hydrothermal processing of hydroxyapatite: Past, present and future”, In: Brown P.W., Constantz B., editors. Hydroxyapatite and Related Materials, (1994) CRC press.

[43] Smith D.K., “Calcium phosphate apatites in nature”, In: Brown P.W., Constantz B., editors. Hydroxyapatite and Related Materials, (1994) CRC press.

[44] Weatherell J.A., Robinson C., “The inorganic composition of teeth”; in Zipkin I. (ed): Biological Mineralization, NY, USA, John Wiley (1973), 43-74.

[45] Dallemagne M.J., Richelle L.J., “Inorganic chemistry of bone”; in Zipkin I. (ed): Biological Mineralization, NY, USA, John Wiley (1973), 23-42.

[46] Song Q., Wang C., Wen S., “Effects of doping on crystal and grain boundary in human enamel”, Materials Science and Engineering A 297 (2001), 272-280.

[47] Krajewski A., Ravaglioli A., Wen S., Feng J.W., “Microstructural features of synthetic ceramized chlorapatite in comparison with human enamel crystals”, Journal of Applied Crystallography 25 (1992), 465-470.

[48] Driessens F.C.M., in: Groot K.D. (Ed.), Bioceramics of calcium phosphate, CRC Press, Boca Raton, FL, USA (1983).

[49] Van Landuyt P., Li F., Keustermans J.P., Streydio J.M., Delannay F., Munting E., “The influence of high sintering temperatures on the mechanical properties of hydroxyapatite”, Journal of Materials Science: Materials in Medicine 6 (1995), 8-13.

[50] Xu J.L., Khor K.A., Dong Z.L., Gu Y.W., Kumar R., Cheang P., "Preparation and characterization of nano-sized hydroxyapatite powders produced in a radio frequency (rf) thermal plasma", Materials Science and Engineering A 374 (2004), 101-108.

[51] Aronov D., Karlov A., Rosenman G., "Hydroxyapatite nanoceramics: Basic physical properties and biointerface modification", Journal of the European Ceramic Society 27 (2007) 4181-4186.

[52] Itokazu M., Yang W., Aoki T., Ohara A., Kato N., "Synthesis of antibiotic-loaded interporous hydroxyapatite blocks by vacuum method and in vitro drug release testing", Biomaterials 19 (1998), 817-819.

[53] Evis Z., Doremus R.H., "Coatings of hydroxyapatite-nanosize alpha alumina composites on Ti-6Al-4V", Materials Letters 59 (2005), 3824-3827.

[54] Legeros R.Z., Legeros J.P., In: Hench L.L., Wilson J., editors, "An Introduction to Bioceramics", World Scientific Publishing Company, Singapore (1993), 139.

[55] Grote J.J., "Biocompatible materials in chronic ear surgery", In: Brachmann D., editor, Otologic Surgery, Philadelphia, PA: W.B. Saunders (1994), 185-200.

[56] Mobasherpour I., Heshajin M.S., Kazemzadeh A., Zakeri M. "Synthesis of nanocrystalline hydroxyapatite by using precipitation method", Journal of Alloys and Compounds 430 (2007), 330-333.

[57] Ahn E.S., Gleason N.J., Nakahira A., Ying J.Y., "Nanostructure processing of hydroxyapatite-based bioceramics", Nano Letters 1 (2001), 149-153.

[58] Chen F., Wang Z.C., Lin C.J., “Preparation and characterization of nano-sized hydroxyapatite particles and hydroxyapatite/chitosan nano-composite for use in biomedical materials”, Materials Letters 57 (2002), 858–861.

[59] Sarig S., Kahana F., “Rapid formation of nanocrystalline apatite”, Journal of Crystal Growth 237-239 (2002), 55-59.

[60] Kuriakose T.A., Kalkura S.N., Palanichamy M., Arivuoli D., Dierks K., Bocelli G., Betzel C., “Synthesis of stoichiometric nano crystalline hydroxyapatite by ethanol-based sol–gel technique at low temperature”, Journal of Crystal Growth 263 (2004), 517-523.

[61] Pang Y.X., Bao X., “Influence of temperature, ripening time and calcination on the morphology and crystallinity of hydroxyapatite nanoparticles”, Journal of the European Ceramic Society 23 (2003), 1697-1704.

[62] Manuell C.M., Ferraz M.P., Monteiro F.J., “Synthesis of hydroxyapatite and tricalcium phosphate nanoparticles – preliminary studies”, Key Engineering Materials 240-242 (2003), 555-558.

[63] Bose S., Saha S.K., “Synthesis of hydroxyapatite nanopowders via sucrose templated sol–gel method”, Journal of the American Ceramic Society 86 (2003), 1055-1057.

[64] Shih W.J., Chen Y.F., Wang M.C., Hon M.H., “Crystal growth and morphology of the nano-sized hydroxyapatite powders synthesized from $CaHPO_4 \cdot 2H_2O$ and $CaCO_3$ by hydrolysis method”, Journal of Crystal Growth 270 (2004), 211-218.

[65] Ramesh S., Tan C.Y., Sopyan I., Hamdi M., Teng W.D., “Consolidation of nanocrystalline hydroxyapatite powder”, Science and Technology of Advanced Materials 8 (2007), 124-130.

[66] Manafi S.A., Yazdani B., Rahimiopour M.R., Sadrnezhaad S.K., Amin M.H., Razavi M., “Synthesis of nano-hydroxyapatite under a sonochemical/ hydrothermal condition”, Biomedical Materials 3 (2008), 1-6.

[67] Wang C.K., Ju C.P., Chern Lin J.H., “Effect of doped bioactive glass on structure and properties of sintered hydroxyapatite”, Materials Chemistry and Physics 53 (1998), 138-149.

[68] Royer A., Viguie J.C., Heughebaert M., Heughebaert J.C., “Stoichiometry of hydroxyapatite: Influence on the flexural strength”, Journal of Materials Science: Materials in Medicine 4 (1993), 76-82.

[69] Wang P.E., Chaki T.K., “Sintering behaviour and mechanical properties of hydroxyapatite and dicalcium phosphate”, Journal of Materials Science: Materials in Medicine 4 (1993), 150-158.

[70] Meyers M.A., Chen P.Y., Lin A.Y.M., Seki Y., “Biological materials: Structure and mechanical properties”, Progress in Materials Science 53 (2008), 1-206.

[71] Turner C.H., Rho J., Takano Y., Tsui T.Y., Pharr G.M., “The elastic properties of trabecular and cortical bone tissues are similar: Results from two microscopic measurement techniques”, Journal of Biomechanics 32 (1999), 437-441.

[72] He L.-H., Standard O.C., Huang T.T.Y., Latella B.A., Svain M.V., “Mechanical behavior of porous hydroxyapatite”, Acta Biomaterialia 4 (2008), 577-586.

[73] Klawitter J.J., Hulbert S.F., “Application of porous ceramics for the attachment of load bearing internal orthopedic applications”, Journal of Biomedical Materials Research (1971), 161-229.

[74] Ayers R.A., Wolford L.M., Bateman T.A., Ferguson V.L., Simske S.J., “Qualification of bone ingrowth into porous block hydroxyapatite in humans”, Journal of Biomedical Materials Research 47 (1999), 54-59.

[75] De With G., Van Dijk H.J.A., Hattu N., Prijs K., “Preparation, microstructure and mechanical properties of dense polycrystalline hydroxyapatite”, Journal of Materials Science 16 (1981), 1592-1598.

[76] Akao M., Aoki H., Kato K., “Mechanical properties of sintered hydroxyapatite for prosthetic applications”, Journal of Materials Science 16 (1981), 809-812.

[77] Ruys A.J., Wei M., Sorrell C.C., Dickson M.R., Brandwood A., Milthorpe B.K., “Sintering effects on the strength of hydroxyapatite”, Biomaterials 16 (1995), 409-415.

[78] Suchanek W., Yoshimura, M., “Processing and properties of hydroxyapatite-based biomaterials for use as hard tissue replacement implants”, Journal of Materials Research 13 (1998), 94-117.

[79] Nalla R.K., Kinney J.H., Ritchie R.O., “Effect of orientation on the in vitro fracture toughness of dentin: the role of toughening mechanisms”, Biomaterials 24 (2003), 3955-3968.

[80] Guyton A.C., Textbook of Medical Physiology, 8th ed. Philadelphia, PA, USA: W.B. Saunders Company (1991).

[81] Kaplan F.S., Hayes W.L., Keaveny T.M., Boskey A., Einhorn T.A., Iannotti J.P., “Form and function of bone. In: Simon S.P., editor, Orthopaedic Basic Research, Columbus, OH, USA: American Academy of Orthopaedic Surgeons (1994), 127-185.

[82] Webster T.J., Massa-Schlueter E.A., Smith J.L., Slamovich E.B., “Osteoblast response to hydroxyapatite doped with divalent and trivalent cations”, Biomaterials 25 (2004), 2111-2121.

[83] Narasaraju T.S.B., Phebe D.E., “Some physico-chemical aspects of hydroxylapatite”, Journal of Materials Science 31 (1996), 1-21.

[84] Webster T.J., Ergun C., Doremus R.H., Bizios R., “Hydroxylapatite with substituted magnesium, zinc, cadmium, and yttrium. II. Mechanisms of osteoblast adhesion”, Journal of Biomedical Materials Research 59 (2002), 312-317.

[85] Shannon R.D., “Revised effective ionic-radii and systematic studies of interatomic distances in halides and chalcogenides”, Acta Crystallographica Section A 32 (1976), 751-767.

[86] Koutsoukos P.G., Nancollas G.H., “Influence of strontium ion on the crystallization of hydroxyapatite from aqueous solution”, Journal of Physical Chemistry 85 (1981), 2403-2408.

[87] Koutsoukos P.G., Nancollas G.H., “The effect of lithium on the precipitation of hydroxyapatite from aqueous solutions”, Colloids and Surfaces 17 (1986), 361-370.

[88] Wilson J.W., Werness P.G., Smith L.H., “Inhibitors of crystal growth of hydroxyapatite: a constant composition approach”, Journal of Urology 134 (1985), 1255-1258.

[89] Legeros R.Z., “Incorporation of magnesium in synthetic and biological apatites”, in Fearnhead R.W., Suga S. (eds): Tooth enamel IV, Amsterdam, Elsevier (1984), 32-36.

[90] Machoy-Mokrzynska A., “Fluoride- magnesium interaction”, Fluoride, Journal of the International Society for Fluoride Research 28 (1995), 175-177.

[91] Kannan S., Ferreira J.M.F., “Synthesis and thermal stability of hydroxyapatite-beta-tricalcium phosphate composites with cosubstituted sodium, magnesium, and fluorine”, Chemistry of Materials 18 (2006), 198-203.

[92] Gineste L., Gineste M., Ranz X., Ellefterion A., Guilhem A., Rouquet N., Frayssinet P., “Degradation of hydroxylapatite, fluorapatite, and fluorhydroxyapatite coatings of dental implants in dogs”, Journal of Biomedical Materials Research 48 (1999), 224-234.

[93] Bigi, A., Foresti, E., Gregorini, R., Ripamonti, A., Roveri, N., Shah, J.S., “The role of magnesium on the structure of biological apatite”, Calcified Tissue International 50 (1992), 439-444.

[94] Bigi A., Falini, G., Foresti, E., Gazzano, M., Ripamonti, A., Roveri, N., “Magnesium influence on hydroxyapatite crystallization”, Journal of Inorganic Biochemistry 49 (1993), 69-78.

[95] TenHuisen K.S., Brown P.W., “Effects of magnesium on the formation of calcium-deficient hydroxyapatite from $CaHPO_4 \cdot 2H_2O$ and $Ca_4(PO_4)_2O$”, Journal of Biomedical Materials Research 36 (1997), 306-314.

[96] Le Geros, R.Z., Calcium phosphates in oral biology and medicine. In Monographs in Oral Science, Vol. 15, ed. K. H. Myers. AG Publishers, Basel, Switzerland, (1991), 82-107.

[97] Percival M., “Bone health and osteoporosis”, Applied Nutritional Science Reports 5 (1999), 1-5.

[98] Cao X., Harris W., “Carbonate and magnesium interactive effect on calcium phosphate precipitation”, Environmental Science & Technology 42 (2008), 436-442.

[99] Ryu H.-S., Hong K.S., Lee J.-K., Kim D.J., Lee J.H., Chang B.-S., Lee D., Lee C.-K., Chung S.-S., “Magnesia-doped HA/β-TCP ceramics and evaluation of their biocompatibility” Biomaterials 25 (2004), 393-401.

[100] Gibson I.R., Bonfield W., “Preparation and characterization of magnesium/ carbonate co-substituted hydroxyapatites” Journal of Materials Science: Materials in Medicine 13 (2002), 685-693.

[101] Kannan S., Ventura J.M., Ferreira J.M.F., “Aqueous precipitation method for the formation of Mg-stabilized β-tricalcium phosphate: An x-ray diffraction study”, Ceramics International 33 (2007), 637-641.

[102] Xue W., Dahlquist K., Banerjee A., Bandyopadhyay A., Bose S., “Synthesis and characterization of tricalcium phosphate with Zn and Mg based dopants”, Journal of Materials Science: Materials in Medicine 19 (2008), 2669-2677.

[103] Tian J., Zhang S., Shao Y., Shan H., “Nanosize SiC particle reinforced hydroxyapatite composites”, In: Proceedings of the Bioceramics: Materials and Applications II Symposium (1995), 107-114.

[104] Evis Z., Doremus R.H., 2006, “Effect of MgF_2 on hot pressed hydroxylapatite and monoclinic zirconia composites”, Journal of Materials Science 42 (2007), 3739-3744.

[105] Sugiyama K., Tokonami M., “Structure and crystal chemistry of a dense polymorph of tricalcium phosphate $Ca_3(PO_4)_2$: A host to accommodate large lithophile elements in the earth’s mantle”, Physics and Chemistry of Minerals 15 (1987), 125-130.

[106] Famery R., Richard N., Boch P., “Preparation of α- and β-tricalcium phosphate ceramics, with and without magnesium addition”, Ceramics International 20 (1994), 327-336.

[107] Welch J.H., Gutt W., “High-temperature studies of the system calcium oxide-phosphorous pentoxide”, Journal of the Chemical Society (1961), 4442-4444.

[108] Wei X., Akinc M., “Crystal structure analysis of Si- and Zn-codoped tricalcium phosphate by neutron powder diffraction”, Journal of the American Ceramic Society 90, (2007), 2709-2715.

[109] Chang B.S., Lee C.K., Hong K.S., Youn H.J., Ryu H.S., Chung S.S., Park K.W., “Osteoconduction at porous hydroxyapatite with various pore configurations”, Biomaterials 21 (2000), 1291-1298.

[110] Yu D., Wong J., Matsuda Y., Fox J.L., Higuchi W.I., Otsuka M., “Self-setting hydroxyapatite cement: A novel skeletal drug-delivery system for antibiotics”, Journal of Pharmaceutical Sciences 81 (1992), 529- 534.

[111] Boskey A.L., Bone Mineralization; Bone Mechanics Handbook, 2nd edition, CRC Press (2001).

[112] Jee W.S.S., Integrated Bone Tissue Physiology: Anatomy and Physiology; Bone Mechanics Handbook, 2nd edition, CRC Press (2001).

[113] Currey J.D., Bones: Structure and Mechanics, Princeton, NJ: Princeton University Press (2002).

[114] Han Y., Xu K., Montay G., Fu T., Lu J., "Evaluation of nanostructured carbonated hydroxyapatite coatings formed by a hybrid process of plasma spraying and hydrothermal synthesis", Journal of Biomedical Materials Research 60 (2002), 511-516.

[115] Fratzl P., Gupta H.S., Paschalis E.P., Roschger P., "Structure and mechanical quality of the collagen-mineral nano-composite in bone", Journal of Materials Chemistry 14 (2004), 2115 -2123.

[116] Rho J.Y., Khun-Spearing L., Zioupos P., "Mechanical properties and the hierarchical structure of bone ", Medical Engineering & Physics 20 (1998), 92-102.

[117] Evis Z., "Al^{3+} doped nano-hydroxyapatites and their sintering characteristics", Journal of the Ceramic Society of Japan 114 (2006), 1001-1004.

[118] Evis Z., Ergun C., Doremus R.H., "Hydroxylapatite-zirconia composites: Thermal stability of phases and sinterability as related to the $CaO\text{-}ZrO_2$ phase diagram", Journal of Materials Science 40 (2005), 1127-1134.

[119] Joint Committee on Powder Diffraction Standards; Hydroxyapatite data (#09-0432).

[120] Joint Committee on Powder Diffraction Standards; β-tricalcium phosphate data (#09-0169).

[121] Evis Z., "Reactions in hydroxylapatite-zirconia composites", Ceramics International 33 (2007), 987-991.

[122] Cullity B.D., “Elements of X-ray diffraction”, 2nd edn., Addison-Wesley Publishing company, Massachusetts, USA (1978).

[123] Hilliard J.E., “Estimating grain size by the intercept method”, Metal Progress Data Sheet (1964), 99-102.

[124] Evis Z., Doremus R.H., “Effect of YF_3 on hot-pressed hydroxyapatite and monoclinic zirconia composites”, Materials Chemistry and Physics 105 (2007), 76-79.

[125] Thomas M.B., Doremus R.H., Jarcho M., Salsbury R.L., “Dense hydroxylapatite: Fatigue and fracture strength after various treatments, from diametral tests”, Journal of Materials Science 15 (1980), 891-894.

[126] Kamst G.F, Vasseur J., Bonazzi C., Bimbenet J.J., “A new method for the measurement of the tensile strength of rice grains by using the diametral compression test”, Journal of Food Engineering 40 (1999), 227-232.

[127] Jang J., Kim S., “Factors affecting diametral tensile strength of microfilled dental composites”, Polymer Journal 28 (1996), 293-298.

[128] Landi E., Logroscino G., Proietti L., Tampieri A., Sandri M., Sprio S., “Biomimetic Mg-substituted hydroxyapatite: from synthesis to in vivo behaviour”, Journal of Materials Science: Materials in Medicine 19 (2008), 239-247.

[129] Zyman Z., Tkachenko M., Epple M., Polyakov M., Naboka M., “Magnesium-substituted hydroxyapatite ceramics”, Materialwissenschaft und Werkstofftechnik 37 (2006), 474-477.

[130] Slosarczyk A., Bialoskorski J., “Hardness and fracture toughness of dense calcium-phosphate-based materials”, Journal of Materials Science: Materials in Medicine 9 (1998), 103-108.

[131] Slosarczyk A., Paluszkiewicz C., Gawlicki M., Paszkiewicz Z., “The FTIR spectroscopy and QXRD studies of calcium phosphate based materials produced from the powder precursors with different Ca/P ratios”, Ceramics International 23 (1997), 297-304.

[132] Torrent-Burgues J., Rodriguez-Clemente R., “Hydroxyapatite precipitation in a semibatch process”, Crystal Research and Technology 36 (2001), 1075-1082.

[133] Oliveira Ugarte J.F., Sena L.A., Castro Perez C.A., Aguiar P.F., Rossi A.M., Soares G.A., “Influence of processing parameters on structural characteristics of porous calcium phosphate samples: A study using an experimenta design method”, Materials Research 8 (2005), 71-76.

[134] Okazaki M., “Crystallographic behaviour of fluoridated hydroxyapatite containing Mg^{2+} and CO_3^{2-} ions”, Biomaterials 12 (1991), 831-835.

[135] Reid J.W., Fargo K., Hendry J.A., Sayer M., “The influence of trace magnesium content on the phase composition of silicon-stabilized calcium phosphate powders”, Materials Letters 61 (2007), 3851-3854.

[136] Iijima M., Moradian-Oldak J., “Control of apatite crystal growth in a fluoride containing amelogenin-rich matrix”, Biomaterials 26 (2005), 1595-1603.

[137] Rameshbabu N., Sampath Kumar T.S., Prasad Rao K., “Synthesis of nanocrystalline fluorinated hydroxyapatite by microwave processing and its in vitro dissolution study”, Bulletin of Materials Science 29 (2006), 611-615.

[138] Yang X., Wang Z., “Synthesis of biphasic ceramics of hydroxyapatite and β - tricalcium phosphate with controlled phase content and porosity”, Journal of Materials Chemistry 8 (1998), 2233-2237.

[139] Jarcho M., Bolen C.H., Thomas M.B., Bobick J., Kay J.F., Doremus R.H., “Hydroxylapatite synthesis and characterization in dense polycrystalline form”, Journal of Materials Science 11 (1976), 2027-2035.

[140] Rodriguez-Lorenzo L.M., Hart J.N., Gross K.A., “Structural and chemical analysis of well-crystallized hydroxyfluorapatites”, The Journal of Physical Chemistry B 107 (2003), 8316-8320.

[141] Qu H., Vasiliev A.L., Aindow M., Wei M., “Incorporation of fluorine ions into hydroxyapatite by a pH cycling method”, Journal of Materials Science: Materials in Medicine 16 (2005), 447-453.

[142] Okazaki M., Miake Y., Tohda H., Yanagisava T., Matsumoto T., Takahashi J., “Functionally graded fluoridated apatites, Biomaterials 20 (1999), 1421-1426.

[143] Okazaki M., Tohda H., Yanagisava T., Taira M., Takahashi J., “Heterogeneous fluoridated apatites synthesized with a three-step fluoride supply system”, Biomaterials 19 (1998), 919-923.

[144] Chen Y., Miao X., “Effect of fluorine addition on the corrosion resistance of hydroxyapatite ceramics”, Ceramics International 30 (2004), 1961-1965.

[145] Okazaki M., “Magnesium-containing fluoridated apatites”, Journal of Fluorine Chemistry 41 (1988), 45-52.

[146] Evis Z., Ozturk F., “Investigation of tensile strength of hydroxyapatite with various porosities by diametral strength test”, Materials Science and Technology 24 (2008), 274-278.

[147] Chau K.T., Wei X.X., “A new analytic solution for the diametral point load strength on finite solid circular cylinders”, International Journal of Solids and Structures 38 (2001), 1459-1481.

[148] Komlev V.S., Barinov S.M., Rustichelli F., “Strength enhancement of porous hydroxyapatite ceramics by polymer impregnation”, Journal of Materials Science Letters 22 (2003), 1215-1217.

[149] Pattanayak D.K., Divya P., Upadhyay S., Prasad R.C., Rao B.T., Rama Mohan T.R., “Synthesis and evaluation of hydroxyapatite ceramics”, Trends in Biomaterials and Artificial Organs 18 (2005), 87-92.

[150] Best S., Bonfield W., Doyle C., “In Proceedings of the Second International Symposium on Ceramics in Medicine”, edited by Heimke G., Heidelberg, Germany (1989), 57-64.

[151] Rousseau S., Buehler M., Jordi L., Lemaitre J., “Influence of magnesium on the working characteristics of brushite ceramics”, European Cells and Materials 5 (2003), 26-29.